

# Spatial and temporal variability of low-level convergence zones triggering deep moist convection in south-western Germany

Master's thesis in Meteorology  
by

**Fabian Siegmann**

February 2022



INSTITUTE OF METEOROLOGY AND CLIMATE RESEARCH  
KARLSRUHE INSTITUTE OF TECHNOLOGY (KIT)

Reviewer:

Prof. Dr. Michael Kunz

Second Reviewer:

Prof. Dr. Peter Knippertz



*This document is licenced under the Creative Commons Attribution-ShareAlike 4.0 International Licence.*

---

## Abstract

Extreme meteorological events in the form of severe thunderstorms pose a major threat to buildings, agriculture and human beings. In addition to damage caused by storms and flooding, hail events are a major source of financial loss. A clustering of hail events downstream of Central European low mountain ranges has already been observed in previous works. In this elaboration, cell tracks from TRACE3D and KONRAD cell detection and tracking algorithm as well as COSMO-DE model analysis data are used to investigate environmental conditions prevailing during the formation phase of hailstorms east of the Black Forest and over the Swabian Jura in south-western Germany. From the cell tracking data, the Swabian Jura can be confirmed as a thunderstorm and hail hotspot. Averaged over multiple time steps a pre-convective, dominant flow regime around the Black Forest is found in the ground level wind-field during situations with southwesterly mean flow. Downstream of the Black Forest, a spatially extended area of low-level horizontal moisture flux convergence can be detected in the model data. A relationship between the flow regime with respect to the Froude number and the location of the occurrence of these convergence regions is established, as well as an influence of the height of the planetary boundary layer on the low-level flow regime around the Black Forest. Furthermore, an event set is created including days with thermodynamic conditions suitable for the formation of deep moist convection, but without the actual appearance of the latter. This data set is compared with respect to flow dynamics with the situation on days with thunderstorms and hailstorms.



---

## Zusammenfassung

Extremwetterereignisse in Form von schweren Gewittern stellen eine große Gefahr für Gebäude, Landwirtschaft und Menschen dar. Neben Schäden durch Sturm und Überschwemmung haben Hagelereignisse einen bedeutenden Anteil an finanziellen Verlusten im Zusammenhang mit Gewittern. Bereits in früheren Arbeiten konnte eine Häufung von Hagelereignissen stromab der mitteleuropäischen Mittelgebirge beobachtet werden. In dieser Ausarbeitung werden Ergebnisse der Zelldetektions- und -verfolgungsalgorithmen TRACE3D und KONRAD, sowie Analysedaten des Wettervorhersagemodells COSMO-DE verwendet, um die Umgebungsbedingungen in der Entstehungsphase von Hagelgewittern im Bereich des Neckartals und der schwäbischen Alb zu untersuchen. Anhand der Zellverfolgungsdaten kann die Region stromab (östlich) des Schwarzwalds als Gewitter- und Hagelhotspot identifiziert werden. In zeitlichen Mittelwerten über mehrere Zeitpunkte während der Entstehungsphase von Schwergewittern im Untersuchungsgebiet können im bodennahen Windfeld Umströmungseffekte des Schwarzwaldes nachgewiesen werden. Im Lee des Schwarzwalds zeigt sich dabei in den Modelldaten ein ausgedehntes Gebiet von bodennaher horizontaler Strömungs- und Feuchteflusskonvergenz. Es kann ein Zusammenhang zwischen dem Strömungsregime hinsichtlich der Froude Zahl und dem räumlichen Auftreten dieses Konvergenzbereiches hergestellt werden, ebenso wie ein Einfluss der Höhe der planetaren Grenzschicht auf die Umströmungseffekte des Schwarzwalds. Im Rahmen der Arbeit wird ein Datensatz herausgearbeitet, der Events enthält, an denen die thermodynamischen Bedingungen für die Ausbildung von hochreichender Konvektion im Untersuchungsgebiet geeignet waren, diese aber nicht ausgelöst wurde. Dieser Datensatz wird hinsichtlich der Strömungsdynamik mit der Situation an Tagen verglichen, an denen es unter ähnlichen thermodynamischen Verhältnissen zur Auslöse von hochreichender Konvektion kam.



# Contents

<b>1</b>	<b>Introduction and Motivation</b>	<b>1</b>
<b>2</b>	<b>Theoretical Background</b>	<b>5</b>
2.1	Static stability . . . . .	5
2.2	Deep moist convection . . . . .	9
2.3	Thunderstorm types . . . . .	13
2.4	Rain and hail formation . . . . .	17
2.5	Basics of Radar Meteorology . . . . .	23
2.6	Convection above complex terrain . . . . .	28
2.7	COSMO-DE Model . . . . .	31
<b>3</b>	<b>Data and Methods</b>	<b>37</b>
3.1	Cell detecting and tracking . . . . .	37
3.2	Analysis and processing of cell tracking data . . . . .	42
3.3	Selection procedure for non-event days . . . . .	47
3.4	Threshold filtering of thunderstorm effects . . . . .	49
3.5	Spatial smoothing of horizontal moisture flux convergence fields . . . . .	52
3.6	Determination of flow regimes . . . . .	52
<b>4</b>	<b>Results</b>	<b>55</b>
4.1	Properties of cell tracks within the study area . . . . .	55
4.2	Limitations of initial potential hailstorm detections . . . . .	59
4.3	Relevance of dynamic conditions on potential hail storm occurrences in convection-favouring thermodynamical conditions . . . . .	61
4.4	Flow characteristics in different flow regimes and effects on potential hail- storm locality . . . . .	66
<b>5</b>	<b>Final remarks and discussion</b>	<b>71</b>
	<b>Bibliography</b>	<b>81</b>
	<b>List of figures</b>	<b>84</b>



# 1 Introduction and Motivation

Meteorological extreme events cause considerable economical losses year by year. During the winter period in Central Europe, the main losses are caused by winter storms. During summer, the losses are mainly related to thunderstorms producing lightning strikes, gale force gusts, heavy precipitation and related flash floods, hail or in rare cases even tornadoes. According to data from sigma-explorer thunderstorms are responsible for a total of 13 billion euros of economical damage from 1990-2020 (SwissRe-Institute, 2021) in Germany. With 2.3 billion, about 20% of this figure are produced by strong wind gusts in the context of thunderstorms. The other 80% of this amount (more than 10 billion euros) are related to hail events, whereas almost 7 billion euros originate from hail events in Baden-Württemberg. Accordingly the annual economic loss by hail is 340 million for Germany and 225 million euros for Baden-Württemberg. Kunz and Puskeiler (2010) estimated that about 40% of all insured damage in Baden-Württemberg are related to hail.

Convective storms basically can occur everywhere across Germany. Their frequency, however, show some distinct clear patterns that are governed by the climatology on the large-scale, but also by orographic flow modifications on the regional-scale. Damian (2011) found positive anomalies in lightning data over Germany's low mountain range such as the northern Black Forest and the northern crest of the Swabian Jura. By analysing radar data and cell tracks, Puskeiler (2009) estimated the spatial distribution of the expected annual extreme values of radar reflectivity over Baden-Württemberg and found the highest values between Stuttgart and Reutlingen. The reason for the increased hail probability in the vicinity of mountains is explained by the interaction between orography and flow conditions on different temporal and spatial scales. Necessary, but not sufficient conditions for the development of deep moist convection and thunderstorms are sufficient humidity above all in the lowest layers and an unstable atmosphere. The initiation of convection can be triggered by synoptic-scale lifting, e.g. by fronts, or by reaching a trigger surface temperature as a result of thermal heating by insolation. Orographic structures also play a central role in the development of convection because of direct thermal circulation or by flow deviation at the obstacles leading to convergence zones preferably over or downstream the crests. Brombach (2012), Koebele (2014) and Mahlke (2017) found an influence of near-surface flow convergence preferably downstream of the low-mountain ranges. These convergence areas, which develop as a result of a dominating flow around regime, can have both convection-inhibiting and convection-favoring effects from a local perspective.

In 2013, two severe hailstorms with record-breaking damage occurred within a short period of time in south-western Germany. One of them, the so-called "Reutlinger Hagelunwetter" of 28 July 2013 made history as the most expensive single event for the insurance industry to date (Kunz et al., 2018). According to data from sigma-explorer, the total thunderstorm event caused an insured loss of 3.5 billion euros and a total loss of 4.8 billion euros (SwissRe-Institute, 2021). Only nine days later, a supercell developed over the central Black Forest and moved across the Swabian Jura. At least one hailstone with a diameter of 14.1 cm was documented in Undingen. According to the European Severe Weather Database (ESWD, Dotzek et al., 2009), this was the largest hailstone ever documented in Germany.

According to Dotzek (2001) and Hagen et al. (2011), the regional distribution of thunderstorm and hail probability around mountain ranges is mainly determined by the flow dynamics in pre-convective conditions. Analyses of atmospheric soundings at 12 UTC from Stuttgart-Schnarrenberg demonstrated that prior to damage related hail days in Baden-Württemberg (1997-2007), relatively low mean wind speeds prevail together with a slightly stable stratified atmosphere (Kunz, 2007). The analysis of hailstorm track data with regard to the Froude number as the ratio of wind speed to stability and characteristic obstacle height provided evidence that suggest the flow around or over obstacles to be decisive for the initiation of convection. Previous investigations based on semi-idealized model simulations already found convergence areas in the lee of obstacles during low Froude numbers (Brombach, 2012; Koebele, 2014). In both cases, the model was driven with a mean vertical profile of damage-relevant hail days, which was held constant at the boundaries of the investigation area. However, a detailed consideration of atmospheric environmental conditions such as the Brunt Vaisala frequency and the Froude number was not performed.

The objective of the prevailing master's thesis is to analyse horizontal low-level moisture flux convergences and divergences prior and during the formation of (severe) thunderstorms in the area of the Neckar Valley and the Swabian Jura with regard to their location and intensity. Input data are COSMO-DE model analyses and radar-based tracks of severe convective storms, whereby the sample of individual events or days was separated with regard to the prevailing large-scale conditions (wind direction, Froude number). Thereby, differences in the orography related influence on the surface-near wind field between different flow regimes are to be elaborated. Furthermore, the flow dynamic situation will be compared between event days (days with thunderstorm initiation within the investigation area) and non-event days (days with suitable thermodynamic conditions but no appearance of thunderstorms within the investigation area). Available for the investigations were hourly COSMO-DE assimilation analyses with 2.8 km resolution for the period 2011-2017 as well as thunderstorm tracks obtained from radar data. There are two data sets for cell tracks: For single cells based on tracking with KONRAD (**KON**vektive Entwicklung in

---

**RAD**arprodukten) a data set from Wilhelm (2021) is used. For potentially hail producing thunderstorms based on tracking with TRACE3D a data set from Schmidberger (2018) is used, where the tracking was performed with a reflectivity threshold of 52 dBZ to identify potential hailstorms.



# 2 Theoretical Background

## 2.1 Static stability

The vertical stratification of the atmosphere is an important characteristic in meteorology, especially for vertical fluxes or vertical movements. A basic distinction is made between stable, neutral and unstable stratification. While stable stratification counteracts vertical upward motions in the atmosphere, unstable stratification can favour and amplify vertical lifting. However, there are also other cases such as conditional, latent or potential instability. Conditional instability occurs when the stratification is dry-stable but becomes moist-unstable when condensation begins, i.e. when the atmospheric temperature gradient is between the dry- and the moist-adiabatic gradient. Latent instability occurs when, in a conditionally unstable stratified atmosphere, moist air parcels rise by forced lifting and experience free buoyancy in the process (Normand, 1938). Potential instability is present when moist air is stored below dry air. If such a column of air experience large scale lifting, the lower air parcels reach saturation earlier than the upper air parcels. As the upper air parcel continues to cool down in a dry-adiabatic manner, the air column becomes more unstable. Static stability can either be determined by comparing the prevailing atmospheric vertical temperature gradient with the dry or moist adiabatic temperature gradient or using a derived quantity such as the Brunt-Vaisala Frequency.

### 2.1.1 Potential Temperature

The dry-adiabatic temperature gradient describes the temperature change that an air parcel experiences through vertical displacement under isentropic conditions. If an air parcel, treated as a mechanically-closed, adiabatic thermodynamic system, is moved upwards in the atmosphere, the ambient pressure decreases and the air parcel experiences an expansion, i.e. increases its volume. According to the first thermodynamic equation

$$dU = \delta Q + \delta W = \delta Q - pd\alpha, \quad (2.1)$$

the change in volume leads to a change in the inertial energy and, thus, in the temperature assuming dry-adiabatic lifting ( $\delta Q = 0$ ). Here  $U$  corresponds to the internal energy,  $Q$  to the internal heat and  $W$  to the work that is done,  $\alpha$  represents the specific volume and  $p$  the pressure,  $d$  denotes a total differential and  $\delta$  an inexact differential. Combining the first thermodynamic equation with the hydrostatic approximation

$$\frac{dp}{dz} = -\rho g \quad (2.2)$$

leads to the vertical temperature gradient

$$\frac{\partial T}{\partial z} = -\frac{g}{c_p}. \quad (2.3)$$

$z$  describes the altitude,  $\rho = \alpha^{-1}$  the density and  $g$  the standard acceleration due to gravity.  $T$  describes the temperature of the air parcel and  $c_p$  the specific heat capacity at constant pressure. Inserting  $g = 9.81 \text{ ms}^{-2}$  and  $c_p = 1.005 \text{ Jg}^{-1}\text{K}^{-1}$  yields the dry-adiabatic temperature gradient

$$\Gamma_{\text{dry}} = -\frac{\partial T}{\partial z} = 0.976 \frac{\text{K}}{100\text{m}}. \quad (2.4)$$

In the atmosphere the dry-adiabatic temperature gradient is applicable for vertical motions where no diabatic processes, especially phase transitions, take place. This is generally the case for air parcels whose relative humidity is below 100 %.

The potential temperature describes the temperature of an air parcel that is lifted or descended dry-adiabatically from a certain pressure  $p$  to a reference pressure  $p_0$ . Typically  $p_0$  is set to 1000 hPa. With the gas constant for dry air  $R_d$

$$R_d = \frac{R}{M} = \frac{N_A}{k_B}, \quad (2.5)$$

where  $R$  is the universal gas constant,  $M$  the molar mass,  $N_A$  the Avogadro constant and  $k_B$  the Boltzmann constant, one can formulate the equation of state for an ideal gas (in this case: dry air)

$$p\alpha = R_d T \quad (2.6)$$

With

$$c_p dT = \alpha dp \quad (2.7)$$

a dry-adiabatic process can be described by

$$d\ln(T) = \frac{R_d}{c_p} d\ln(p). \quad (2.8)$$

With  $\gamma = c_p c_V^{-1}$ , where  $c_V$  is the specific heat capacity at constant volume, indefinite integration of this equation leads to

$$T^\gamma p^{1-\gamma} = \text{const.} \quad (2.9)$$

A solution of this Poisson equation, by integration from the reference level  $p_0$  to an any pressure level  $p$ , yields the potential temperature

$$\theta = T \left( \frac{p_0}{p} \right)^{\frac{R_d}{c_p}} \quad (2.10)$$

as a suitable measure for comparing the temperature of air parcels from different pressure levels and a measure of the entropy content of an air parcel.

### 2.1.2 Equivalent potential Temperature

The concept of dry-adiabatic ascent usually cannot be considered as a realistic concept in the atmosphere. The cooling associated with ascent increases the relative humidity and finally brings the air parcel to saturation. The height at which an air parcel reaches saturation is called the condensation level. If it continues to rise above this level, condensation occurs, releasing latent heat of condensation as a result of phase transition. This heat is added to the air parcel and counteracts the adiabatic cooling. For water, the specific enthalpy of evaporation at standard conditions (1013.25 hPa and 25 °C) is about

$$l_v = 2.44 \text{ kJ g}^{-1}. \quad (2.11)$$

The equivalent potential temperature describes the temperature that would be expected of an air parcel that is lifted dry-adiabatically below the condensation level and moist-adiabatically above the condensation level and is afterwards brought to a reference pressure of 1000 hPa again in a dry-adiabatically manner. In this case, one assumes the process to be reversible which means that the condensate remains in the air parcel. The equivalent potential temperature is then calculated by

$$\theta_e = \theta \exp\left(\frac{l_v r_s}{c_p T}\right), \quad (2.12)$$

where  $r_s$  describes the saturation mixing ratio. For the pseudo-potential temperature any liquid water that condensates is assumed to be removed as soon as it is formed, by idealized instantaneous precipitation. By removing the condensed water, the assumption of adiabasia ( $\delta Q = 0$ ) is no longer sustainable and the process has to be considered as not reversible. An approximation for the pseudo-adiabatic temperature was done by Bolton (1980).

Since in the case of moist-adiabatic rise the latent heat released by condensation counteracts the adiabatic cooling, the moist adiabatic temperature gradient is smaller than the dry-adiabatic gradient. Typically, it ranges from

$$0.5 \frac{\text{K}}{100\text{m}} < \Gamma_{\text{moist}} < 0.7 \frac{\text{K}}{100\text{m}}. \quad (2.13)$$

However, for extremely cold environmental conditions in the upper troposphere  $\Gamma_{\text{moist}}$  and  $\Gamma_{\text{dry}}$  are almost identical as the heating effect of condensation processes is only small due to the small amounts of moisture.

### 2.1.3 Buoyancy in the atmosphere

The buoyancy of an air parcel is caused by the difference between its own density and the density of the surrounding air. Writing the equation of state for an ideal gas (here: dry air)

$$p = \rho R_d T, \quad (2.14)$$

it can be seen, that the difference in density  $\rho$  can also be expressed as a difference in pressure and temperature (Houze, 1994).

From the momentum equation consisting of pressure gradient force, effective gravitational force, Coriolis force and friction force

$$\frac{d\vec{v}}{dt} = -\frac{\nabla p}{\rho} + \Phi - 2\vec{\Omega} \times \vec{v} - \nabla \cdot \vec{f} \quad (2.15)$$

the third component is used to derive the buoyancy. In Equation 2.15,  $\vec{v}$  describes the three-dimensional motion of the fluid,  $\Phi$  the effective gravitational force consisting of gravitation and centrifugal force,  $\vec{\Omega}$  the constant vector of the angular velocity of the earth rotation and  $\vec{f}$  the viscous stress tensor. Neglecting the effects of the Coriolis force and friction forces, and using the approximation  $\Phi \approx g = 9.81 \text{ ms}^{-2}$ , one finds for the vertical component of the momentum equation

$$\frac{dw}{dt} = -\frac{1}{\rho} \frac{\partial p}{\partial z} - g, \quad (2.16)$$

where  $w$  describes the vertical velocity. Decomposition of the contributions of the state variables  $p$ ,  $\rho$  and  $T$  into a horizontally homogeneous mean state and small disturbances according to the scheme

$$\xi(z) = \bar{\xi}(z) + \xi'(z), \quad (2.17)$$

under the assumption of hydrostasy for the mean state

$$\frac{\partial \bar{p}}{\partial z} = -\bar{\rho} g \quad (2.18)$$

leads to

$$\frac{dw}{dt} \approx -\frac{1}{\rho} \frac{\partial p'}{\partial z} - \frac{\rho'}{\rho} \quad (2.19)$$

for the vertical velocity. Here

$$B = -\frac{\rho'}{\rho}. \quad (2.20)$$

is the thermal buyoancy.

### 2.1.4 Parcel theory

In meteorology, cumulus convection in the atmosphere is commonly described using the parcel method. Equation 2.19 and 2.20 lead to the vertical velocity

$$\frac{dw}{dt} \approx -\frac{1}{\rho} \frac{\partial p'}{\partial z} + B \quad (2.21)$$

to be only dependent on the vertical change of the pressure perturbation  $\delta p$  and the buoyancy force  $B$  under the given assumptions (decomposition of state variables in mean and perturbation, as well as neglect of Coriolis and friction forces, Houze, 1994).

The parcel method is useful because it provides an illustrative bridge between stability measures in the atmosphere and the development convection. However, Equation 2.21 often provides an overestimation of the actual vertical acceleration, as effects such as entrainment and the density change of the air parcel due to condensation are neglected.

### 2.1.5 Brunt Vaisala Frequency

Static stability can also be expressed by the Brunt Vaisala frequency. Considering Equation 2.21 for the vertical acceleration of an air parcel and neglecting the pressure perturbation term

$$\frac{\partial^2 z}{\partial t^2} + N^2 z = B + N^2 z = 0 \quad (2.22)$$

one finds the differential equation of a frictionless harmonic oscillation with  $N$  as the

$$N = \sqrt{\frac{g}{\theta} \frac{\partial \theta}{\partial z}} \quad (2.23)$$

the Brunt Vaisala frequency (Etling, 1996).

## 2.2 Deep moist convection

### 2.2.1 Development and initiation of deep moist convection

In meteorology, convection refers to the vertical transport of an air parcel. Convection is visually detectable in the atmosphere as soon as the condensation level is exceeded and cloud droplets form. If this is not (yet) the case, the term blue thermal (originating from aviation and gliding) is used. The spectrum of convective systems ranges from cumulus clouds to supercells to multicells to mesoscale convective systems (MCS). Deep moist convection is described as when the vertical extent of the convective cell is approximately equal to or greater than the horizontal extent of a convective system.

The following conditions are necessary for the formation and triggering of deep moist convection (Doswell, 1987):

- Sufficient static instability (conditional, potential, latent)

- Sufficient amount of moisture especially in lower troposphere
- Vertical lifting to trigger convection

The convection initiation can occur in different ways. Generally, a distinction is made between free lifting, e.g. by reaching the trigger temperature at the surface, and forced lifting, e.g. initial uplift at obstacles like mountains. The following lifting mechanisms can be involved in the triggering of convection (North Carolina Climate Office, 2021):

- Thermal lifting by reaching the trigger temperature at the surface
- Thermal lifting by land-sea-circulation or mountain-valley-circulation
- Forced lifting by orography
- Forced lifting by convergence
- Synoptic-scale lifting by differential temperature advection and vorticity advection
- Frontal lifting

Commonly, several factors are involved in the formation of deep moist convection simultaneously. In Central Europe, suitable conditions are often found at the front of a trough, where the advection of warm and humid air provides destabilisation through synoptic-scale lifting processes (Jukes and Smith, 2000). Corresponding surface lows can additionally provide convergence areas and frontal uplift processes (Wissmeier and Goler, 2009). The influence of the jet stream in such cases often provides sufficient vertical wind shear to allow the formation of organised convection (Graf et al., 2011).

### 2.2.2 CAPE

The **C**onvective **A**vailable **P**otential **E**nergy (CAPE) is a measure of the energy that is based on the temperature difference between an idealised rising air parcel  $T_{vp}$  and its environment  $T_{ve}$  within two specific height levels (Scorer, 1995). To explain the meaning of CAPE it is helpful to understand the lifting condensation level (LCL), the level of free convection (LFC) and the level of neutral buoyancy (LNB). Considering an air parcel that is lifted starting from a initial level, the ascent is dry-adiabatic, which means that the potential temperature and the saturation mixing ratio are conserved. The LCL is the altitude at which the air parcel reaches saturation. Above this level, further ascent is moist-adiabatic. The LFC is at the altitude above which the air parcel is warmer than the ambient air and thus experiences a buoyancy force. A LFC may not always be present. If there is a LFC, there is also a LNB, above which the temperature of the air parcel is lower than that of the ambient air. It is usually located at the upper edge of the troposphere (Markowski and Richardson, 2010). For the calculation of CAPE, the virtual temperature

$$T_v = T \cdot \frac{1 + \frac{r_v}{\epsilon}}{1 + r_v + r_l} \quad (2.24)$$

is used, i.e. the temperature that dry air would need in order to have the same density as humid air at a lower real temperature and the same pressure. In Equation 2.24,  $T$  is the temperature,  $r_v$  is the water vapour mixing ratio ( $m_{\text{vapor}} m_{\text{dry-air}}^{-1}$ ),  $r_l$  is the liquid water mixing ratio ( $m_{\text{liquid}} m_{\text{dry-air}}^{-1}$ ) and  $\epsilon \approx 0.622$  is the ratio of the molar masses of water vapour and dry air. If not only liquid water is present but also frozen water, then the term  $r_l$  can be replaced by  $r_{\text{cond}} = r_l + r_{\text{ice}}$ , where  $r_{\text{ice}}$  is the frozen water mixing ratio. The calculation of CAPE is commonly done by

$$\text{CAPE} = \int_{\text{LFC}}^{\text{LNB}} R_d (T_{\text{vp}} - T_{\text{ve}}) d\ln(p). \quad (2.25)$$

In this form, CAPE represents the maximum amount of energy that an air parcel can extract from the potential energy during an ascent, whereas the ascent is dry adiabatic from the initial starting position of the parcel  $z_{\text{start}}$  (in this case the LFC) to the LCL and pseudo-adiabatic from the LCL to the LNB (cf. also Figure 2.1). At the LNB, the air parcel no longer experiences buoyancy, and above the LNB it even experiences downward acceleration. The LNB is inevitable because at the upper boundary of the troposphere, in the tropopause, the atmospheric vertical temperature gradient weakens and even changes its sign. The tropopause thus acts as an inverse barrier between the troposphere and the stratosphere. It is also possible to calculate the CAPE from the LCL to the LNB. CAPE is directly related to the vertical speed of an air parcel during the ascent. As a rough rule of thumb, the maximum possible thermodynamic vertical velocity of an air parcel can be estimated with

$$w = \sqrt{2 \cdot \text{CAPE}}. \quad (2.26)$$

However, since inhibiting effects such as the increase in density of the air parcel due to condensate, pressure perturbation and entrainment are neglected here, this approximation is usually an overestimation (Lamb and Verlinde, 2011).

There are different types of CAPE depending on the starting point of the air parcel. The **Most Unstable CAPE** is the maximum CAPE that one can find by starting the air parcel in the specific height in the lowest 300 hPa of the atmosphere, where the value of CAPE becomes maximum.

The **Mixed Layer CAPE** represents the available potential energy of an air parcel with the mean characteristics of a low level layer (usually the lowest 100 hPa) when lifted to the LNB.

One speaks of the **Surface Based CAPE** when the ascent of the considered air parcel starts at the earth surface.

CAPE is a commonly used indicator to forecast deep moist convection and its strength. It is worth noting, that high CAPE values - and therefore high amounts of available energy - is not sufficient for the formation of thunderstorms as there is also a trigger process needed, which allows the available energy to be released (cf. Section 2.2.1).

In Central Europe, typical CAPE values for thunderstorms range from 800 to 2800 Jkg<sup>-1</sup>

(Westermayer et al., 2017). Kunz (2007) has found for south-western Germany that CAPE values above  $1500 \text{ Jkg}^{-1}$  often occur in association with hail events.

### 2.2.3 CIN

In most cases, a certain amount of energy must be overcome for an air parcel starting at a certain level  $z_0$  to reach the LFC. This convection-suppressing energy barrier is called **C**onvective **I**Nhibition (CIN). As with CAPE, the calculation is done using the temperature difference between the air parcel and the ambient temperature with

$$\text{CIN} = - \int_{z_0}^{\text{LFC}} R_d (T_{\text{vp}} - T_{\text{ve}}) d \ln(p). \quad (2.27)$$

CIN often results from a temperature inversion in the upper region of the planetary boundary layer. The depletion of CIN can occur through large-scale or orographic lifting, but also through lifting effects in convergence areas or by reaching the trigger temperature at surface level or moisture pooling.

CAPE and CIN can be illustrated in vertical profiles of temperature and dewpoint. The determining parameter is the enclosed area between the vertical temperature profile and the pseudo-adiabatic ascent of an air parcel from its initial level. In a skewT-log p diagram, the enclosed area above the LFC represents CAPE, below the LFC it represents CIN (cf. Figure 2.1).

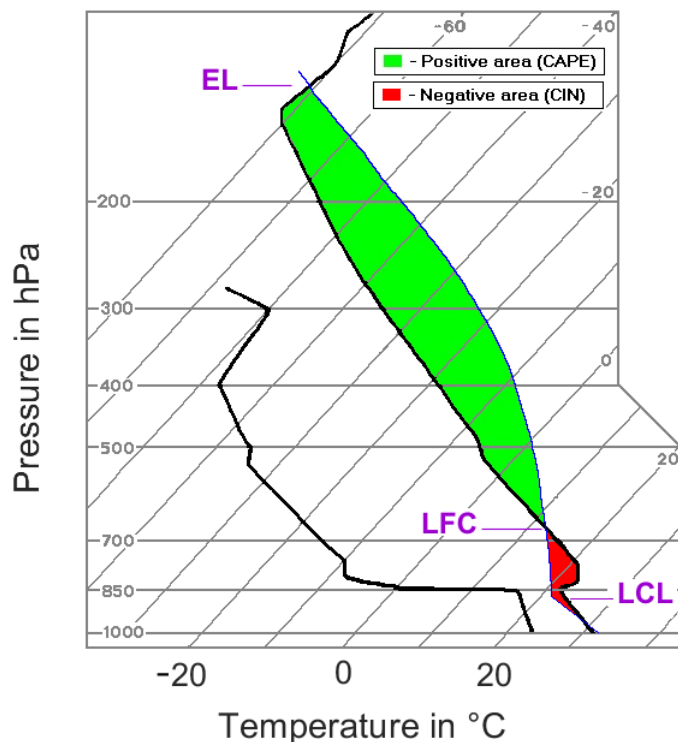


Figure 2.1: CAPE and CIN visualized in the skewT-log p diagram. The solid black lines indicate vertical profiles of temperature and dew point (dew point is always equal or smaller than the temperature and therefore is the line on the left). Green and red areas represent CAPE and CIN. LFC describes the level of free convection, LCL the lifted condensation level. The equilibrium level EL corresponds to the level of neutral buoyancy LNB (PennState Meteorology Department, 2021).

## 2.3 Thunderstorm types

Although any form of thunderstorm can have severe effects and may cause considerable damage, it is essential to distinguish between different types of convective systems. All convective cells differ in their forms, characteristics, and thus typically also in their spatial extent and lifetime. The high residence time and large vertical extension in so-called organised, multicellular convection provides suitable conditions for the formation of coarse hail by freezing processes. The following chapter also considers the **supercell**, a special case of the single cell, which can achieve enormous lifetimes due to spatial separation of upwind and downwind regions (so-called up- and downdrafts).

### 2.3.1 Single cell

The life cycle of a non-rotating single cell can be divided into three stages. The life cycle begins in the **cumulus stage** with an air parcel lifted to the LCL, where condensation sets in and cloud formation begins. When the parcel continues to rise, it cools down in a moist adiabatic process and thus typically experiences an increasing buoyancy force with altitude (cf. Section 2.2.2). Vertical velocity in single cell thunderstorm typically ranges from 5 to 20  $\text{ms}^{-1}$  (Adler and Fenn, 1979). Therefore, the cloud droplets grow

not only by condensation but also by collision coalescence. In the upper region of the cloud, more and more ice particles are being formed. Since the saturation with respect to the ice phase is significantly greater than the saturation with respect to the liquid water phase, ice particles can grow significantly faster than liquid water droplets. In the specific case of supersaturation with respect to the ice phase and subsaturation with respect to the liquid water phase, ice particles can grow at the expense of liquid water droplets (Wegener-Bergeron-Findeisen process, Wegener, 1911 and Bergeron, 1928). Therefore, ice particles can rapidly grow to a critical size at which the downward directed gravitational force can no longer be compensated by the upward directed buoyancy force. This is the stage where the cloud starts to precipitate.

A common definition for the beginning of the **mature stage** is the moment when precipitation reaches the surface for the first time. At the upper part of the cloud precipitation-forming processes and vertical lifting are still effective due to the low temperatures and create the typical anvil structure of the cloud below the tropopause through a divergent flow. In the lower area, the updrafts are already weakened by the neighbouring downdraft area, mixing in of dry environmental air and the formation of a divergent wind field at ground level, that creates the so-called gust front. Apart from strong wind speeds the gust front also acts as a boundary separating the cooled outflow of a thunderstorm cell from the environmental air. Its passage is therefore often characterized by an increase in wind speed, as well as temperature decrease and a related pressure increase. Depending on the relative position to the thunderstorm, not only the speed but also the wind direction may change.

In the **dissipation stage**, the updrafts weaken continuously as a result of the missing separation between up- and downdrafts due to low environmental vertical wind shear (characteristic deep layer shear from 0 to 6 km below  $10 \text{ ms}^{-1}$ , Markowski and Richardson, 2010). Without the supply of warm and humid air the updraft region can no longer be maintained and a single large-scale downdraft area establishes. The cloud then dissipates starting from the bottom, while remnants of the anvil often remain at the upper edge of the troposphere in the form of cirrus clouds.

Single cells are often coupled to the diurnal cycle of the temperature. Because upwind and downwind areas are not separated in space, the lifetime is usually less than 60 min.

### 2.3.2 Multicell

A multicellular thunderstorm cluster is composed of multiple up- and downdraft couplets from cells at different stages in their life cycle. In a vertically moderate sheared environment (characteristic deep layer shear between  $8$  and  $20 \text{ ms}^{-1}$ , Markowski and Richardson, 2010), updraft and downdraft regions are separated from each other with the downdraft located downstream of the updraft. When a cell reaches the maturity stage and forms a gust front, this structure provides surface-level flux convergence between gust front and

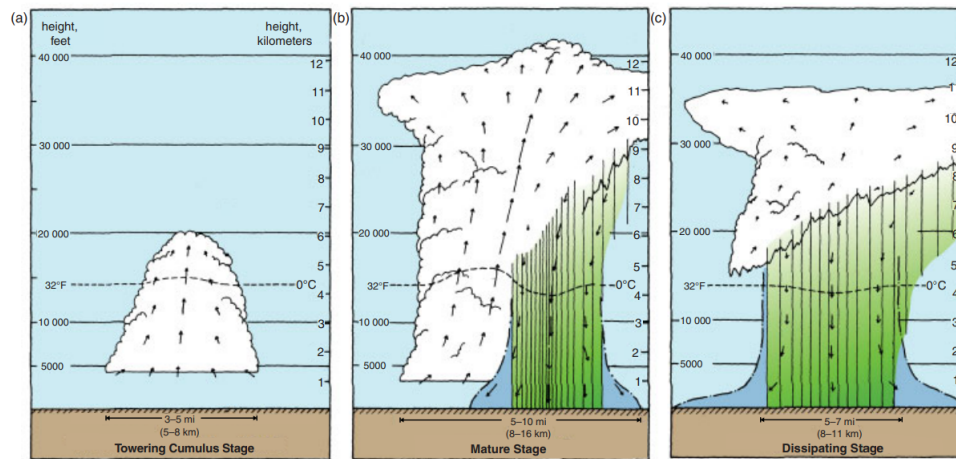


Figure 2.2: Illustration of the typical life cycle of a single cell thunderstorm (from left to right). Arrows indicate up- and downdrafts, green areas indicate precipitation, blue areas indicate rain-cooled air. Dashed line indicates the  $0^{\circ}\text{C}$  isotherm. Figure slightly adopted from Markowski and Richardson (2010). Primarily based on Byers and Braham (1948) and Doswell (1985).

low-level wind field downstream of the cell. Considering horizontal vorticity, negative vorticity from the gust front near the ground and positive vorticity from the westerly wind shear collide in this area (referred to Figure 2.3). Due to the repetitive formation of new updraft areas, multicells can reach lifetimes of several hours up to one day. The effective propagation vector of a multicell is composed of the propagation due to the mean flow and the apparent displacement due to the formation of new cells. The propagation speed and direction of multicells therefore may differ from the mean flow. According to Marwitz (1972), the angle between mean flow direction and displacement direction by new cell formation can reach  $50^{\circ}$  in individual cases.

### 2.3.3 Supercell

Supercells are a specific type of single cells that are characterised by an organised structure and are more intense and larger in scale. Characteristic for a supercell is a rotating updraft that covers at least one third of the vertical extent and has a lifetime of at least 30 min (Kessler, 1981). While velocity shear in the vertical wind profile is necessary for the formation of multicells, supercells preferentially form in environments with both velocity and directional shear. Structurally, a supercell is defined by the presence of a mesocyclone and a spatial separation of the up- and downdraft regions. The updraft region covers the whole troposphere and is inclined in the direction of the mid-tropospheric (500 hPa) wind vector. The updraft core is characterized by weak radar reflectivity (so-called bounded weak echo region) and updraft velocity can reach up to  $65\text{ ms}^{-1}$  (DiGangi et al., 2016). At middle and high altitudes of the system, moderate to strong storm-relative winds create a separation between the supercell updraft and the elevated hydrometeors. This allows the hydrometeors to fall to the ground outside of the updraft instead of through the updraft area. The downdraft regions are enhanced by the precipitation, especially in the proximity the forward-flank downdraft (FFD) and the rear-flank downdraft (RFD) that evolve at

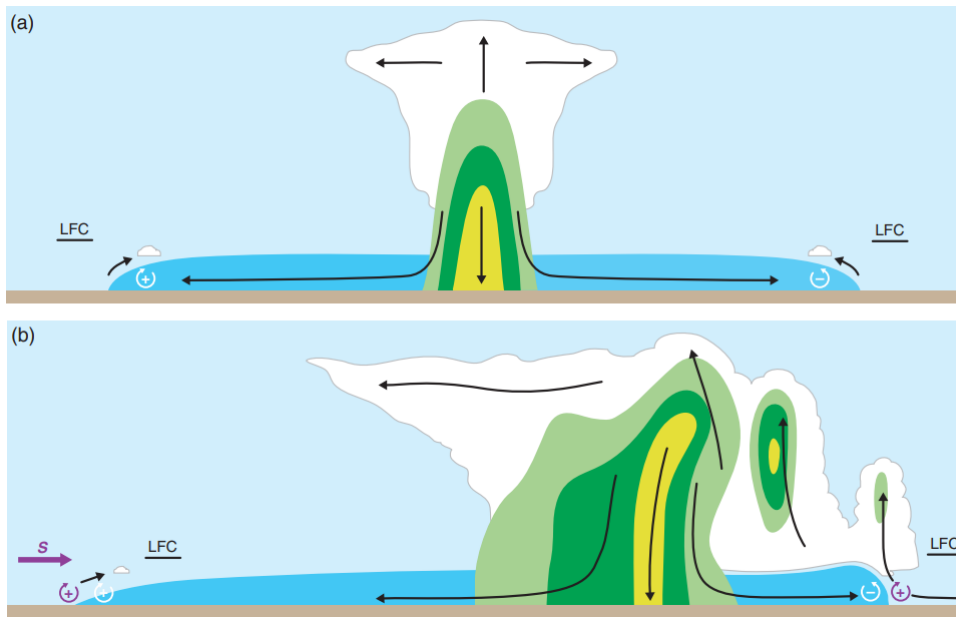


Figure 2.3: Comparison of gust front related lifting processes in a no-shear environment (upper part) and a moderate westerly shear environment (lower part). Clouds, rain and heavy rain / hail are represented by white, green and yellow shading. Cool outflow is shaded blue. Solid black arrows indicate storm-relative streamlines, horizontal vorticity is displayed by circular arrows (white for cold pool induced vorticity, dark purple for shear induced vorticity). Figure by Markowski and Richardson (2010).

the front and at the rear of the system. Those downdraft areas also benefit from the inflow of relatively cool ambient air at medium altitudes. Evaporation and sublimation provide further cooling and intensification of the downward movement. At ground level, well-defined interfaces can be identified between the cold outflowing air of these downdrafts and the ambient air (gust fronts, Trapp, 2013). Due to their long lifetime and strong updrafts, the largest hailstones develop in supercells (cf. also Section 2.4.3).

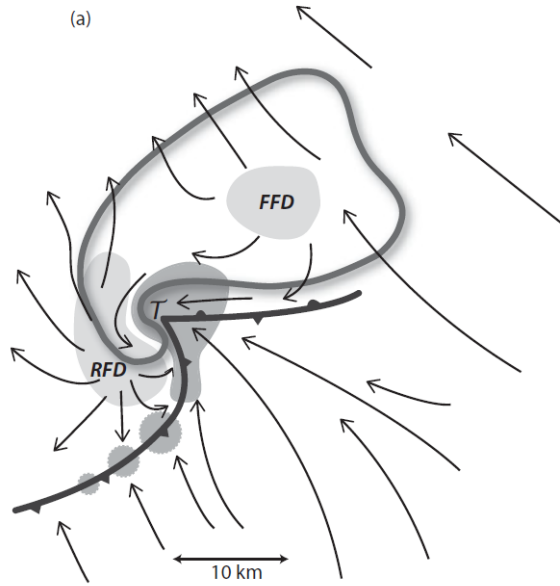


Figure 2.4: Plan-view schematic of a supercell thunderstorm at low levels. T indicates a mesocyclone, the grey contour marks the boundary of heavy precipitation, the dark grey areas represent updraft areas, the light grey areas represent downwind areas (FFD: Forward-Flank Downdraft; RFD: Rear-Flank Downdraft). The storm-relative low-level wind field is represented by arrows, its convergences by the dark grey front line. Figure from Trapp (2013) adopted by Lemon and Doswell (1979).

## 2.4 Rain and hail formation

### 2.4.1 Nucleation

During the formation of rain and hail, various microphysical processes take place subsequently. The initial cloud formation is described by the process of nucleation, i.e. the transition from gaseous water vapour to liquid water droplets or solid ice particles. Droplet and particle growth within a cloud can occur both by condensation and by collection. The processes involved will be described briefly in the following.

According to the classical nucleation theory, during a phase transition by nucleation, the new phase is initially formed by nuclei from the original, meta-stable phase. In case of homogeneous nucleation, the formation of these nuclei is counteracted by the work that must be applied to form the curved surface of a nucleus (e.g. a spherical droplet) of the new phase. For very small droplets or crystals, this surface work is greater than the energy gain from the transition to the new, meta-stable phase. This results in an energy barrier that has to be overcome. In the atmosphere, this energy barrier is reduced through the influence of cloud condensation nuclei (CCNs) or ice nucleating particles (INPs). Figure 2.5 shows the dependence of the volume and interface term on the nucleus size  $N$  and the resulting threshold value of the nucleus size  $N^*$ . The free energy of germ formation  $G$  is calculated from the sum of the two terms

$$\Delta G = -NkT\ln(S) + \sigma A, \quad (2.28)$$

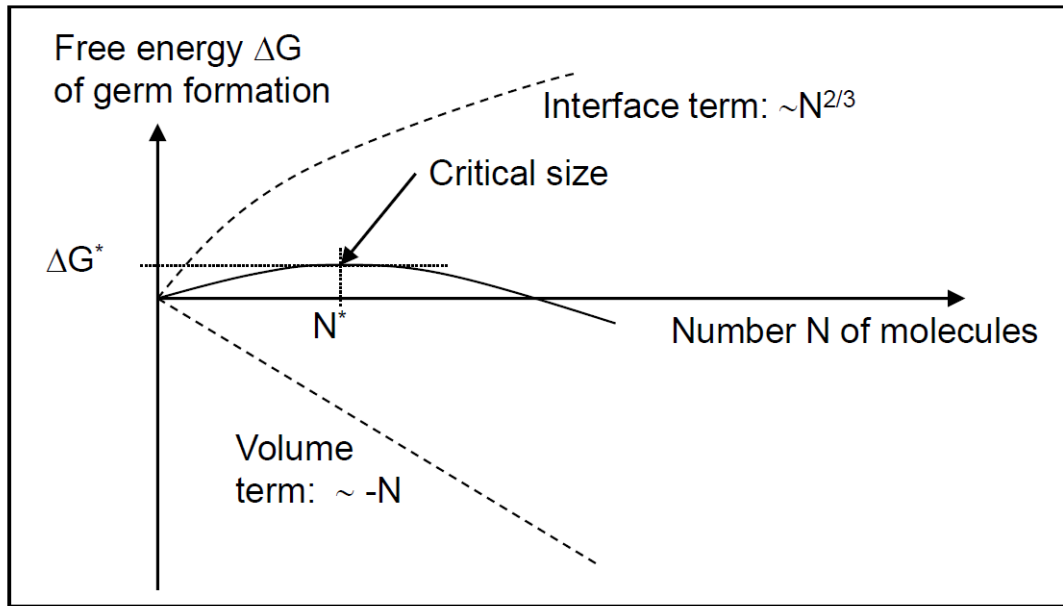


Figure 2.5: Classical nucleation theory (Köhler, 1921). Visualization of the critical embryo size  $N^*$  for cloud droplet formation by Möhler (2019). The interface term represents the work required to form a nucleus of the new phase. The volume term represents the energy difference between the two phases involved.

where  $N$  is the number of molecules changing their phase state,  $k$  the Boltzmann constant,  $S$  the saturation ratio,  $\sigma$  the surface or interface tension and  $A$  the germ surface area (Köhler, 1921).

The classical nucleation theory can be applied to the initial formation of liquid cloud droplets as well as to the formation of ice particles in an already existing liquid water cloud. For the further growth of a liquid water droplet (with an enclosed CCN), the curvature effect and the solution effect also play a role. The curvature effect causes the saturation vapor pressure to be higher over a curved surface than over a flat surface. The effect is strongest for very small droplets and weakens with increasing droplet radius. The solution effect has an opposite impact. A particle dissolved in the liquid (CCN) makes it difficult to leave the liquid composition, which is why the saturation vapor pressure is lower than it would be for a pure liquid.

## 2.4.2 Droplet and particle growth

Once a droplet is formed, further growth can take place via condensational growth or collectional growth. Condensational growth describes the process, where a given droplet or ice particle grows by diffusion from the vapor phase by increasing its size molecule by molecule. Water vapor condenses onto a surface, whenever the partial pressure of vapor  $e$  is greater than the equilibrium pressure  $e_{\text{eq}}$  of the surface. The radius growth rate by condensation can be described via

$$\left. \frac{dr_d}{dt} \right|_{\text{cond.}} = \frac{8}{\rho_l r_d} G s, \quad (2.29)$$

where  $r_d$  is the droplet radius,  $\rho_l$  is the density of water,  $G$  is the effective diffusivity and  $s = S - 1$  is the environmental supersaturation. The condensational radius growth rate

$$\left. \frac{dr_d}{dt} \right|_{\text{cond.}} \propto \frac{1}{r_d} \quad (2.30)$$

is then found to be antiproportional to the radius  $r_d$  itself (Lamb and Verlinde, 2011).

Collectional growth of hydrometeors is driven by collisions. These collisions may occur by chance, but primarily happen when hydrometeors of different sizes and therefore different vertical velocities are in proximity to each other.

A collision of two hydrometeors can have multiple outcomes:

- Rebound: no change in number concentration
- Shattering: increased number concentration
- Collection: reduced number concentration, mass growth for the larger hydrometeor

The droplet radius growth by collection is described via

$$\left. \frac{dr_d}{dt} \right|_{\text{coll.}} = \frac{v_d \bar{E}_c \text{LWC}}{4\rho_l} \quad (2.31)$$

and therefore is proportional to  $r_d$

$$\left. \frac{dr_d}{dt} \right|_{\text{coll.}} \propto r_d. \quad (2.32)$$

The collection efficiency  $E_c$  describes the probability of a collision event followed by coalescence. It has a maximum of about 65% at a radius ratio between small and large droplets of about 0.1. A smaller radius ratio provides fewer collision events (as a very small droplet swirls around the larger droplet), a larger ratio reduces the probability of coalescence. In Equation 2.31,  $\bar{E}_c$  describes the mean collection efficiency over different droplet radii.  $v_d$  describes the velocity of the larger droplet, LWC the liquid water content and  $\rho_l$  the density of liquid water.

Comparing Equation 2.30 and 2.32 indicates the condensational growth to be efficient for small droplets and to be less efficient for larger droplets (Lamb and Verlinde, 2011). Vice versa, the growth by collection is most efficient for larger drops.

The formation of ice particles in the atmosphere occurs either starting from the ice phase via deposition (Wegener-Bergeron-Findeisen process, cf. Section 2.3.1) or starting from liquid droplets using INPs. A distinction is made between immersion freezing, condensation freezing and contact freezing. Immersion freezing is induced by an INP immersed in supercooled water. Condensation freezing occurs when an aerosol particle acts as a CCN and immediately initiates freezing of the water condensate. Contact freezing occurs

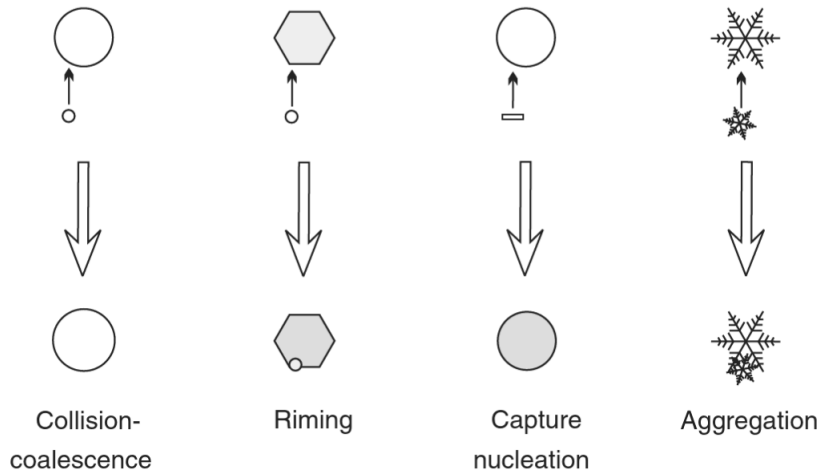


Figure 2.6: Droplet and particle growth processes involving collection (Lamb and Verlinde, 2011). Round and white symbols indicate droplets, hexagon-like shaded symbols indicate ice particles.

when supercooled liquid water droplets freeze instantaneously upon contact with an INP (Pruppacher and Klett, 1997).

Considering collection between liquid droplets as well as ice particles, one further distinguishes between different processes shown in Figure 2.6. Collision coalescence describes the collision of two (typically) differently sized liquid droplets that merge into one large droplet. When a (supercooled) droplet collides with an ice particle and freezes onto its surface instantaneously, one speaks of riming or accretion. Capture nucleation describes the collision of a (supercooled) droplet with a small ice crystal, resulting in the droplet to freeze instantaneously. Aggregation is mostly important for dendrites and happens when two ice particles with complex surface stick with each other after collision. Pflaum (1980) has found that the alternation of low-density riming and wet growth processes play a significant role in hailstone formation.

### 2.4.3 Hail in convective systems

Hail is the product of particle growth processes such as accretion or riming, i.e. the growth of large ice particles by rapid collection of supercooled water droplets. Several layers are found in a hailstone, with some being opaque and some being transparent. Opaque layers are a sign of dry growth. This occurs when the collection of supercooled droplets happens at a moderate rate, the water droplets freeze instantaneously on the ice particle and air bubbles are trapped in the process. Dry layers therefore have a lower ice density and are porous. Transparent layers indicate wet growth, which occurs when the collection of supercooled droplets is happening extremely fast. In this case, the latent heat released by the freezing process prevents instantaneous freezing of the water droplets. The excess water is often lost or flows into the underlying porous layer of a dry growth phase. Figure 2.7 shows a hailstone with different layers of dry and wet growth. The hail embryo itself can also be opaque or transparent. If the hailstone forms around a graupel embryo, the nucleus often has a conical shape and is opaque; if the hailstone forms around a large frozen water



Figure 2.7: Side view of a hail stone indicating different growth processes. Transparent layers are indicating dry growth at, opaque layers indicating wet growth. Picture taken and provided by Kaschuba (2013).

drop, the nucleus is more circular and transparent. The different pathways are shown in Figure 2.8 on the right side. Particularly large hailstones are often characterized by a strong irregularity, while small hailstones are usually rounder and symmetrical.

The structure of a convective system must be suitable to allow the formation of hail. The left part of Figure 2.8 describes three zones in a supercell that are elementary for hail formation. In the embryo formation zone (EFZ), low updrafts prevail so that graupel can develop with diameters of up to 5 mm. The strongest updrafts prevail in the hail growth zone (HGZ). Those hail embryos that make it from the EFZ into the HGZ can grow quickly here due to rapid accretion. Too weak updrafts in the HGZ cause the hailstones to fall out before they can reach a critical size, too strong updrafts cause the hailstones to be ejected into the anvil of the system where the amount of liquid water is insufficient for further growth. The fallout zone (FOZ) describes the area where the largest hailstones fall towards the ground.

Even if the explanation above refers to a supercell, in principle, hail formation is possible in all convective systems in which the updraft speed in the HGZ is similar to the theoretical fall velocity of the hailstones. In a single cell, this can happen when the updraft increases at a rate similar to the increase in hail fall speed. However, the largest hailstones commonly occur in super cells, when the hail embryos are located at the outer boundaries of the updraft and are transported upwards in a spiral-like path. At some point the hailstones reach the critical size where they can no longer be held by the updrafts and fall out under further accretion. Below the freezing line, the hailstones partly begin to melt and shed

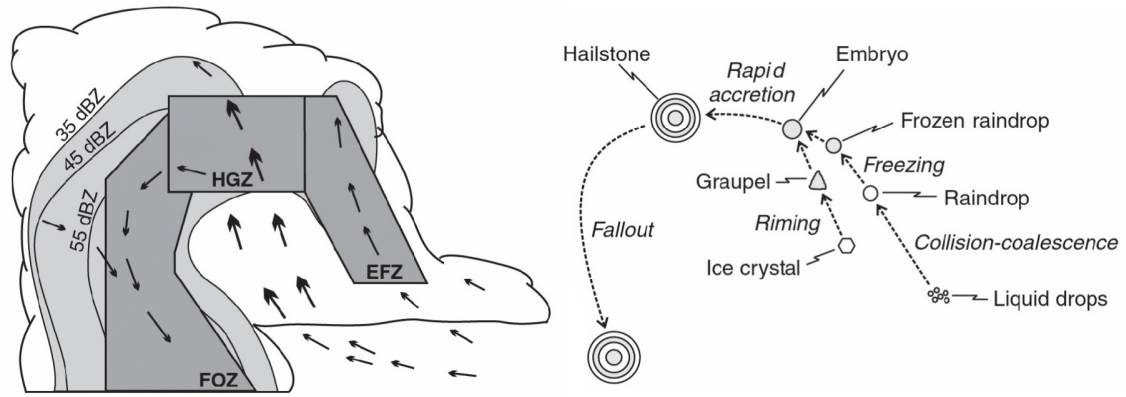


Figure 2.8: Hail formation areas within a supercell, arrows indicate air movements (left side). Possible pathway for a hailstone and its development within a convective system (right side). EFZ, HGZ and FOZ stand for embryo formation zone, hail growth zone and fallout zone, respectively. Figure by Lamb and Verlinde (2011) adopted by Young et al. (1993).

small water droplets. The height of the freezing line therefore has a slight influence on the hailstone size on the ground (Lamb and Verlinde, 2011).

## 2.5 Basics of Radar Meteorology

Weather radars (**radio detection and ranging**) make use of the fact that electromagnetic radiation in the microwave range is scattered by atmospheric particles such as hydrometeors. Weather radars such as those from the radar network of DWD emit electromagnetic radiation in a pulse-like form, which - if present - is backscattered by raindrops, snowflakes or hailstones in the atmosphere and is then detected again by the radar. The time delay between transmission and reception of the pulse provides information about the distance between the radar and the scattering particles. The intensity of the backscattered signal, on the other hand, provides information about the type and size of the scattering particle. The radars of the operate in the frequency range around 5.6 GHz (C-band), which corresponds to a wavelength of about 5.4 cm. With a typical hydrometeor diameter of 1 mm to 1 cm, the size parameter  $\alpha$  is found to be

$$\alpha = \frac{2\pi r}{\lambda} \quad (2.33)$$

with  $r$  as the particle radius and  $\lambda$  as the radiation wave length. For typical hydrometeors one finds  $\alpha \ll 1$ , which allows an analysis according to the laws of Rayleigh scattering. (cf. Section 2.5.1). However, it should be noted that the Rayleigh approximation is no longer sustainable for large hail, which instead has to be considered with respect to the Mie scattering regime.

The DWD operates a weather radar network consisting of 17 operational radar devices (as of 2021) which offer full coverage over almost entire Germany. The operational radar network was modernised from 2011 to 2015 by installing dual-pole Doppler radars of the type "EEC DWSR-5001C/SDP-CE" (Bartels et al., 2005). At the sites in Frankfurt, Hamburg, Berlin, Munich and Hannover, sites from densely urbanised areas were replaced by new sites in neighbouring locations with lower urban development (DWD, 2018, cf. Figure 2.9). To avoid large data gaps, two neighbouring radar units were never exchanged at the same time. If needed, failover radar systems were established to ensure good coverage. Extensive quality controls and filtering of undesired disturbance effects enable to significantly increase the quality of the collected data (Seltmann and Reidl, 1999), so that the precipitation data derived from the radar measurements can be regarded as suitable for the automated detection of thunderstorm and hail cells (cf. Wilhelm, 2021).

In order to obtain the most detailed information as possible about precipitation intensity and characteristics, the radar units are operated with two scanning modes. The precipitation scan is used for the quantitative determination of precipitation and is performed every 5 min for a fixed elevation angle between  $0.5^\circ$  and  $1.8^\circ$  (Bartels et al., 2005). In this context, it is worth noting that information from the lower troposphere is lost when operating at higher elevations (cf. Section 2.5.2).

The volume scan consists of ten elevation angles and starts with a measurement at  $5.5^\circ$ . This is followed by five measurements with decreasing elevation angles down to  $0.5^\circ$ , pro-

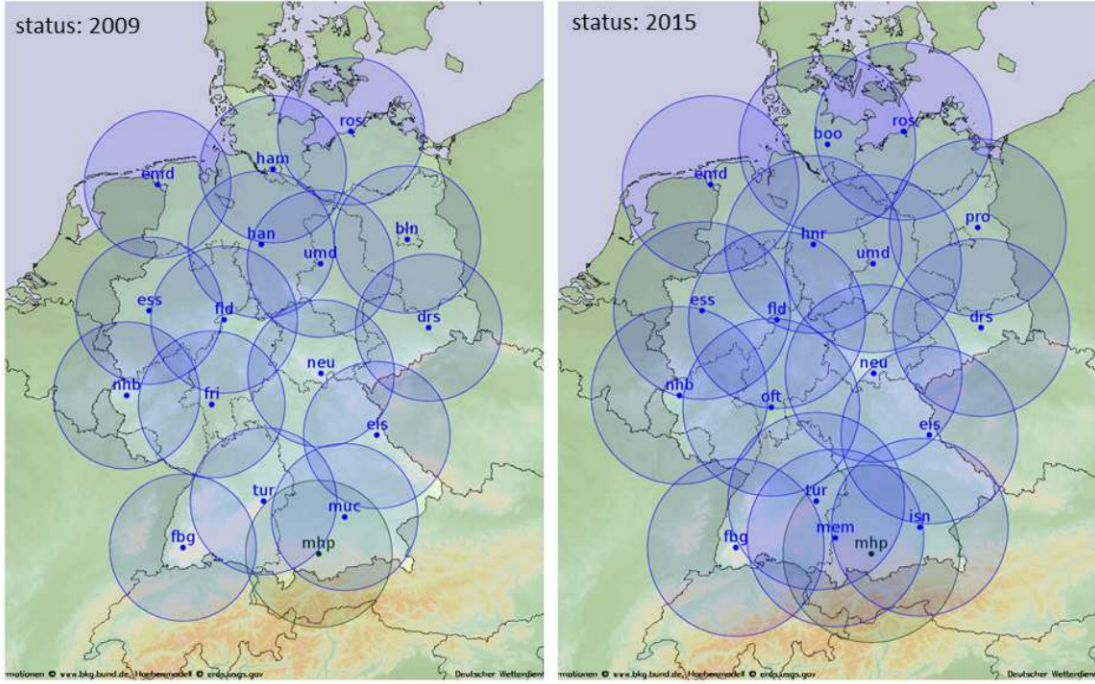


Figure 2.9: DWD’s national Radar network before and after modernization. Some sites (Frankfurt, Hamburg, Berlin, Munich, Hannover) were relocated slightly and the range of precipitation scan was increased from 125 km to 150 km with the change from the old Doppler radar to the new (Dual-Pol) polarimetric C-Band Doppler radar (DWD, 2018). Figure from Helmert et al. (2014).

viding information from the lower troposphere after 2.5 minutes. Subsequently, the missing four elevations from  $8.0^\circ$  to  $25.0^\circ$  are processed. Figure 2.10 provides an overview over the scan strategy and elevation angles.

By combining the measurements of all radar stations, DWD provides different radar products, so-called composites. The basis for the cell tracking algorithms KONRAD (**KON**vektive Entwicklung in **RAD**arprodukten, cf. Section 3.1.2, DWD, 2021a) is the RX-product, which represents the reflectivity factor  $Z$  across Germany on an equidistant grid with a resolution of  $1 \times 1$  km (Wilhelm, 2021). The modified version of the cell tracking algorithm TRACE3D (cf. Section 3.1.1) that is used in this work operates with the 3D radar composite of the DWD (Handwerker, 2002; Schmidberger, 2018).

### 2.5.1 Metrics in radar meteorology

The radar reflectivity  $\eta$  is a measure for the sum of all backscatter cross-sections  $\sigma$  of the scattering objects within the considered beam volume. According to the Rayleigh approximation, the backscatter cross-section of a hydrometeor is a function of the particle diameter  $D$

$$\sigma(D) = \frac{\pi^5}{\lambda^4} \left| \frac{n^2 - 1}{n^2 + 1} \right|^2 D^6. \quad (2.34)$$

Here  $D$  is the particle diameter and  $n$  the dielectric constant of the particle. The term

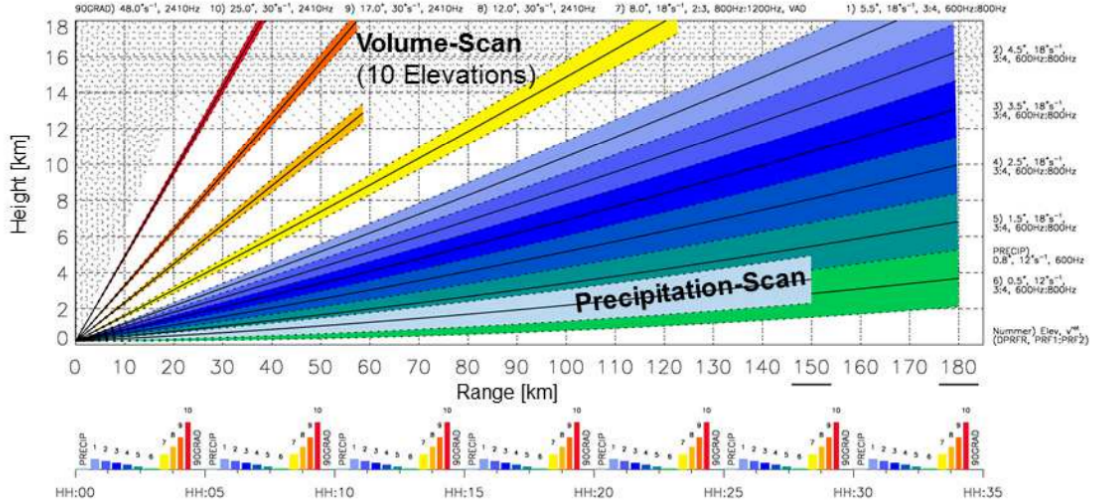


Figure 2.10: Schematic view of DWD's five-minute scanning strategy. The Volume-Scan is operated with ten different elevation angles to ensure good coverage of the vertical structure of the atmosphere. The Precipitation-Scan works with a single fixed elevation angle that depends on the orographic characteristics for each site (DWD, 2018). Figure from Helmert et al. (2014).

$$K = \frac{n^2 - 1}{n^2 + 1} \quad (2.35)$$

is defined as dielectric factor. Due to the different dielectric constants,  $K$  depends on the state of aggregation of the hydrometeors. For liquid water  $K$  is around 0.93, for ice it is approximately 0.19 (Doviak et al., 2006). However, for the determination of the radar reflectivity from radar measurements, DWD only applies the dielectric factor of water. In the case of frozen hydrometeors, this leads to a considerable underestimation of the reflectivity.

For the total volume covered by the radar beam, the radar reflectivity results from the product of the backscatter cross-section and the number density. With the number density

$$N = \int_0^\infty n(D) dD \quad (2.36)$$

one finds for the radar reflectivity

$$\eta = \frac{\pi^5}{\lambda^4} |K|^2 Z \quad (2.37)$$

with the reflectivity factor

$$Z = \int_0^\infty D^6 n(D) dD. \quad (2.38)$$

$Z$  has the unit  $\text{mm}^6 \text{m}^{-3}$  and varies over several orders of magnitude in this form. For this reason, the reflectivity factor is usually expressed in the logarithmic unit dBZ

$$Z_{\text{dBZ}} = 10 \log_{10} \left( \frac{Z}{\text{mm}^6 \text{m}^{-3}} \right). \quad (2.39)$$

The reflectivity factor  $Z_{\text{dBZ}}$  varies from slightly above 0 dBZ to 60 dBZ for light rain to heavy rain or hail and is negative in the case of no precipitation.

In order to estimate the precipitation intensity based on the reflectivity factor, the Z-R relationship is used

$$Z = aR^b. \quad (2.40)$$

$a$  and  $b$  are constants determined empirically and which depend on external factors such as precipitation type and cloud structure. The most common relationship by Marshall and Palmer (1948) uses  $a = 200$  and  $b = 1.6$ . It is based on an exponential decrease in droplet number  $n(D)$  with droplet size. For convective events, the relation from Sekhon and Srivastava (1971) is also often used, which uses  $a = 300$  and  $b = 1.35$ . The Z-R relationship used in the operational radar network of DWD is

$$Z = 256 \cdot R^{1.42} \quad (2.41)$$

and should represent the best possible compromise between stratiform and convective precipitation. For the most recent radar products, DWD now uses reflectivity-dependent parameters  $a$  and  $b$  with the objective to avoid an overestimation of precipitation intensities in convective precipitation and an overestimation in the stratiform case (Fruntko, 2021).

A common practice according to Mason (1971) is that reflectivity values above 55 dBZ are assumed to be related to hail. However, high reflectivity values alone do not indicate whether the precipitation is solid or liquid. The height and especially the vertical distribution of reflectivity can help in the determination process. The greater the vertical extent of the layer with reflectivity values above the threshold, the higher the probability of hail. Other criteria such as cloud top temperature and vertically integrated water vapor can also be considered (Kugel, 2012).

## 2.5.2 Errors

Scattering particles for the radar signal are not only hydrometeors in the atmosphere, but also aircraft, birds or insects. Furthermore, orography or buildings can cause objects from ground level to extend into the radar beams of the lower elevation angles (e.g. mountains, ships, skyscrapers or wind turbines), thereby causing ground clutter or erroneous signals. In the simplest way and for non-Doppler radars, the echoes from stationary objects can be removed by creating a reference map with the clutter data, which is then subtracted from the measured reflectivities. In DWD's radar network, however, the instruments are Doppler radars, which allows the quantification of the radial velocity of scattering particles. In this way, stationary objects or objects with unrealistic radial velocities (e.g. aircrafts) can be filtered out. However, not all interfering effects can always be eliminated entirely. As can be seen in Figure 2.11 the difference between an unfiltered radar data set

and a data set after correction by the quality assurance procedures applied by DWD can be significant (DWD, 2022).

A special case of ground clutter is the so-called anaprop echo (**anomalous propagation**). During weather conditions with strong inversion in the lower troposphere, the radar beams can be refracted stronger than usual and therefore still reach the ground in some places and generate ground echoes where this is normally not possible. In most cases, the usual ground echoes are also amplified.

Further problems are posed by shadowing and attenuation effects. Attenuation effects mean that precipitation located further away from the radar produces weaker echoes than nearby precipitation. This can lead to underestimations in rain rates or even to a lack of detection of a more distant thunderstorm. Shadowing (or shielding) effects can occur when an orographic obstacle shades the radar beam from the area behind it. This effect can be reduced by a dense radar network, so that each area of the investigation area is observed by several radars from different directions. If this is not the case, the reflectivities can be extrapolated from the measurements of higher layers or even from measurements of ground stations. However the latter is not performed by DWD in operational use.

A frequently observed phenomenon is the bright band. This is a horizontally aligned area with particularly high reflectivity in the vertical section of a radar image. It occurs at the altitude where sedimenting snow and ice particles begin to melt, because in this case the surface of the previously solid particles becomes liquid. In this process, the backscatter cross-section  $\sigma$  increases due to the change of the dielectric constant  $n$ . However, because the melting process has just begun, the particles still have a larger diameter than it would be the case with a liquid water drop. The combination of large particle size and liquid surface then provides very high reflectivity values in this area. The bright band is usually about 200 m to 500 m below the freezing line.

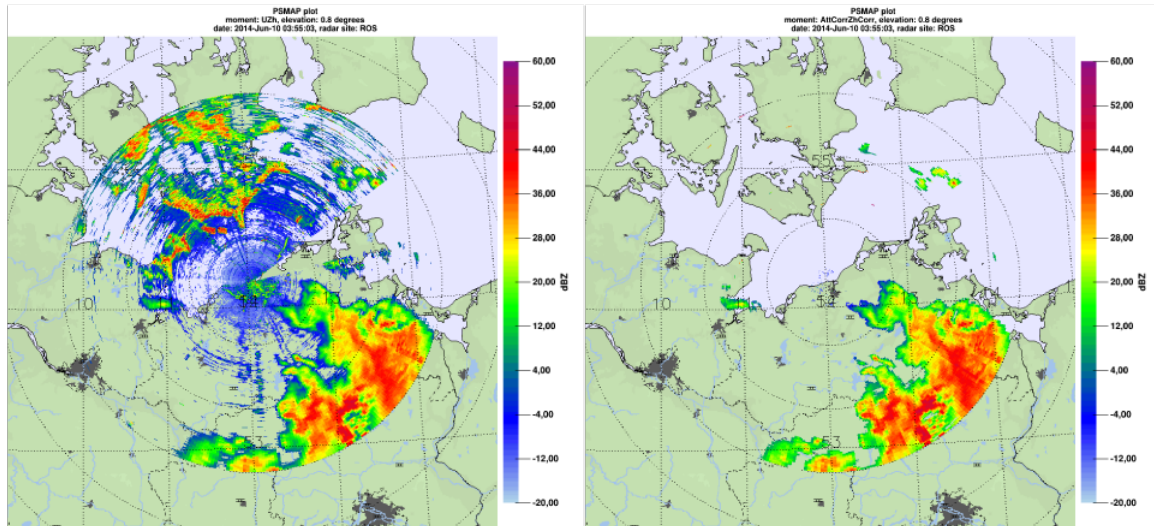


Figure 2.11: Radar reflectivity with (right side) and without (left side) quality assurance from DWD’s radar site in Rostock, 10 June 2014, 05:55 MESZ. In the left image, strong ground echoes are visible (DWD, 2022).

## 2.6 Convection above complex terrain

The presence of mountains can have a major impact on the development of deep moist convection. In an environment with weak ambient winds or high static stability, a mountain range can decelerate or even block the flow. Similarly, an obstacle can force the flow to go around or over itself (Smith, 1989). The elevation layers above the obstacle can be affected as well. In a low wind speed environment it is also possible that air movements are induced by thermally driven mountain-valley wind circulations. In the following, the interactions between an obstacle and an existing wind field will be discussed and their influence on the initiation of deep moist convection will be elaborated.

### 2.6.1 Wind field modification by mountains

In an environment with considerable ambient wind, the presence of an obstacle can generate vertical motion. The type of interaction between the wind field and the obstacle depends on meteorological parameters such as wind speed and direction as well as stability, but also on the properties of the obstacle. A measure that can be used to estimate the type of interaction is the Froude number  $Fr$ , which is introduced in Section 2.6.2. Figure 2.12 shows an overview of different possibilities how a mountain range in a horizontal wind field can favour convective processes (Kunz, 2003).

On the upstream side and above the obstacle, convective processes can be triggered by flow deceleration or even blocking when moist and unstable air masses are forced against an obstacle (Figure 2.12 (a), orographic rain).

Since the streamlines at higher layers are affected by an obstacle already further upstream because of the tilted streamlines, convection can also form in certain cases far upstream of the obstacle (Figure 2.12 (b), Smith, 1979).

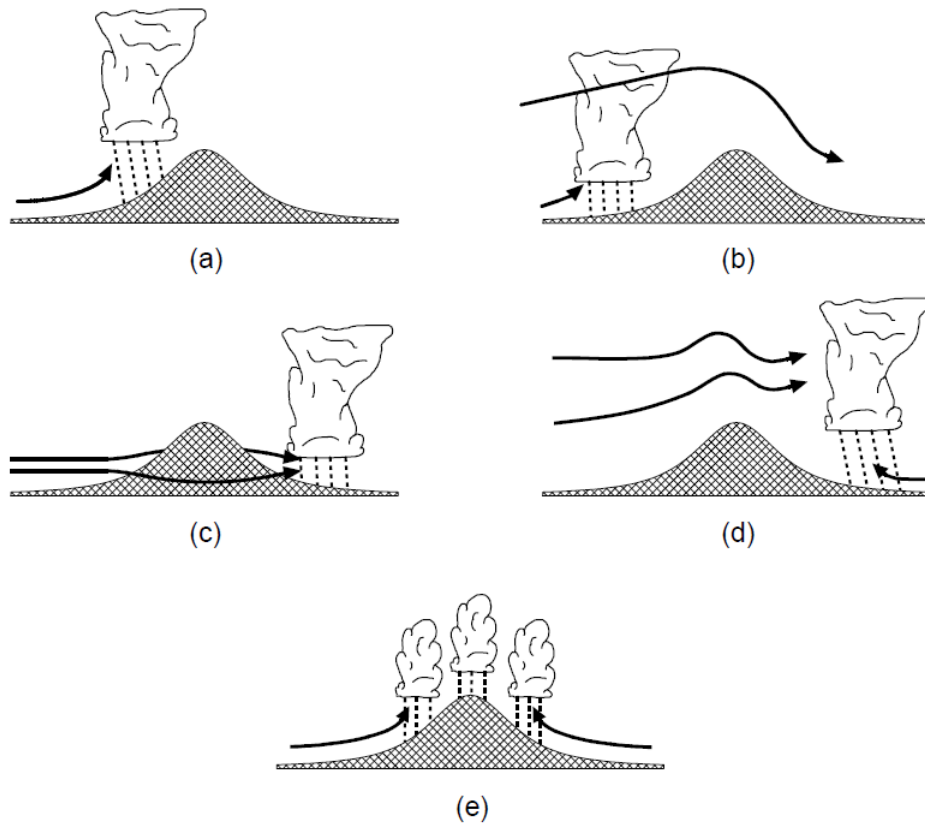


Figure 2.12: Different types of interaction between an obstacle and the initiation of convection by deceleration of the flow at the upwind side (a), deceleration and wave formation at the upwind side (b), flow around the obstacle with convergence on the downwind side (c), wave formation above and on the downwind side (d) or based on mountain-valley circulation by thermally heating of elevated areas (e). Graphic by Kunz (2003) adopted from Houze (1994).

In the case of low Froude numbers, a flow around the obstacle can develop. This leads to convergence areas in the lee of the obstacle. Assuming incompressibility of the air and for continuity reasons, upward motion follows, which can have a convection-favouring effect as shown by Kuo and Orville (1973) for the Black Hills (South Dakota and Wyoming, USA, Figure 2.12 (c)).

In the case of high Froude numbers, the flow tends to go over the obstacle rather than around, which can also lead to convection initiation in the lee of the mountains by inducing gravity waves. According to Peristeri et al. (2000), in case of an overflow, labilization often occurs in the lee of obstacles due to vertical stretching of the air column (Figure 2.12 (d)).

Direct thermal effects such as a mountain-valley circulation can also have a convection-favouring effect through differential heating on inclined and higher elevated slope surfaces (Figure 2.12 (e)).

## 2.6.2 Froude number

Considering an obstacle with a certain vertical extent in a flowing fluid, it depends on various factors whether the fluid can flow over the obstacle or not. Generally spoken, the ratio between horizontal velocity  $U$  perpendicular to the obstacle and the product of the scaling height of the obstacle  $H$  and the gravitational force  $g$  is decisive. The Froude number  $Fr$

$$Fr = \frac{U}{\sqrt{gH}} \quad (2.42)$$

is a dimensionless parameter, which combines these parameters (Markowski and Richardson, 2010).

In the meteorological context, the effort required for the flow to go over the obstacle cannot be characterised so broadly. In this case, the vertical acceleration of an air parcel does not depend on the acceleration due to gravity  $g$ , but on the buoyancy  $B$  and thus on the static stability (cf. Section 2.1.4). Additionally energy is lost by the increase of dynamic pressure upstream of the obstacle. Replacing the gravitational acceleration  $g$  in Equation 2.42 with the buoyancy acting during a vertical deflection by the height  $\Delta z$

$$B = \Delta z \frac{g}{\theta} \frac{\partial \theta}{\partial z} \quad (2.43)$$

and equalling  $\Delta z = H$  leads to the Froude number

$$Fr = \frac{U}{H \sqrt{\frac{g}{\theta} \frac{\partial \theta}{\partial z}}}. \quad (2.44)$$

Inserting the Brunt-Vaisala-Frequency  $N$  (cf. Equation 2.23) simplifies the equation to

$$Fr = \frac{U}{HN}. \quad (2.45)$$

In this form, the Froude number  $Fr$  can be interpreted as a characteristic parameter for the flow dynamics. Thereby, the following applies:

- $Fr < 1$ : Characteristic velocity of the flow is not sufficient to make it over the top of the mountain  $\rightarrow$  Tendency to flow around the mountain
- $Fr > 1$ : Characteristic velocity of the flow is sufficient to make it over the top of the mountain  $\rightarrow$  Tendency to flow over the mountain.

For  $Fr \approx 1$  no clear decision can be made. In General, the interaction with the obstacle can have a major influence on the formation of clouds, precipitation and thunderstorms. The interrelationships are very complex and not yet fully understood. In the case of overflow, rising air masses can lead to orographic precipitation from the upwind side to the crest of a mountain. Downstream of the obstacle, lee waves can also interact with cloud and precipitation formation (Muccilli, 2015). In the case of a flow around the obstacle,

areas of divergence and convergence develop in the horizontal wind field. In this case, convection can be triggered by flux or moisture flux convergence, respectively, in the lee of the obstacle. The critical value of  $Fr$  at which the flow is not only decelerated, but completely blocked, has not yet been sufficiently clarified (Lin and Wang, 1996).

### 2.6.3 Surface-near horizontal moisture flux convergence

The divergence of a three-dimensional wind field is described by

$$\nabla \cdot \vec{v} = \frac{\partial u}{\partial x} + \frac{\partial v}{\partial y} + \frac{\partial w}{\partial z}, \quad (2.46)$$

where the law of mass conservation requires  $\nabla \cdot \vec{v} = 0$ . Thus, divergence of the horizontal wind field

$$\nabla \cdot \vec{v}_h = \frac{\partial u}{\partial x} + \frac{\partial v}{\partial y} = -\frac{\partial w}{\partial z} \quad (2.47)$$

creates negative vertical motion. In reverse, any presence of negative divergence, which is convergence, leads to positive (=upward) vertical motion. Therefore, in a suitable environment, a converging horizontal wind field can serve as trigger for the initiation of thunderstorms (Doswell, 1982).

Since a sufficient amount of moisture is also necessary for the development of thunderstorms, the horizontal moisture flux convergence (MFC) will be investigated in this work

$$\text{MFC} = \nabla \cdot (q\vec{v}_h) = q\nabla \cdot \vec{v}_h + \vec{v}_h \cdot \nabla q \quad (2.48)$$

$$= \underbrace{q \left( \frac{\partial u}{\partial x} + \frac{\partial v}{\partial y} \right)}_{\text{convergence term}} + \underbrace{u \frac{dq}{dx} + v \frac{dq}{dy}}_{\text{advection term}} \quad (2.49)$$

which is composed of two terms. The convergence term describes the product of horizontal flux convergence and specific moisture  $q$ . The advection term incorporates changes in the moisture field with time, or the fluctuations of the moisture field. Although the convergence term is usually dominant, a significant influence of the advection term could be found in regards to the development and also the intensification of thunderstorms (Bothwell, 1988; Waldstreicher, 1989). MFC can also be used as an indicator for the prediction of thunderstorm initiation (Banacos and Schultz, 2005; Wei et al., 2016).

## 2.7 COSMO-DE Model

The regional model COSMO-DE (**C**Onsortium for **S**mall-scale **M**Odelling, COSMO, 1998) was developed by DWD under the name "Lokal-Modell Kürzefrist" (LMK). On 16 Jan 2007 the LMK was taken into operational use by the DWD and from then on complemented the already existing model systems. In the course of a name change in 2007, the LMK became the COSMO-DE. Since the analyses of the COSMO-DE model provided by the DWD contain only a few parameters that are related to convection, extended analyses of Wilhelm (2021) are used in this work, which were supplemented by

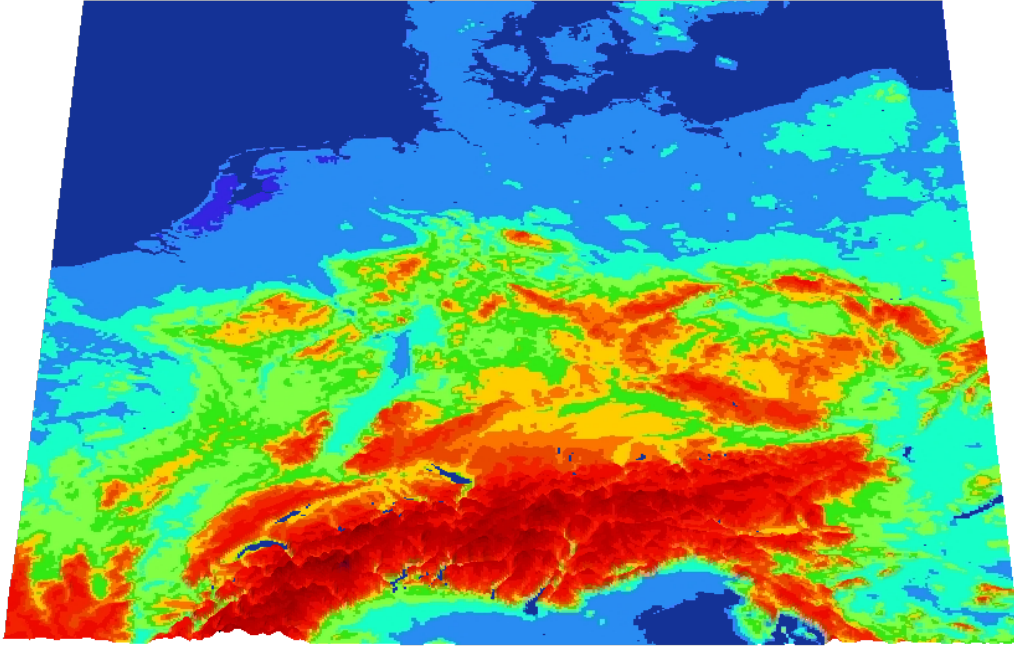


Figure 2.13: Model domain of COSMO-DE. Colors indicate model surface height above sea level. (DWD, 2021b).

various convection-relevant parameters such as the low level lapse rate, deep layer shear and vertically averaged wind means.

### 2.7.1 Model overview and differences to COSMO-EU

The main differences between COSMO-DE and COSMO-EU are in the grid mesh size, the covered model area (cf. Figure 2.13) and the forecast horizon. The number of vertical layers in COSMO-DE is 50 (COSMO-EU: 40). The data assimilation includes the assimilation of 5-minute high-resolution 2D radar data composites with usage of latent heat nudging (Schraff, 2005). In contrary to COSMO-EU, the parametrization for deep moist convection is completely switched off, since the model resolves the coarse structure of deep-moist convection explicitly. For shallow convection a slightly modified version of the parametrization is used (Schraff, 2005). As can be seen in Figure 2.13, the COSMO-DE model domain covers Germany, most of the Alpine region as well as Switzerland and Austria. Large parts of the other neighbouring countries are also covered. The horizontal resolution of 2.8 km results in a good understanding of the orographic conditions.

### 2.7.2 Basic equations

A mathematical description of atmospheric movements is achieved by considering the atmosphere as a continuum of different components. These components are dry air as well as water in all three aggregate states. From the external side, the system is driven by forces such as gravity and the Coriolis force. Internal processes triggered by transfer

of sensible and latent heat as well as mass and momentum must also be considered. The basic system of equations is therefore composed of the conservation laws for momentum, mass and heat (Doms, 2018):

$$\rho \frac{d\vec{v}}{dt} = -\nabla p + \rho \vec{g} - 2\vec{\Omega} \times (\rho \vec{v}) - \nabla \cdot \vec{t} \quad (2.50)$$

$$\frac{d\rho}{dt} = -\rho \nabla \cdot \vec{v} \quad (2.51)$$

$$\rho \frac{dq^x}{dt} = -\nabla \cdot \vec{J}^x + I^x \quad (2.52)$$

$$\rho \frac{de}{dt} = -p \nabla \cdot \vec{v} - \nabla \cdot (\vec{J}_e + \vec{R}) + \epsilon \quad (2.53)$$

Here,  $x$  represents the different components of the continuum. Thus, it can be

$$\begin{aligned} x &= d && \text{for dry air,} \\ x &= v && \text{for water vapour,} \\ x &= l && \text{for liquid water and} \\ x &= i && \text{for frozen water, i.e. ice.} \end{aligned}$$

In Equation 2.50 to 2.53 the following symbols are used:

- $t$  : time
- $q^x$  : mass fraction of constituent  $x$
- $\vec{v}$  : velocity relative to the rotating earth
- $\vec{g}$  : apparent acceleration of gravity and centrifugal force
- $\vec{\Omega}$  : angular velocity of earth rotation
- $\vec{t}$  : stress tensor due to viscosity
- $I^x$  : sources / sinks of constituent  $x$
- $J^x$  : diffusion flux of constituent  $x$
- $\vec{J}_e$  : heat flux
- $\vec{R}$  : flux density of solar and thermal radiation
- $\epsilon$  : kinetic energy dissipation due to viscosity

Assuming a stationary, horizontally homogeneous and dry initial state, which is hydrostatically balanced, the thermodynamic variables pressure  $p$ , temperature  $T$  and density  $\rho$  are thus each composed of a height-dependent reference value of the initial state and a location-dependent deviation.

$$T = T_0(z) + T'(\mathbf{x}, t) \quad (2.54)$$

$$p = p_0(z) + p'(\mathbf{x}, t) \quad (2.55)$$

$$\rho = \rho_0(z) + \rho'(\mathbf{x}, t) \quad (2.56)$$

With the equation of state for an ideal and the basic equation of hydrostatics

$$\frac{\partial p_0}{\partial z} = -g\rho_0 = -\frac{gp_0}{R_d T_0} \quad (2.57)$$

describes the relation between  $T_0(z)$ ,  $p_0(z)$  and  $\rho_0(z)$ , where  $R_d$  describes the gas constant for dry air.

### 2.7.3 Geographic coordinates with rotated pole

Both COSMO-DE and COSMO-EU, make use of rotated spherical coordinates. The equations shown in Section 2.7.1 were formulated for a rotating system and are therefore also valid for an arbitrarily rotated coordinate system. It is apparent that ordinary spherical coordinates are the simplest and most convenient way to consider the (nearly) spherical shape of the Earth. However, when using spherical coordinates, numerical problems arise due to the confluence of meridians at the poles and the resulting singularities.

The COSMO-DE grid is created by rotating the conventional geographic coordinate system  $(\lambda_g, \varphi_g)$ , resulting in the coordinate-North-pole of the rotated system  $(\lambda, \varphi)$  to be located in the Pacific Ocean, at  $\lambda_N = 170^\circ\text{W}$  and  $\varphi_N = 40^\circ\text{N}$  of the conventional geographic coordinate system (Schraff, 2005). An equidistant grid with mesh size

$$\Delta\lambda = \Delta\varphi = 0.025^\circ \approx 2.8\text{km} \quad (2.58)$$

is established in the new rotated coordinate system, which can be seen in Figure 2.14.

Transformation from the rotated coordinate system  $(\lambda, \varphi)$  to the geographic coordinate system  $(\lambda_g, \varphi_g)$  can be performed with geometric relations based on the spherical trigonometry:

$$\lambda_g = \lambda_N - \arctan\left(\frac{\cos\varphi \sin\lambda}{\sin\varphi \cos\varphi_N - \sin\varphi_N \cos\varphi \cos\lambda}\right), \quad (2.59)$$

$$\varphi_g = \arcsin(\sin\varphi \sin\varphi_N + \cos\varphi \cos\lambda \cos\varphi_N,) \quad (2.60)$$

such as the re-transformation from geographic coordinates into rotated coordinates

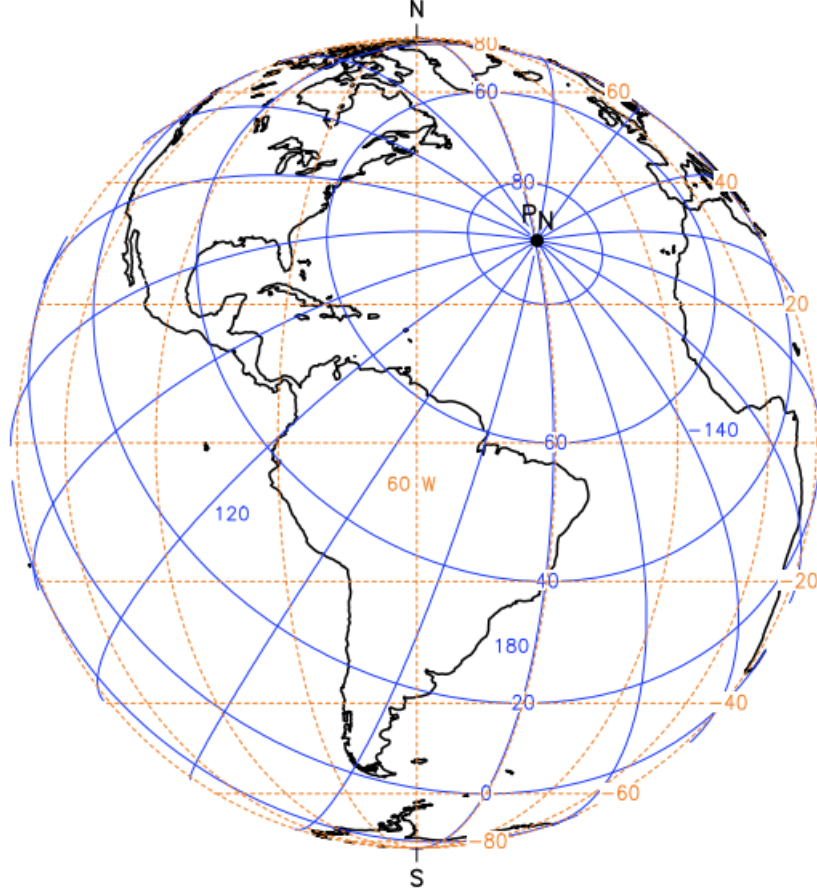


Figure 2.14: Rotated longitude and latitude (full lines, at a contour interval of  $20^\circ$ ) for a spherical coordinate system with the North pole shifted to the point  $P_N$ . Broken lines indicate longitude and latitude of the geographical system (at a contour interval of  $20^\circ$ ) (Doms, 2018).

$$\lambda = \arctan\left(\frac{-\cos\varphi_g \sin(\lambda_g - \lambda_N)}{-\cos\varphi_g \sin\varphi_N \cos(\lambda_g - \lambda_N) + \sin\varphi_g \cos\varphi_N}\right), \quad (2.61)$$

$$\varphi = \arcsin\left(\sin\varphi_g \sin\varphi_N + \cos\varphi_g \cos\varphi_N \cos(\lambda_g - \lambda_N)\right). \quad (2.62)$$



## 3 Data and Methods

As part of this work, different data sets and methods were combined for the analysis of the frequency and spatial distribution of thunderstorm and hail tracks in Germany. Data based on the cell tracking algorithms TRADE3D according to Schmidberger (2018) and KONRAD according to Wilhelm (2021) allows to estimate hail and thunderstorm track. The sample of the former data mainly comprises organized thunderstorms with a high potential for hail on the ground, while the latter includes isolated convection in terms of single sells (cf. Section 2.3.1) and supercells (cf. Section 2.3.3). The event set based on TRACE3D ranges from 2005 to 2020, the event set based on KONRAD from 2011 to 2016, both for the summer months (April to September), where severe convective storms occur frequently. TRACE3D's cell tracking data includes the date and time of the first detection, the coordinates of the center of the track, the length and width of the track, and the average displacement direction and speed. The location of the first detection can be calculated from this information. The temporal resolution is 15 min. KONRAD's cell tracking data includes the date and time of the first detection and, for each subsequent detection, the coordinates of the cell, the duration, and the displacement direction and velocity. The temporal resolution is 5 min. By means of hourly available analyses of the high-resolution numerical weather forecast model COSMO-DE, environmental conditions are examined during and especially prior convection initiation. This data is available for the time period of 2011 to 2017.

### 3.1 Cell detecting and tracking

In order to automatically produce contiguous tracks for thunderstorms from radar or satellite images, so-called cell tracking algorithms are required. The first attempts of tracking storms by weather radar data or satellite observations goes back to Rinehart and Garvey (1978). The pattern recognition was based on finding the maximum correlation coefficient between an initial array of reflectivity factors and another array in the following time step. There, all arrays in the potential target area were searched, and the one with the maximum correlation coefficient was determined as the new position. By linking the centers of the estimated positions for each time step, the track of a storm could be recreated. With the evolution of discrete objects, i.e. objects with definable boundaries, a second generation of tracking algorithms has been developed (Dixon and Wiener, 1993; Johnson et al., 1998). The cell tracking algorithms TRACE3D and KONRAD, which are described in the following section, are algorithms of this second generation.

### 3.1.1 Cell detecting and tracking algorithm TRACE3D

TRACE3D tracks convective signals in volumetric radar data (Handwerker, 2002). Originally developed for usage in spherical coordinate from a single radar, the algorithm was adopted by Schmidberger (2018) for usage in Cartesian coordinates of radar composites from multiple radar sources (such as DWD radar composites, cf. Section 2.5). The method uses a reflectivity threshold  $Z_{\text{threshold},1}$  to separate the total radar image into single regions of intense precipitation (ROIP). This threshold is usually set to rather low values (e.g. 35 dBZ) to identify convective cells already in early stages of their development. However, this leads to the problem that also stratiform precipitation may be detected and furthermore undesired echoes such as the bright band are detected. For this reason, another threshold  $Z_{\text{threshold},2}$  is defined for each ROIP with  $Z_{\text{threshold},2} > Z_{\text{threshold},1}$  based on the maximum reflectivity within that ROIP. Thus, in each ROIP there can be several contiguous areas that have a reflectivity greater than  $Z_{\text{threshold},2}$ , so-called reflectivity cores (RCs). Figure 3.1 demonstrates the different methods for defining RCs using an exemplary one-dimensional data set.

To retrieve the RCs, which were detected in the first step (called "parents") in a subsequent radar image, TRACE3D uses a similar principle as the Storm Cell Identification and Tracking Algorithm (SCIT) of Johnson et al. (1998). Based on the movement of cells in previous time steps, the velocity of each RC is estimated and extrapolated. RCs are then searched for within a circle of a pre-defined search radius in the new time step. If the algorithm finds a potentially suitable RC in the new radar image (called "children"), it verifies whether parents and children match based on size and intensity. If this is not the case, the algorithm takes into account a potential storm splitting or storm merging. If there is more than one potential child for a parent, the parent element is moved to the volume-weighted centre of the children found. If the covered area of each child is significantly smaller than that of the parent, cell splitting is assumed. The detection of cell mergings follows the same principle in the opposite direction.

If there are several RCs within a ROIP, the assignment of parents and children can become more difficult, as the algorithm may assign parents and children crosswise. Crossing of tracks is possible in reality, since the track of a thunderstorm cell does not always strictly follow the mean flow. In the case of supercells, the track may deviate from the general flow direction by up to  $45^\circ$  (Bunkers et al., 2002). The TRACE3D algorithm generally tends to find more connections between parents and children than reasonable, which is why parent-child assignments that indicate a crossing of the tracks are deleted (cf. Figure 3.2).

Handwerker (2002) estimated the TRACE3D algorithm to create assignments between parent RCs and child RCs closely to human-level assignment. The critical success ratio (CSI) of assignments was found to be between 0.85 and 0.96 for testing data sets. Human persons achieved CSI values between 0.91 and 0.99 for the same data sets.

The data set created by Schmidberger (2018), which is used as the basis in this work, was generated with a modified version of TRACE3D. For the use of the reflectivity composite,

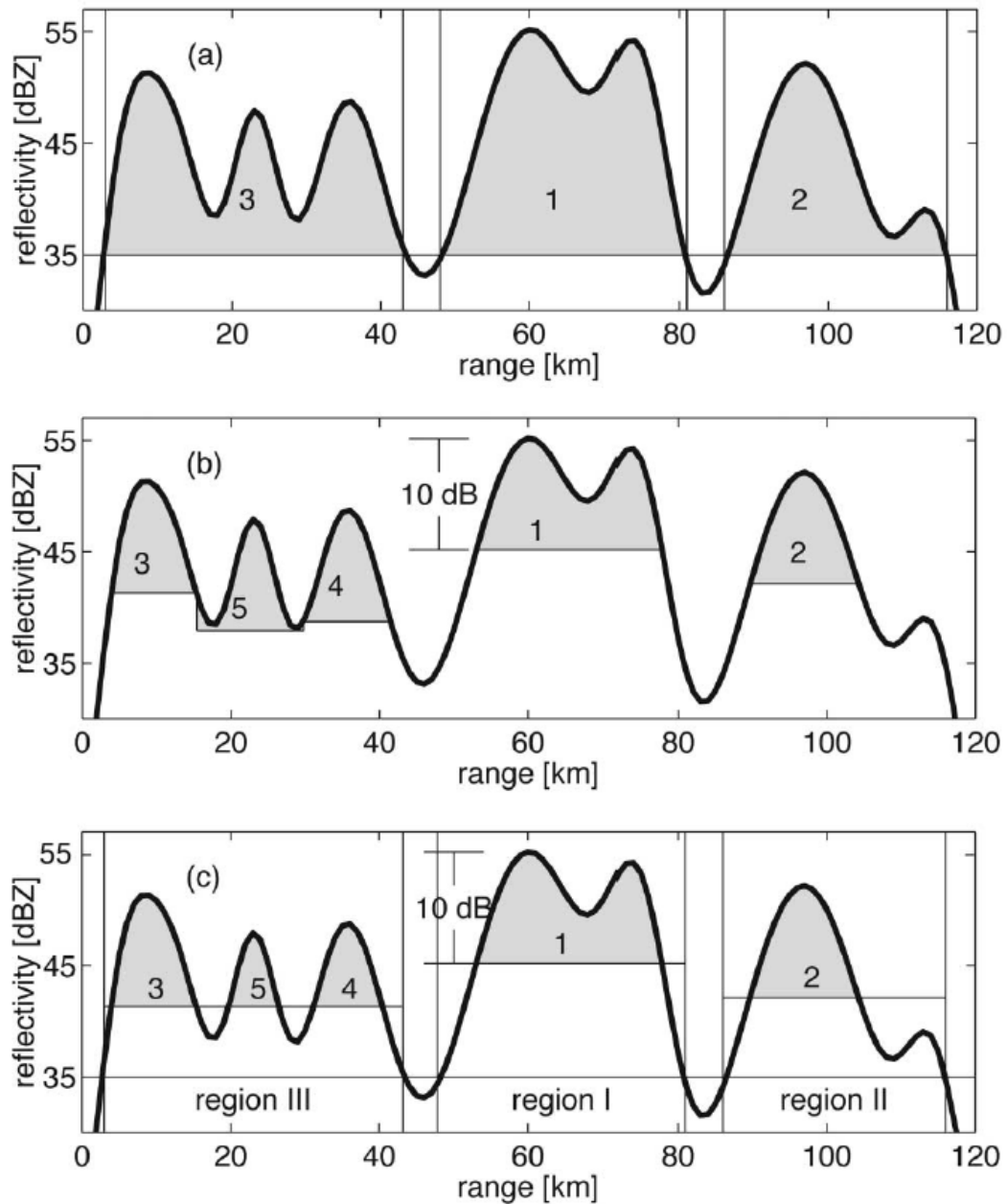


Figure 3.1: Schematic sketch of possible methods to define reflectivity cores demonstrated on a unique onedimensional data set. (a) Each beam volume element with a reflectivity above a certain threshold  $Z_{\text{threshold},1}$  (35 dBZ) is part of an RC. (b) "The upper 10 dB" ( $Z_{\text{max, RC}} - Z_{\text{diff}}$  with  $Z_{\text{diff}} = 10 \text{ dBZ}$ ) are taken as RC. This might lead to RCs that include the lower regions of more prominent adjacent RCs as can be seen with RC 5. (c) In a first step, contiguous regions with a reflectivity value above a threshold  $Z_{\text{threshold},1}$  (35 dBZ) are searched for. Within each region, a second threshold  $Z_{\text{threshold},2} = Z_{\text{max, ROIP}} - Z_{\text{diff}}$  beneath the maximum reflectivity within that region, is used to define RCs. In this way, TRACE3D defines RCs. Figure and description from Handwerker (2002).

the so-called PZ-product of DWD, on the one hand, different reflectivity classes had to be dealt with, on the other hand, a change from spherical coordinates to Cartesian coordi-

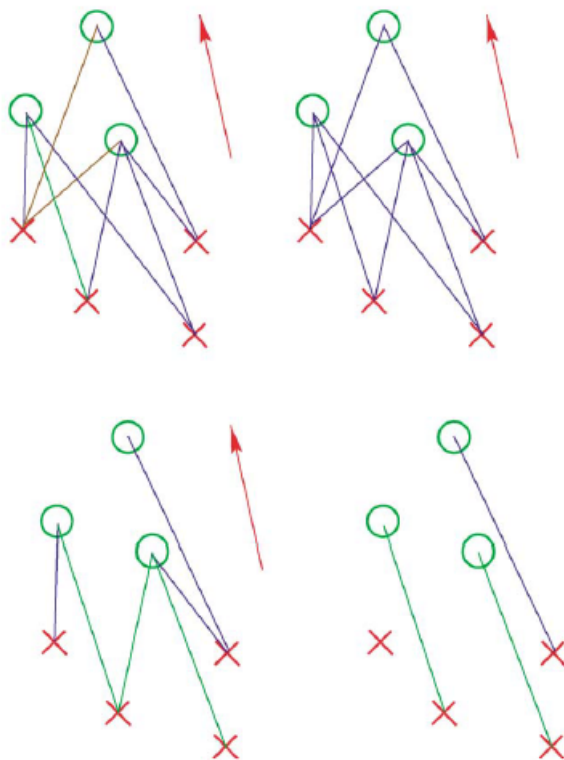


Figure 3.2: Illustration of the removal of crossings. Green circles mark the positions of child RCs, red crosses the positions of parent RCs. The red arrows indicates the direction of the mean flow. Those assignments with the least correlation to the mean flow (in terms of direction and velocity) are being removed. If there still remain more than three parents and more than three children (lower left), splitting and merging is forbidden. Figure and description (with slight changes) from Handwerker (2002).

nates had to be performed. The boundaries between the individual reflectivity classes are predefined at 7, 19, 28, 37, 46 and 55 dBZ. A consideration according to the criterion by Mason (1971) for two-dimensional radar data would suggest that only the highest reflectivity class may be considered here. However, since the vertical extent of reflectivity is also considered, the criterion by Waldvogel et al. (1979) should be noted, which is based on the vertical extent of the 45 dBZ reflectivity area. Focusing on potentially damage-relevant hail tracks, the threshold  $Z_{\text{threshold},1} = 52 \text{ dBZ}$  was set higher than in Handwerker (2002). The second threshold was defined via the threshold difference  $Z_{\text{diff}} = 10 \text{ dBZ}$ . In this way, RCs of the highest class are detected, adjacent reflectivity values of the second highest class are added to them.

### 3.1.2 Cell detecting and tracking algorithm KONRAD

While the TRACE3D algorithm is particularly suitable for the detection of convective systems with several cores due to the use of multiple thresholds, the cell tracking algorithm KONRAD is mainly specialized on finding and tracking isolated convection. The system was developed and is in operational use by the DWD. It is a procedure for the automated detection, tracking and forecasting of thunderstorm cells on the basis of weather radar data. In addition to information about the intensity and direction of a thunderstorm, it

also provides warnings regarding hail, heavy rain and wind gusts and more (Lang, 2003). The method thus represents an important tool for the severe weather warning process at DWD.

The Germany-wide RX-product (cf. Section 2.5), serves as data basis. In a first step, so-called primary cells are detected. The condition for this is a radar reflectivity of  $Z_{\text{primary}} \geq 46$  dBZ at 15 neighbouring grid points at least. The radar reflectivity  $Z_{\text{primary}} = 46$  dBZ corresponds approximately to a precipitation intensity of  $RR = 23 \text{ mmh}^{-1}$  (Wilhelm, 2021). Each detected thunderstorm cell is assigned a reflectivity-weighted centre and a rectangular frame that completely encloses the cell while keeping its area as small as possible. Since the (usually) 5 min interval between radar images makes it impossible to determine the exact time of origin, each cell detected for the first time is assigned the age  $t_{\text{start}} = 2$  min as a general rule. Each registered centroid is then searched for again in a certain radius in the following time step. This radius is defined by a maximum realistic displacement velocity of  $v_{\text{max}} = 110 \text{ kmh}^{-1}$  for the detected cell and an additionally considered displacement of the centroid within the cell. If a cell with a matching spatial extent is found within this radius, the cell is considered to be the continuation of the cell detected in the first step, and the cell age is increased by 5 min. For cells with associated cell tracks from previous positions, track predictions can be performed. The individual primary cells are also analysed further. Thus, there is a classification into an intensity class as well as an assignment of an intensity trend.

If no suitable centroid can be found for an already detected primary cell in a subsequent image, this is treated as a dissipating cell. In the opposite case, a cell is considered as a new formation.

The application range of KONRAD is extended by detecting so-called secondary cells with a second threshold of  $Z_{\text{secondary}} > 37$  dBZ. This is used for the early detection of approaching thunderstorms. The use of a third threshold  $Z_{\text{hail}} \geq 55$  dBZ enables the detection of (potential) hail events and the automated warning thereof.

The KONRAD cell tracking algorithm data used in this work is identical to the KONRAD data sets filtered by Wilhelm (2021). Both the natural dynamics of the convective cells and simple technical conditions (radar failures, boundary areas) lead to uncertainties in the cell tracking procedures. Therefore, during the quality control of the data, particularly the following points had to be taken into account and corrected if necessary:

- Starting and/or ending point of cells beyond the covered area
- Cell track traverses uncovered areas
- Cell lifetime is covered by only one time step
- Cell merging and cell splitting
- Unrealistic cell assignments between two timesteps

With the aim to obtain a sample that not only allows conclusions to be drawn about the track of the thunderstorm cells, but also to provide information about the visible life cycle of a cell, a rather strict filtering was applied. All cell objects were sorted out that were registered for the first time at a time step from which no data on the previous time step was available. Similarly, cell objects were sorted out whose last registration fell on a time step at which no data on the subsequent time step was available. Furthermore, all cell objects were deleted whose tracks lead into a permanently data-less area or originates from such an area.

In addition, a filtering of particularly short life cycles took place. All cell objects that were only detected at a single time step were deleted, as the definition of a life cycle was meaningless.

A cluster filter was used to remove cell objects that were potentially involved in cell splitting or cell merging. All cells that were too close to a neighbouring cell at the first or last time of detection were deleted. Consequently, the neighbouring cell also had to be deleted in this case, as it may have arisen from cell splitting with another object or could merge with the original cell object in the next time step. The search for neighbouring cells was performed in a rectangular field with the edge length  $0.5^\circ$  according to the geographical coordinate system around the cell's centroid. The exclusion criterion was a distance between neighbouring cells of less than 5 km.

Filtering was also performed with respect to cell area and displacement. Cell objects with a closed area of more than  $A_{\text{crit}} = 40 \text{ km}^2$  at the time of the first or last detection were removed, because the formation or dissipation of a convective core of this spatial extent is considered unrealistic according to the general knowledge about the life cycle of convective cells. Similarly, the database is cleared of cells where a change in cell area of more than

$$\left| \frac{dA}{dt} \right| = 10 \text{ km}^2 \text{ min}^{-1} \quad (3.1)$$

occurs between two time steps.

Last but not least, obvious misassignments were removed. In isolated cases it occurred that independent cells were assigned the same cell ID by KONRAD. In extremely rare cases, even cells that are several 100 km apart between two time steps were associated with each other.

Filtering reduced the data set spanning the summer half-year 2011 to 2016 from 165 572 to 38 553 cell object entries. The largest shares of filtered objects are based on filtering due to short lifetime (only one time step) and the cluster filter. More detailed information on the filtering methods and the remaining data set can be found in Wilhelm (2021).

## 3.2 Analysis and processing of cell tracking data

The analysis results of the COSMO-DE model are available for the months from April to September from 2011 to 2017 and thus cover a period of 7 years. Cell tracks based on the KONRAD cell tracking is available for the period from 2011 to 2016, whereas the tracks

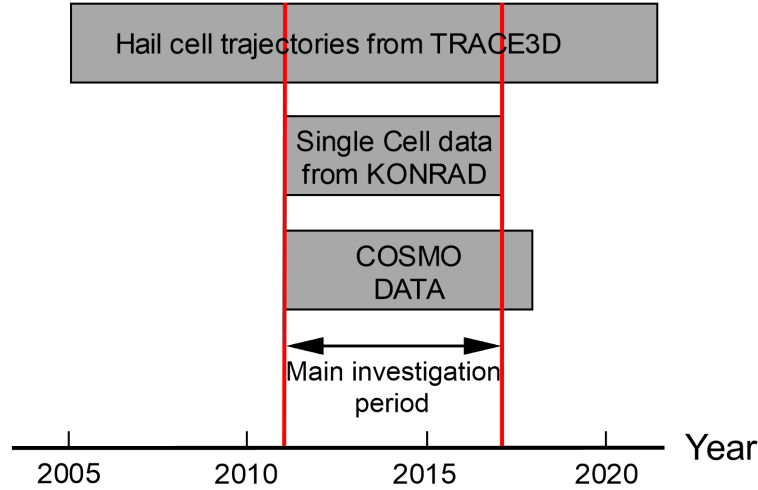


Figure 3.3: Overview of the availability of the individual data sources. The main investigation period from 2011 to 2016 inclusive is marked with red bars.

based on TRACE3D are available from 2005 to 2020 (cf. Figure 3.3). The intersection of all three time spans, the years 2011 to 2016, are the main study period of this work.

During the main investigation period, the available KONRAD database shows 38553 thunderstorm entries throughout Germany. For the data set according to TRACE3D, there are 8164 tracks over the entire period from 2005 to 2020, and 2793 tracks for the duration of the main investigation period. The large difference in the number of tracks is due to the type of detection. While the KONRAD data set includes all single cells that were detected on at least two consecutive radar images and thus have a lifetime of at least 5 min, the data from TRACE3D only includes cells with a minimum lifetime of 45 min. Figure 3.4 compares the lifetime distribution of the cells included in the data sets. If only cells with a lifetime of more than 45 min are considered in the KONRAD data set, a subsample of 2280 cells remains. This number is about 20% smaller than the number of cells detected in TRACE3D. The reason for this is that in the KONRAD data set only single cells are considered and more complex cell clusters involved in cell splitting or cell merging are removed (cf. Section 3.1.2). Regarding the lifetime of the cells, it should be noted that this quantity is only based on a precipitation-producing cell that can be detected in the radar image. The actual lifetime of the convective cell from cloud formation to dissipation is usually about 30 to 45 min higher (Wilhelm, 2021).

Figure 3.5 shows a distribution of the movement direction and track length for the two data sets. In both cases, there is a clear tendency for cell tracks to be directed from the southwest to the northeast. About 50 to 60% of the tracks are found here in the southwest quadrant. However, there are also differences between the data sets. The dominance of the southwestern directions is stronger in the TRACE3D data set, whereas the KONRAD data set shows a minor local peak for directions from N to NNE. The reason for this could be single cell thunderstorms, which form in summerly high pressure conditions in a northeasterly flow and are preferably detected by KONRAD because they

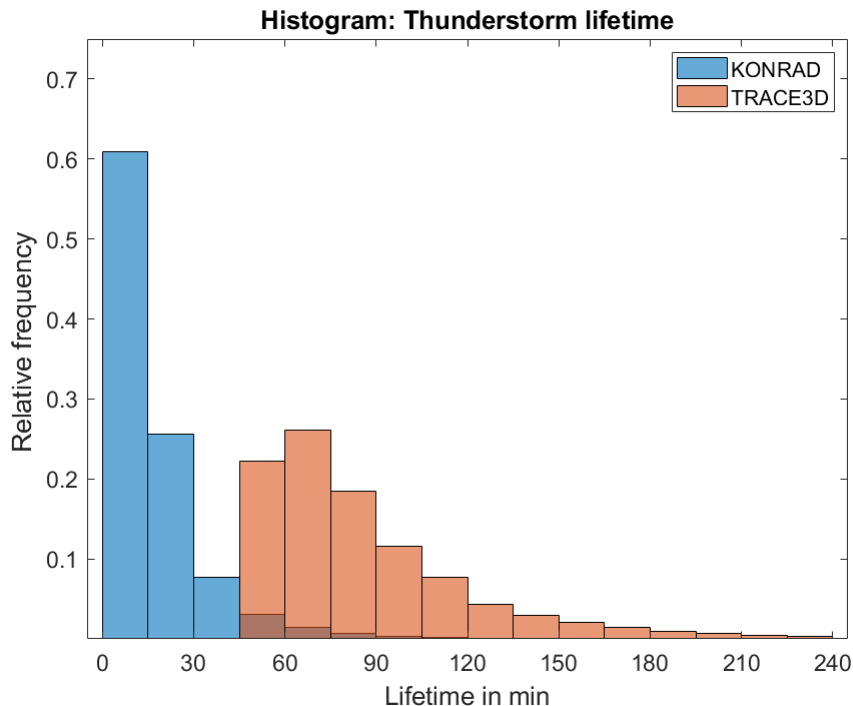


Figure 3.4: Statistical comparison of the thunderstorm lifetimes detected by KONRAD and TRACE3D. Cells from TRACE3D have a minimum lifetime of 45 min per calibration of the algorithm whereas more than 90% of cells detected by KONRAD have a lifetime below 45 min.

tend to be short-lived. The color coding by track length shows that the number density of long distance cell tracks is significantly higher in the TRACE3D data set. This is consistent with the findings from Figure 3.4, as higher lifetime (under the assumption of similar displacement velocity) also leads to increased track length. It is also apparent that long-lived cells associated with longer tracks have a tendency to move from SW to NE.

Since the influence of flow around or over the Black Forest on the formation of thunderstorms in the Swabian Jura region will be investigated in this work, the main focus is on tracks that develop under southwesterly flow.

Figure 3.6 provides an overview of the places of origin of all potential hail producing thunderstorm tracks estimated by TRACE3D for the years 2005 to 2020. The figure confirms the north-south gradient in the number of hail events found by Puskeiler (2013). A slighter pronounced east-west gradient can also be identified. Individual grid points with local maximum values are found in the Eifel, Hunsrück and Palatinate Forest, as well as in the Taunus. In Bavaria, local maxima are found in the area of the Lech Valley and from the Loisach Valley to Munich. In Baden-Württemberg, a wide area from the eastern Black Forest to the Swabian Jura can be identified, which is associated with a high number of potential hail days (from now on called PHDs). The western side of the Black Forest does not appear as a hail hotspot, and in the adjacent Upper Rhine Graben there are hardly any PHDs to be found. The Swabian Jura, on the other hand, is particularly prominent, with several neighbouring grid boxes showing values around 20 PHDs within

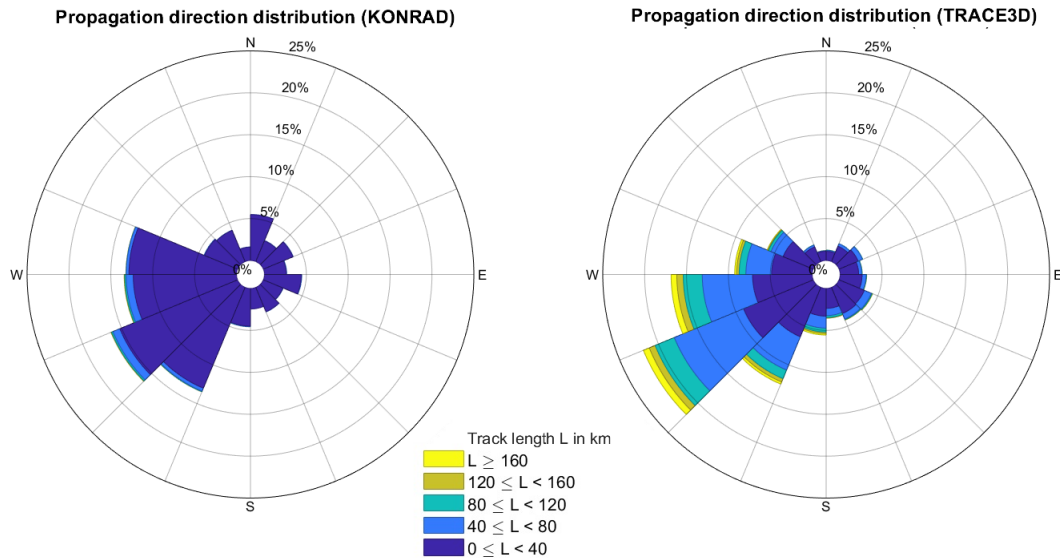


Figure 3.5: Comparison of average cell propagation direction and track length between cells detected by KONRAD (left) and cells detected by TRACE3D (right). The direction convention is analogous to wind direction, thus an entry in the southwestern quadrant indicates a cell displacement from southwest to northeast. The data is clustered by wind direction and track length (by colors).

the study period. In this context it should be noted that the place of origin mentioned here corresponds to the first detection of a cell with hail intensity registered by TRACE3D. The location of the first precipitation detection can be up to 100 km further upstream, the actual development area of the system may be even further upstream (cf. Section 4.2). The investigation of the meteorological environmental conditions during and before thunderstorm events is performed with the help of a categorization of the thunderstorm tracks into different investigation areas. One area is located directly downwind of the Black Forest ridge and encloses the Neckar Valley located there. The second study area is located above the main ridge of the Swabian Jura. Figure 3.7 graphically represents the corresponding areas. From now on, the study areas will be referred to as NV (Neckar Valley) and SJ (Swabian Jura). When referring to the unification of the two areas, the term combined investigation area is used.

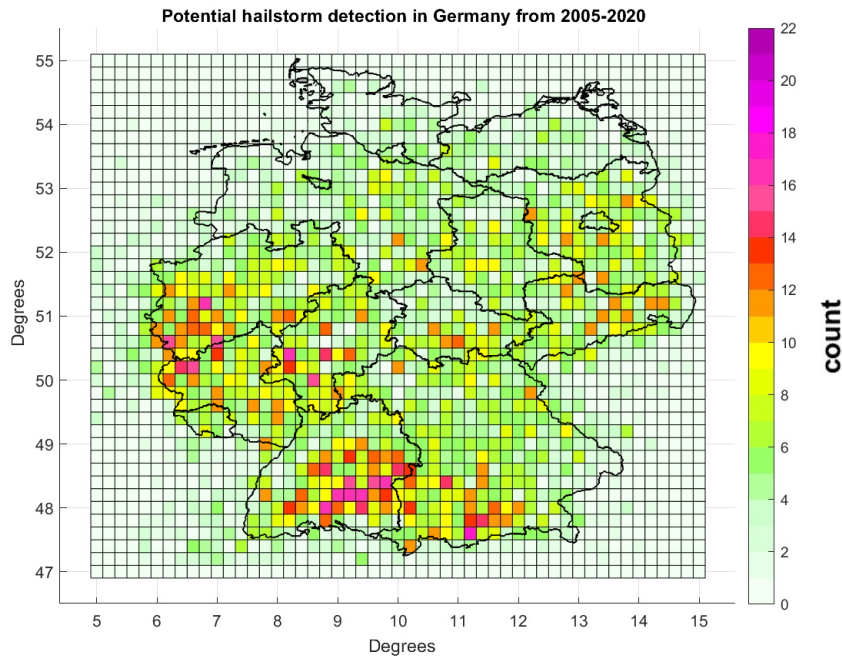


Figure 3.6: Frequency distribution of the points of first potential hail storm detection registered by TRACE3D from 2005-2020. The grid is divided into square grid boxes with an edge length of  $0.2^\circ$ . The color of the grid boxes indicates the number of detected potential hailstorm formation events within this area.

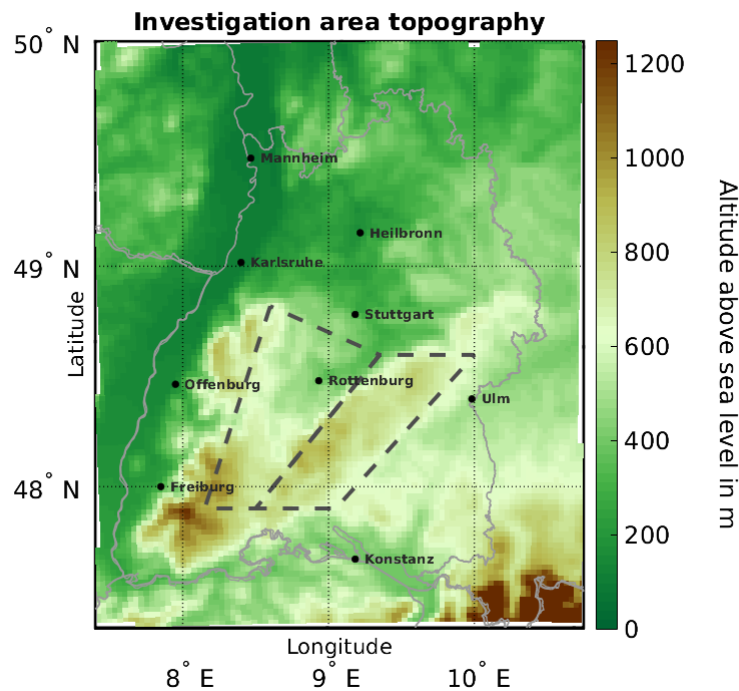


Figure 3.7: Overview of the model topography in the investigation area. Division of the study area into two sub-areas in the immediate lee of the Black Forest surrounding the Neckar Valley (NV) and the area around the main ridge of the Swabian Jura (SJ). Color shading indicates height above sea level from 0 to 1250 m in southern Black Forest as the highest mountain of Black Forest (Feldberg) is only 1223 m in the model (1493 m in reality).

### 3.3 Selection procedure for non-event days

In order to identify processes that contribute to the initiation of deep moist convection, differences in the environmental conditions between event days (potential hail days) and non-event-days (from now on called NEDs) are to be identified. In this work, PHDs are defined as days on which the TRACE3D cell tracking algorithm has detected the point of origin of a potential hail track within the combined investigation area. NEDs are defined as days that were suitable for the formation of deep moist convection with regard to the thermodynamical environmental conditions, but which did not show any thunderstorm formation in the study area. In order to exclude not only severe hailstorms but also ordinary isolated thunderstorm cells from the sample, a combined data set consisting of KONRAD data and TRACE3D data of the years 2011 to 2016 forms the basis for this exclusion criterion.

Since most cases of deep moist convection are associated with flow from the southwest, a westerly to southerly flow is used as a criterion. Additionally, the most unstable convective available potential energy (MU-CAPE, cf. Section 2.2.2) is used. This measure was chosen because it is considered as the essential (although not sufficient) criteria for the formation of (severe) thunderstorms. Since for MU-CAPE the pseudo-adiabatic ascent starts from an initial level at the lowest 300 hPa of the atmosphere at which the resulting convective available potential energy becomes maximum, this measure is less terrain-dependent compared to ,e.g., the surface-based CAPE.

In the context of a sensitivity analysis, different threshold values were studied as lower limits for the MU-CAPE as well as the low level lapse rate (LLR, lowest 3 km of the atmosphere minus the lowest model layer to avoid the surface near excess lapse rate), and their separation characteristics on the selection of all possible NEDs was investigated. A spatial average of these meteorological parameters was calculated for all days within in the investigation period at the fixed time 12 UTC and compared with the corresponding threshold value. The spatial average covered the area (cf. Figure 3.7)

$$\text{Lat}_{\min} = 47.0^{\circ}$$

$$\text{Lon}_{\min} = 7.5^{\circ}$$

$$\text{Lat}_{\max} = 50.0^{\circ}$$

$$\text{Lon}_{\max} = 10.5^{\circ}.$$

Figure 3.8 shows the number of suitable NEDs using different threshold values for the two variables considered. The number of 1098 days is equal to all days from April to September of the years 2011 to 2016. However, the two criteria that were not involved in the sensitivity study (flow direction and non-event filter) already reduced the sample size to 669 days.

The sensitivity analysis shows that the LLR only has a meaningful filter function for low MU-CAPE values of less than  $200 \text{ Jkg}^{-1}$ . This finding can be at least partly ascribed to

		Low level lapse rate in $\text{K km}^{-1}$				
		0.0	5.5	6.0	6.5	7.0
MU-CAPE in $\text{J kg}^{-1}$	0	669	592	526	379	191
	200	105	105	104	87	41
	400	56	56	55	46	25
	600	36	36	35	33	19
	800	23	23	22	22	15

Figure 3.8: Number of remaining days when filtering for a minimum required threshold-value of LLR and MU-CAPE. The filtering was applied to a data set including the 12 UTC analyses of each day from 2011 to 2016 in the summer months (April to September) that did not show any thunderstorm in the vicinity of the investigation area and with a westerly wind direction in the lower troposphere. A sample size of 669 days remains after pre-filtering by wind direction and KONRAD-events (originally 1098 days).

the relationship of the two quantities. The filtering should be performed at least with the threshold value  $\text{MU-CAPE}_{\text{threshold}} = 400 \text{ J kg}^{-1}$ , since MU-CAPE values below  $400 \text{ J kg}^{-1}$  are considered to be unsuitable for deep-moist convection. To remain a sample above 50 entries, further filtering via the LLR was not considered. Ultimately, this leads to the following three criteria that a day or a time step of the study period must fulfil in order to achieve the status of a NED:

- $180^\circ < \alpha_{12 \text{ UTC}} < 300^\circ$
- $\text{MU-CAPE}_{12 \text{ UTC}} > 400 \text{ J kg}^{-1}$
- No entry in KONRAD or TRACE3D data set within the combined investigation area on this day,

where  $\alpha_{12 \text{ UTC}}$  and  $\text{MU-CAPE}_{12 \text{ UTC}}$  are the spatially averaged values at 12 UTC for each day.  $\alpha_{12 \text{ UTC}}$  represents the low to mid-tropospheric (0 to 5000 m above surface) wind angle according to meteorological convention (North wind =  $0^\circ$ , East wind =  $90^\circ$ ).

Figure 3.9 compares the statistical distribution of the spatial means of MU-CAPE and LLR for the PHDs and the selected 56 NEDs. While the quartiles and the upper part of

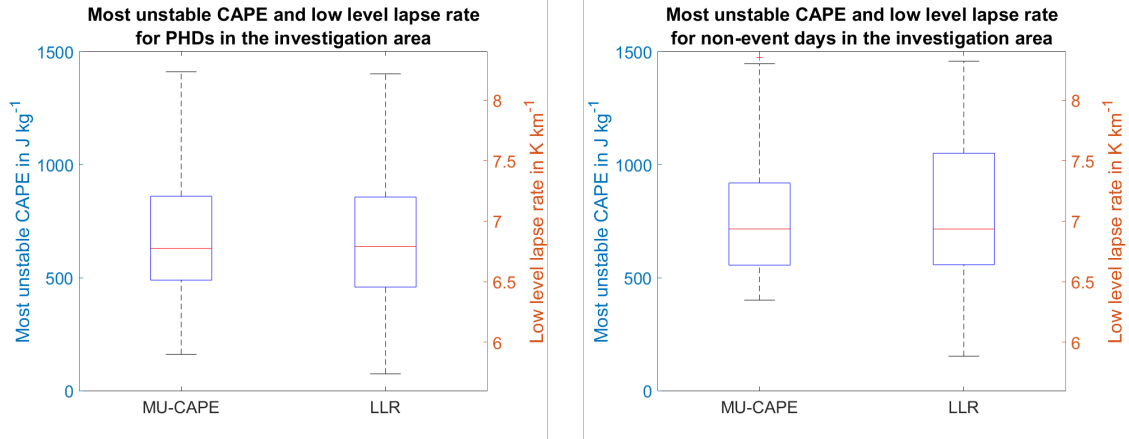


Figure 3.9: Box plots of spatially averaged MU-CAPE and LLR for PHDs and NEDs at 12 UTC. PHDs are days with potential hailstorm formation after 12 UTC within the combined investigation area, NEDs are days with suitable environmental conditions but no thunderstorm occurrence.

the distributions show good agreement between the different data sets, the sample is cut off for MU-CAPE at the lower boundary for the NED data set. This is due to the filtering method and described above.

The data set including NEDs created here should show similar thermodynamic preconditions and at least some similarities in the basic flow pattern as the event set containing the PHDs with a potential hailstorm formation after 12 UTC. Using these data, a deeper insight into the flow dynamic conditions in the investigation area should be provided, giving conclusions about potential convection-triggering processes.

### 3.4 Threshold filtering of thunderstorm effects

The advantage of the high spatial resolution of the COSMO-DE analysis is accompanied by the disadvantage that the consequences of thunderstorms resolved or assimilated in the model are apparent. In addition to the reduction of CAPE and downdraft in a cell at the end of its lifetime, the surface based effects of a gust front are clearly evident in the model data. The horizontal moisture flux convergence for example, is often up to an order of magnitude greater in the vicinity of a cold pool or gust front compared to the values prevailing in the development phase of a thunderstorm. Therefore, if conditions before and during the cumulus stage of a thunderstorm are to be investigated, it must be ensured that no disturbance effects of the fields from the cold pool are included. The horizontal moisture flux convergence is a suitable measure for recognising these situations and for removing them from the data. In the presence of heavy precipitation, the moisture flux convergence at the front of the corresponding thunderstorm cell shows a clear positive anomaly as can be seen exemplary in Figure 3.10. It shows the temporal progression of the horizontal moisture flux convergence over Baden-Württemberg during the formation and passage of the "Reutlinger Hagelunwetter" on 28 July 2013. While at time step 14 UTC no pronounced abnormal values in the horizontal moisture flux convergence are visible yet, they become more apparent in the subsequent time steps. At 16 UTC, the effects of a

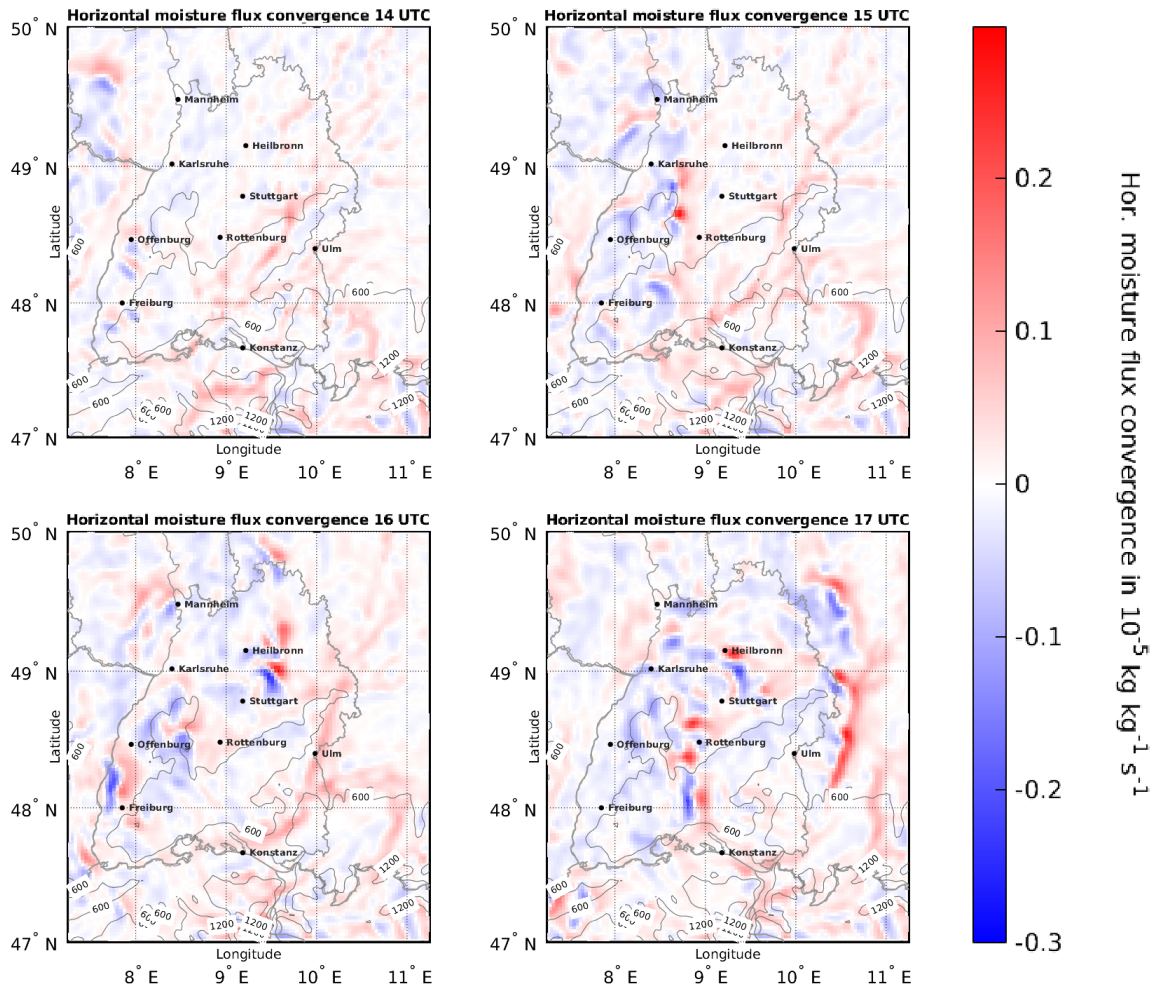


Figure 3.10: Illustration of how a thunderstorm cell affects the horizontal moisture flux convergence (colors) in COSMO-DE analysis data. Thin grey lines with labelling represent isolines of same height above sea level (in m). Bold grey lines indicate borders of federal states. The series of figures shows the development and the progression of the analyzed "Reutlinger Hagelunwetter" on 28 July 2013 from 14 to 17 UTC.

potential hail cell north of Stuttgart are visible as adjacent strongly positive and negative values, respectively. At 17 UTC, this phenomenon occurs more frequently. East and northeast of Ulm, the effects of the hail producing supercell that passed over Reutlingen can be seen.

Composites of mean meteorological fields over several time points therefore only provide meaningful results if these disturbance effects are properly filtered. Figure 3.11 shows the results of a sensitivity study for different threshold values of the moisture flux convergence and the number of grid points at which an exceedance of this threshold is tolerated. All cells detected by TRACE3D in the period from 2011 to 2016 served as input for the analysis. Thereby, model data was considered that preceded the first detection by TRACE3D by up to 3 hours. Accordingly, for a thunderstorm track first detected at 16:15 UTC, the analysis data of 14, 15 and 16 UTC were considered. Here, the considered region was placed around the investigation area in order to avoid any disturbance effects within the relevant data. Thus, all grid boxes between 47° and 50° latitude and between 7°

**Max. allowed MCONV in  $10^{-5} \text{ kg kg}^{-1} \text{ s}^{-1}$**

		<b>0.02</b>	<b>0.04</b>	<b>0.08</b>	<b>0.16</b>	<b>0.32</b>
<b>Number of grid boxes</b>	<b>1</b>	<b>0</b>	<b>1.45</b>	<b>17.6</b>	<b>69.6</b>	<b>97.6</b>
	<b>5</b>	<b>0</b>	<b>3.69</b>	<b>24.8</b>	<b>78.5</b>	<b>99.2</b>
	<b>25</b>	<b>0.13</b>	<b>8.58</b>	<b>48.6</b>	<b>95.0</b>	<b>100</b>
	<b>125</b>	<b>4.89</b>	<b>29.3</b>	<b>88.6</b>	<b>99.9</b>	<b>100</b>
	<b>625</b>	<b>27.4</b>	<b>87.2</b>	<b>100</b>	<b>100</b>	<b>100</b>

Figure 3.11: Remaining portion of analysis data in % when filtering for a maximum allowed threshold-value of horizontal moisture flux convergence and the number of grid boxes that are considered.

and  $11^\circ$  longitude are taken into account. Due to the already limited sample size of days with hail producing thunderstorms, coarse filtering of more than 50% of the data should be avoided. Isolated exceedances of the threshold at a few grid boxes can be tolerated, which is why filtering according to the threshold

$$\text{MCONV}_{\text{threshold}} = 0.08 \cdot 10^{-5} \text{ kg kg}^{-1} \text{ s}^{-1} \quad (3.2)$$

and the number of grid boxes

$$n_{\text{grid boxes}} = 125 \quad (3.3)$$

is applied. Specifically, this means that the threshold value  $\text{MCONV}_{\text{threshold}}$  is allowed to be exceeded at 124 grid boxes. In the investigations that have been performed, this phenomenon is reduced by only analysing PHDs on which a thunderstorm formed after 12 UTC and by investigating the ambient conditions for 12 UTC. Nevertheless, the filter remains active to minimize the influence of any eventual thunderstorm cells present in the analyses.

### 3.5 Spatial smoothing of horizontal moisture flux convergence fields

As shown in Figure 3.11, the horizontal moisture flux convergence can be a quite irregular field. A large part of the spatial variability is caused by gust fronts and/or heavy precipitation, but there are also some almost stationary disturbances because of small-scale topographic flow effects (cf. Section 2.6). In order to increase the readability of horizontal moisture flux fields, a moving spatial average is applied in this work. For the value of a quantity  $\xi$  at the grid point  $(x,y)$  the spatial mean is

$$\xi(x,y) = \frac{\sum_{i=n}^N \left( \sum_{j=m}^M \xi(i,j) \right)}{(2\epsilon + 1)^2} \quad (3.4)$$

with

$$\begin{aligned} n &= x - \epsilon \\ N &= x + \epsilon \\ m &= y - \epsilon \\ M &= y + \epsilon. \end{aligned}$$

$\epsilon$  defines the range of the spatial averaging. For the horizontal moisture flux convergence, spatial averaging with  $\epsilon = 2$  is used in this work, so that the value of a grid point is composed of the mean value of a  $5 \times 5$  matrix that encloses this grid point. This type of averaging causes problems at the boundary regions of the coordinate system. However, since the study areas of this work are sufficiently far away from the boundaries of the COSMO-DE grid, this effect can be neglected. If fields are considered that show a time average over several time steps, the spatial smoothing occurs strictly after the calculation of the time average.

### 3.6 Determination of flow regimes

The dynamics in terms of the wind field in the study area are investigated with regard to different flow regimes. A suitable measure for the classification of different flow regimes is the Froude number  $Fr$  (cf. Section 2.6.2). For its calculation, the (undisturbed) characteristic velocity  $U$ , the scale height of an obstacle  $H$  and the Brunt-Vaisala frequency  $N$  are required.

As a typical scale height of the Black Forest

$$H = 1000 \text{ m} \quad (3.5)$$

is used. Although the height of the Feldberg region in the COSMO-DE model is up to 1223 m, in the northern Black Forest, the model height is below 1000 m.

The characteristic horizontal velocity is determined from the COSMO-DE data. The basis for this quantity are the 12 UTC analysis associated with the sub-sample of all PHDs within the investigation area that formed after 12 UTC. Here, for each time step considered, a spatial average is derived from the wind vector components  $U$  and  $V$  for different altitude layers. The region under consideration for this aspect is located west of the Black Forest and is spanned by the coordinates (cf. Figure 3.7)

$$\text{Lat}_{\min} = 47.5^\circ$$

$$\text{Lon}_{\min} = 6.5^\circ$$

$$\text{Lat}_{\max} = 49.0^\circ$$

$$\text{Lon}_{\max} = 7.5^\circ.$$

The averaging is done component-wise over  $U$  and  $V$ . Afterwards, wind speed is obtained by

$$|\vec{v}| = \sqrt{U^2 + V^2}, \quad (3.6)$$

the calculation of the wind angle for  $U > 0$  is done by

$$\alpha_{\vec{v}} = \arctan\left(\frac{V}{U}\right), \quad (3.7)$$

and for  $U < 0$  by

$$\alpha_{\vec{v}} = 180^\circ + \arctan\left(\frac{V}{U}\right). \quad (3.8)$$

Here the angle is defined in the common mathematical sense, i.e. a westerly wind with  $U = 1$  and  $V = 0$  corresponds to  $0^\circ$ , a southerly wind with  $U = 0$  and  $V = 1$  corresponds to  $90^\circ$ . Finally, the result of the horizontal spatial averaging and a vertical averaging over height layers from 500 to 5000 m above ground level (from now on referred to as agl) is used as characteristic wind speed.

For the calculation of the (dry) Brunt-Vaisala frequency  $N$ , information about the potential temperature at different height levels is necessary. Analogously to the wind field, the potential temperature  $\theta$  is obtained from the model data and spatially averaged for each level of altitude. From the vertical change of the potential temperature, the Brunt-Vaisala frequency can then be calculated according to

$$N = \sqrt{\frac{g}{\bar{\theta}} \frac{\Delta\theta}{\Delta z}}, \quad (3.9)$$

where  $\bar{\theta}$  represents the vertically averaged potential temperature and  $\Delta\theta(\Delta z)^{-1}$  the vertical gradient of the potential temperature between the individual height layers. The Froude number is then calculated according to Equation 2.45.



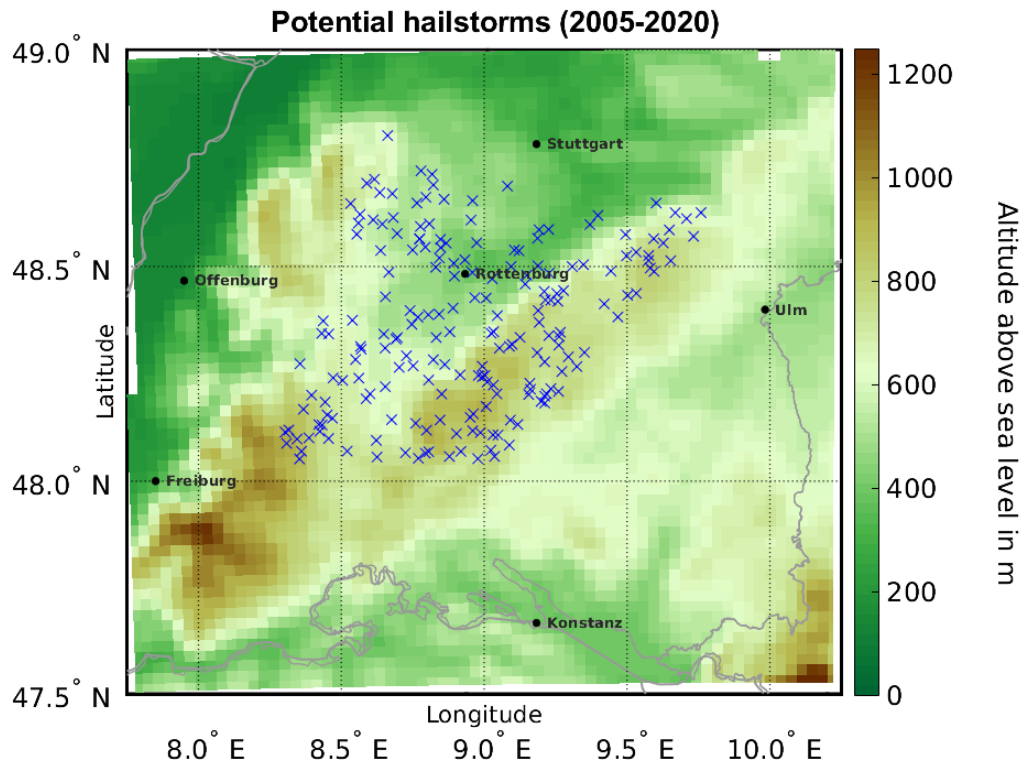


Figure 4.1: Graphical illustration of all thunderstorm cells identified and tracked by TRACE3D from 2005-2020, whose POFHD was located within the combined investigation area. Blue crosses indicate point of first detection, model orography in color.

## 4 Results

### 4.1 Properties of cell tracks within the study area

In the first step, the characteristics of cells detected in the combined investigation area were examined. With the focus on heavy rain and hailstorms, the TRACE3D event set was used. Figure 4.1 shows the location of the point at which the reflectivity of a detected cell track reaches the hail threshold value (from now on called point of first (potential) hail detection, POFHD, cf. Section 3.1.1) for all thunderstorm tracks from 2005 to 2020 where this point lies within the study area. The size of the event set is 197 in this case. It is visible that the POFHDs occur in the entire range of the combined investigation area. A clustering can be identified especially in the eastern part of the area, but also in the southwestern and northwestern border areas. Between Rottenburg and Stuttgart, an area with few POFHDs is noticeable, as well as west-southwest of Rottenburg.

The cell track characteristics (such as lifetime, track length and movement direction) of the cells shown in Figure 4.1 are compared with the properties of all thunderstorms of the

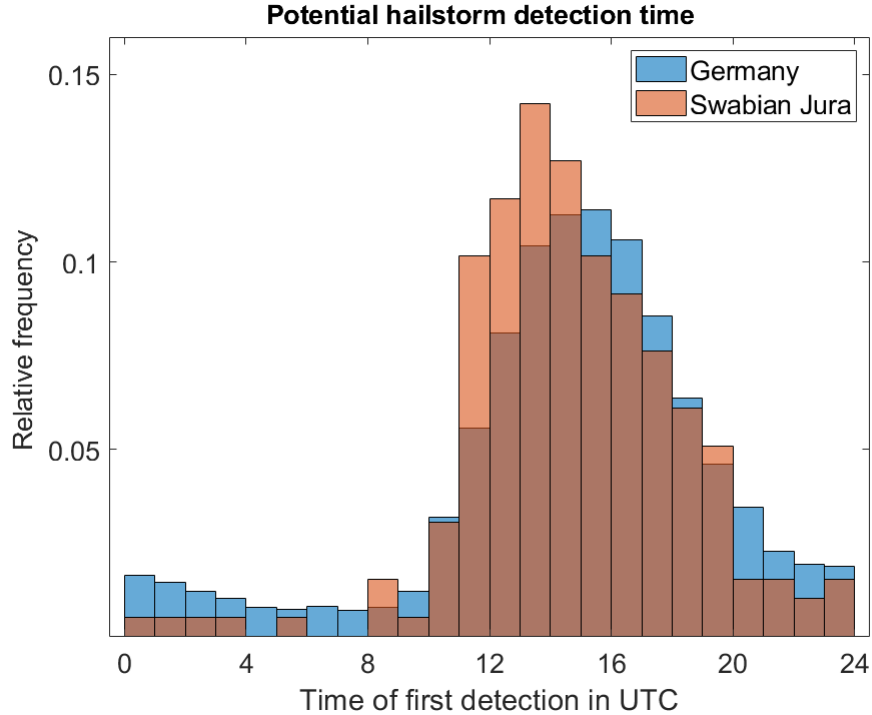


Figure 4.2: Statistical distribution of the hour of first potential hail detection of all thunderstorm cells detected by TRACE3D from 2005-2020. Blue columns indicate data for all thunderstorms within the radar network, brownish columns those for all thunderstorms, whose first point of detection was located within the combined investigation area.

whole radar network, covering more or less entire Germany. Figure 4.2 compares the two event sets with respect to the time of the first detection of potential hail. The detection time shows a clear diurnal cycle, with a minimum of thunderstorm detections in the early morning hours and a maximum around the afternoon. About 75% of all hailstorms are detected between 10 and 20 UTC. For the data set of the investigation area the maximum is found between 13 and 14 UTC, for the Germany-wide event set it is found two hours later. Also in the preceding midday hours, the thunderstorm activity in the investigation period shows a positive anomaly compared to the Germany-wide event set. One possible reason for this could be the generally suitable conditions for deep-moist convection around the Swabian Jura, which also make this region a hail hotspot in Germany (cf. Figure 3.6). In the case of weather conditions suitable for convection, this can then result in early triggering of thunderstorms, while in less suitable region for deep-moist convection a higher trigger temperature is required, which is reached only later in the course of the day. In the late evening and early morning hours, the Germany-wide event set shows a slight excess of thunderstorm development, the amplitude of the diurnal variation is smaller in general.

As can be seen in Figure 4.3 there is a clear tendency for cells to move from (south)west to (north)east in both investigation areas, NV and SJ. Only about 10% of all tracks show a movement with an easterly component. This pattern is to be expected as convection-favouring environmental conditions often occur in a transitional area between an anticyclonic ridge with its axis over eastern Central Europe and a cyclonic high altitude trough

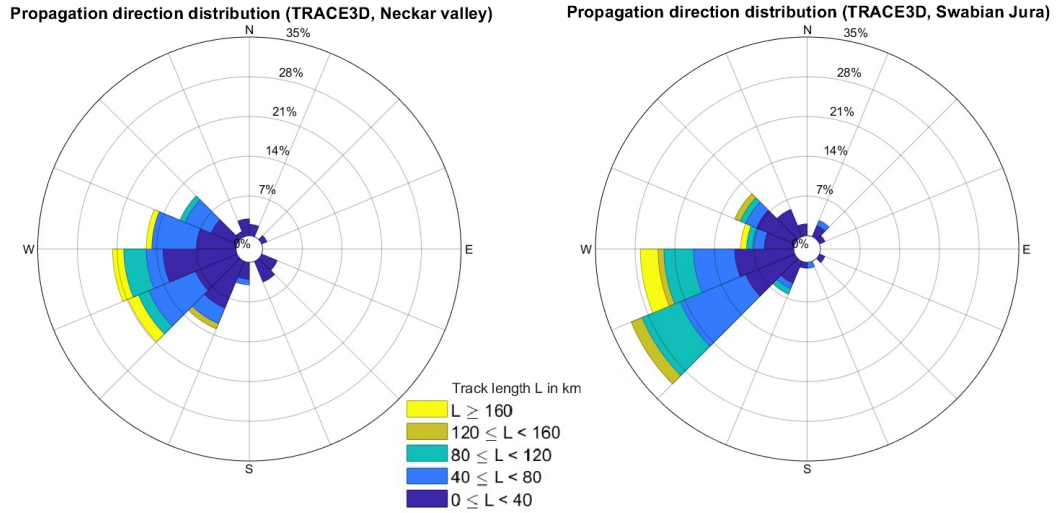


Figure 4.3: Comparison of average cell propagation direction and track length between cells that originated within the two investigation areas. The data is grouped by wind direction and trajectory length (by colors).

with the trough axis over Western Europe or the Eastern Atlantic as described in Section 2.2.1. This means that the two study areas are located on the front side of the trough and affected by large-scale lifting due to processes such as differential positive vorticity advection or warm air advection according to the omega equation (Etling, 1996). Figure 4.4 shows the mean 500 hPa geopotential in the COSMO-EU model at 12 UTC for all PHDs in the combined investigation area from 2011 to 2016.

With a pronounced southerly component of the flow, warm to hot air is often brought to Central Europe, which can be strongly moistened, especially in the lower troposphere, after moving over the open water of eastern Atlantic / western Mediterranean (Koebele, 2014). In the study area NV, a broad maximum of tracks stretching from north-western/south-western to southeastern/north-eastern direction is formed; in the study area SJ, the maximum is significantly more pronounced and lies in a westerly to south-westerly direction. The colour coding in Figure 4.3 provides information about the length of the cell tracks. The longest tracks maintain a reflectivity above the hail threshold for a distance of up to 200 km. Shorter tracks with a length of less than 80 km dominate the distribution, but longer tracks also occur to a considerable extent, especially from a westerly and southwesterly direction. The average length of a cell track in the investigation area SJ is 41.1 km, for the area NV is only 29.1 km. The average length for a cell track in the entire radar network is 35.4 km. For an overview of the propagation direction of all trajectories in the entire radar network, cf. Figure 3.5 (note the different scaling in radial direction).

Figure 4.5 presents statistics on the lifetime and compares the event sets from the two study areas NV and SJ, as well as the combined investigation area with the event set from the Germany-wide radar network. A clear difference between the two study areas with regard to the lifetime of a cell cannot be found. Considering the differences in the average length of a cell track, it is found that an average thunderstorm cell from the NV event set has a lower propagation velocity than a cell from the SJ event set and thus also propagates in an environment with less ambient winds. In comparison with the Germany-

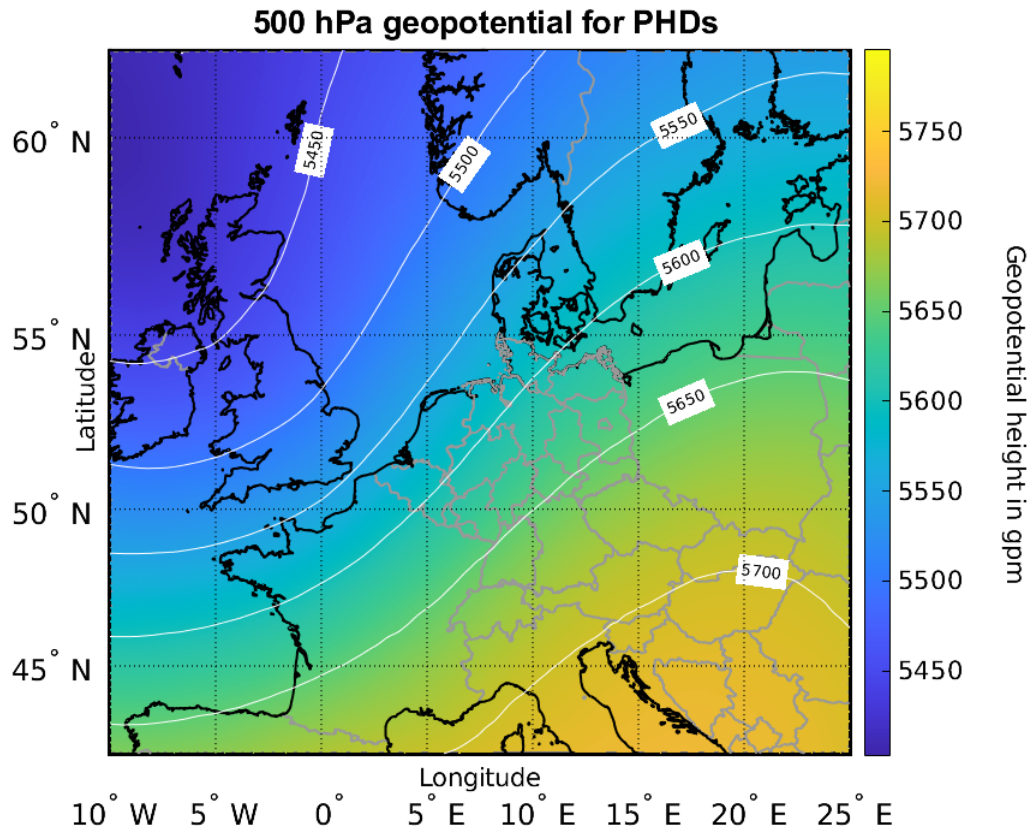


Figure 4.4: Mean 500 hPa geopotential (color shading and isohypses) for all PHDs from 2011 to 2016 with potential hailstorm occurrence within the combined investigation area.

wide event set, a smaller number of thunderstorm cells with a lifetime below 90 min is shown for cells in the combined study area. For longer-lived thunderstorm cells, a positive anomaly is present. One possible reason for this is the earlier detection of thunderstorm cells in the combined investigation area (cf. Section 4.1), which leads to energy-conducting processes such as solar insolation being stronger or persisting longer over the life cycle of a thunderstorm.

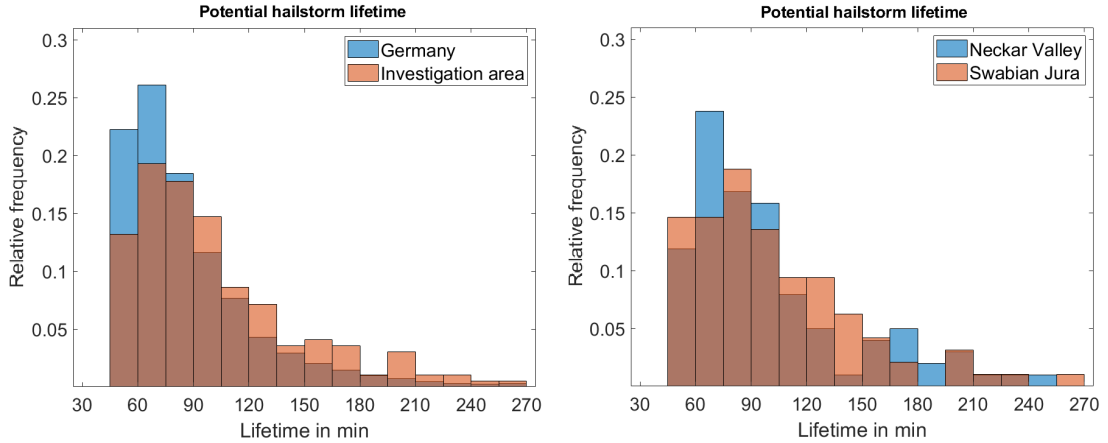


Figure 4.5: Histograms of thunderstorm lifetime. Left plot compares lifetime of all cells detected in the radar network and those that originated within the combined investigation area. Right plot compares the two sub-regions of the investigation area, NV and SJ.

## 4.2 Limitations of initial potential hailstorm detections

The TRACE3D event set used in this work is based on the threshold value  $Z_{\text{threshold},1} = 52\text{dBZ}$ , which serves as the minimum level for the selection of potential hail tracks. Although this detection works quite satisfactorily, usually some time passes between the time, where the cell is visible in a radar image and the time of the first detection by TRACE3D. Because convective cells propagate approximately with the mean wind at mid-tropospheric levels (Markowski and Richardson, 2010), the location at which TRACE3D records a cell for the first time may differ significantly from the location where convection was triggered, in particular for cases with high wind speed. For a manageable number of tracks from the TRACE3D event set, the location of the first detectable precipitation was therefore determined manually with the help of radar image archives. As can be seen in Figure 4.6, the spatial differences between detection by TRACE3D (potential hail) and manual radar-based detection (precipitation) can be significant. It is often the case that both the location detected by TRACE3D and the manually detected location lie in the combined investigation area. In individual cases, however, cells also propagate from outside into the investigation area and provide reflectivity values above the hail threshold used in TRACE3D only there.

Although the spatial distance between the first detectable radar signal and the TRACE3D hail threshold of 52 dBZ is sometimes large, the locations determined by TRACE3D nevertheless provide useful information. On the one hand, only in a few individual cases the manual detection extends far out of the defined investigation area. On the other hand, potential convection-favouring processes in the investigation area can not only cause an initial triggering of deep moist convection, but also an intensification from an ordinary precipitating cell to a potentially hail producing cell. Figure 4.7 gives an overview of the relationship of spatial and temporal distance between the different detection types. The duration between manual detection of first precipitation TRACE3D detection of potential

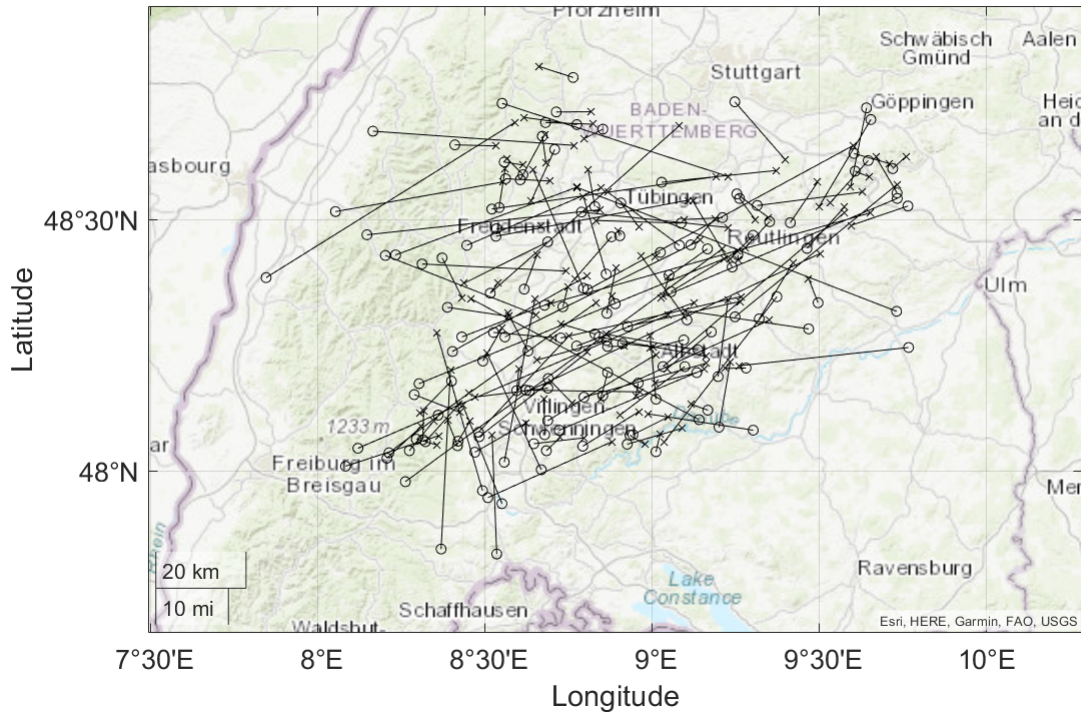


Figure 4.6: Distance vectors that result from the difference in TRACE3D detection (exceedance of hail threshold) and manual detection (first radar-visible precipitation core). Circles denote the point of manual detection, crosses the point of detection by TRACE3D.

hail ranges from 40 min to (in individual cases) over 4 h. No thunderstorm cell reached the state of a potential hail cell in less than 40 min after the detection of the first precipitation. The horizontal distance between the detection types ranges from 0 to 80 km. Due to high variability of the wind field and therefore also of the propagation speed, the correlation between time difference and spatial distance is only weak with a Pearson correlation coefficient of 0.29. This means that a large temporal difference is not necessarily connected to a large spatial difference.

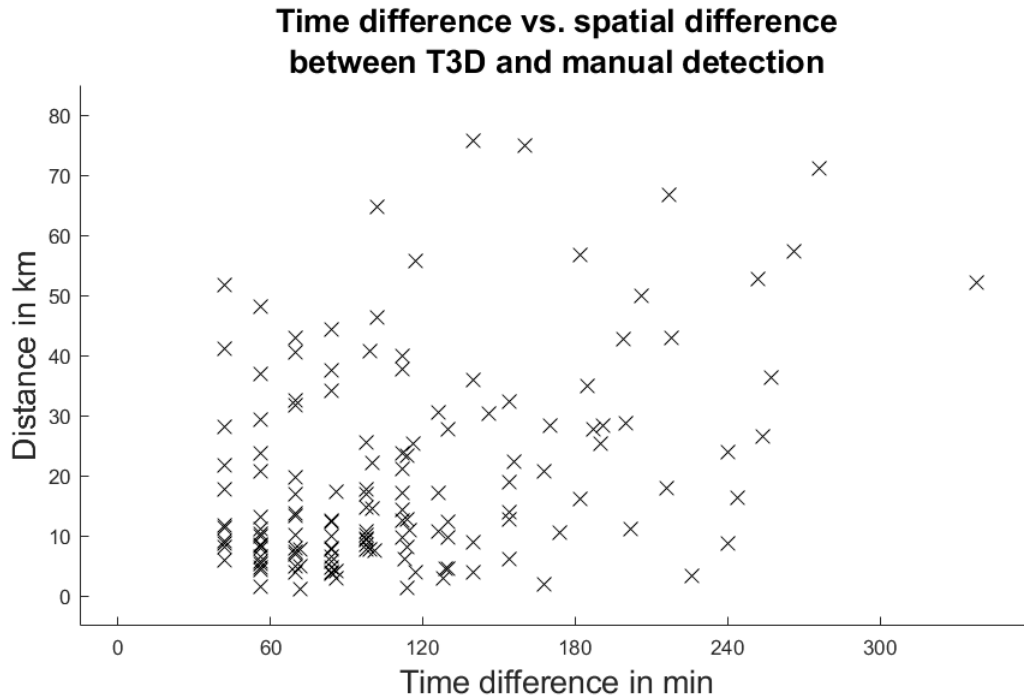


Figure 4.7: Scatter plot of spatial distance in dependence of time difference between manual and TRACE3D detection for all events in the combined investigation area from 2005 to 2020.

### 4.3 Relevance of dynamic conditions on potential hail storm occurrences in convection-favouring thermodynamical conditions

After analyzing the tracks of thunderstorm cells, the next step is to combine these events with COSMO-DE model data to investigate the environmental conditions prior and during potential hailstorms. With the use of a data set containing days whose fundamental thermodynamic conditions are suitable for the formation of deep moist convection (NED, cf. Section 3.3), differences in the flow dynamic conditions in and around the study area will be discussed. A first look is given to the parameter that has served as threshold criterion in generating the data set of NEDs, the most unstable convective available potential energy (MU-CAPE). As can be seen in Figure 4.8, the spatial distribution of MU-CAPE at 12 UTC has considerable similarities for the NEDs and PHDs. In both cases, MU-CAPE values range from 600 to 1000 Jkg<sup>-1</sup> in the area of the Black Forest and the Swabian Jura. The highest CAPE values occur downstream of the study area, in the area around and east of Ulm. A local maximum also occurs in the region between Stuttgart and Heilbronn. Northwest of the study area in the region of Rhineland-Palatinate, significantly reduced values occur, as well as on the northern edge of the Austrian Alps and over the Lake Constance. The MU-CAPE difference between PDHs and NEDs ranges from -250 to 200 Jkg<sup>-1</sup> in the area under consideration. PHDs show positive anomalies over the northern and southern Black Forest, as well as northeast of the Black Forest up to the Odenwald. This is also valid for the Austrian Northern Alps as well as the Swabian Jura,

the main study area, and further downstream from it. Between Basel and Zurich and in the Napf area (between Bern and Lucerne), the NEDs show higher MU-CAPE values than the PHDs.

Even though the LLR was not ultimately applied as a filter criterion, a brief look at it should be taken into account, as LLR can be a useful indicator for forecasting convection initiation (Umscheid, 2005). In both data sets the area from the Neckar valley to the Swabian Jura appears with unstable stratification with a vertical temperature decrease of about  $7.6 \text{ K km}^{-1}$ . The temperature gradient behaves similarly to the CAPE northwest of Baden-Württemberg with reduced values and shows a local minimum over Lake Constance. The maximum areas of MU-CAPE and LLR do not coincide precisely. The only marginal differences in LLR between PHDs and NEDs confirms the decision to reject filtering according to LLR for reasons of redundancy.

Figure 4.9 compares the horizontal wind fields of PHDs and NEDs for different heights. Here, even a close look reveals only small differences. In both cases, there are indications of a flow around the Black Forest at lower layers. However, in the lowest layer at 100 m there is also a slight acceleration of the wind over the Black Forest, presumably due to the lower interaction with the earth's surface over the exposed areas. At 1000 m agl, the flow around the Black Forest is only slightly noticeable. Instead, an area with lower wind speeds appears downstream of the Black Forest reaching as far as the Swabian Jura and also over Stuttgart. However, as this map shows time averages, low values in this figure do not necessarily indicate the absence of strong winds as a low averaged wind speed can also be produced by combining two strong winds of opposing directions. A consideration according to the median instead of the arithmetic mean, though, shows similar results. Significant differences between PHDs and NEDs are only visible in 3000 m agl. Here the PHDs show higher wind speeds overall. The flow appears undisturbed in both cases and thus is more decoupled from the earth's surface. The fact that the wind field shows hardly any differences in the lower altitude layers, but a considerable difference in wind speed is evident in the highest layer considered here (3000 m agl), indicates that a stronger vertical wind shear is present in the time averages of the PHDs.

In order to analyse the effects of the flow around the Black Forest, the horizontal moisture flux convergence is also considered. Figure 4.10 shows areas of (positive) horizontal moisture flux convergence east of the Black Forest for PHDs as well as for NEDs at the times 6 and 12 UTC. Upstream of the Black Forest, on the other hand, there is a divergent horizontal moisture flux. This is also valid for large parts of the Rhine valley (from Basel to Karlsruhe). For 6 UTC the differences between PHDs and NEDs are minor. Around 12 UTC, the horizontal moisture flux convergence shows greater amplitude. For PHDs as well as for NEDs, there is a large range of positive moisture flux convergence that stretches from the Black Forest over the Neckar valley to the Swabian Jura. The phenomenon is particularly prominent in the PHD data set. This maximum also appears in the difference plot and consistently shows increased moisture flux convergence both south and east of

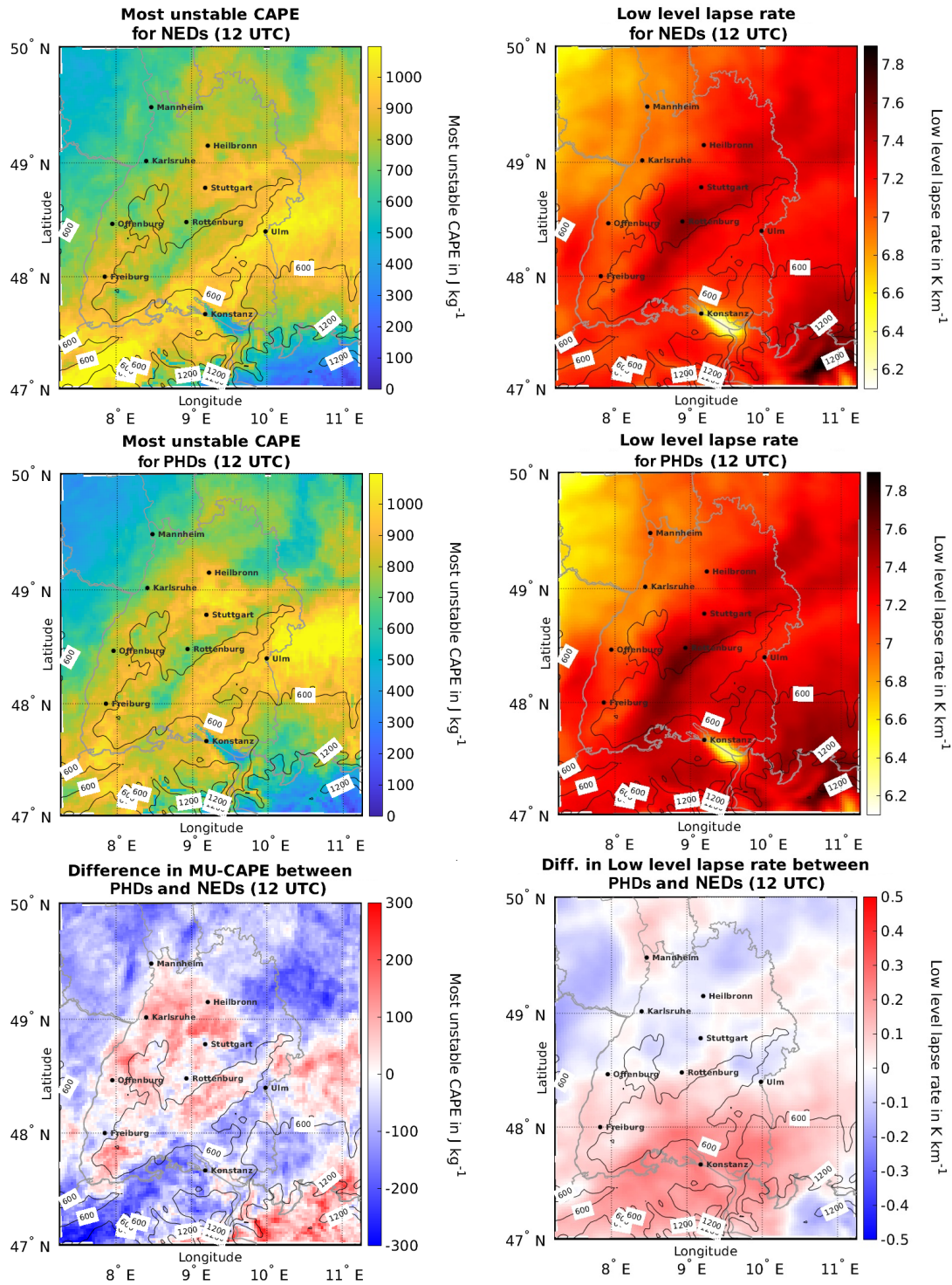


Figure 4.8: Mean MU-CAPE (left side) and LLR (right side) at 12 UTC for NEDs (top), PHDs (center) and the difference between the two (bottom). Positive values in the difference indicate a higher value in the PHD data set.

Rottenburg am Neckar in the PHD data set. The widespread area of positive horizontal moisture flux convergence may be a possible reason for the high number of thunderstorms and hailstorms downstream of the Black Forest and in the Swabian Jura region (cf. Section 3.2).

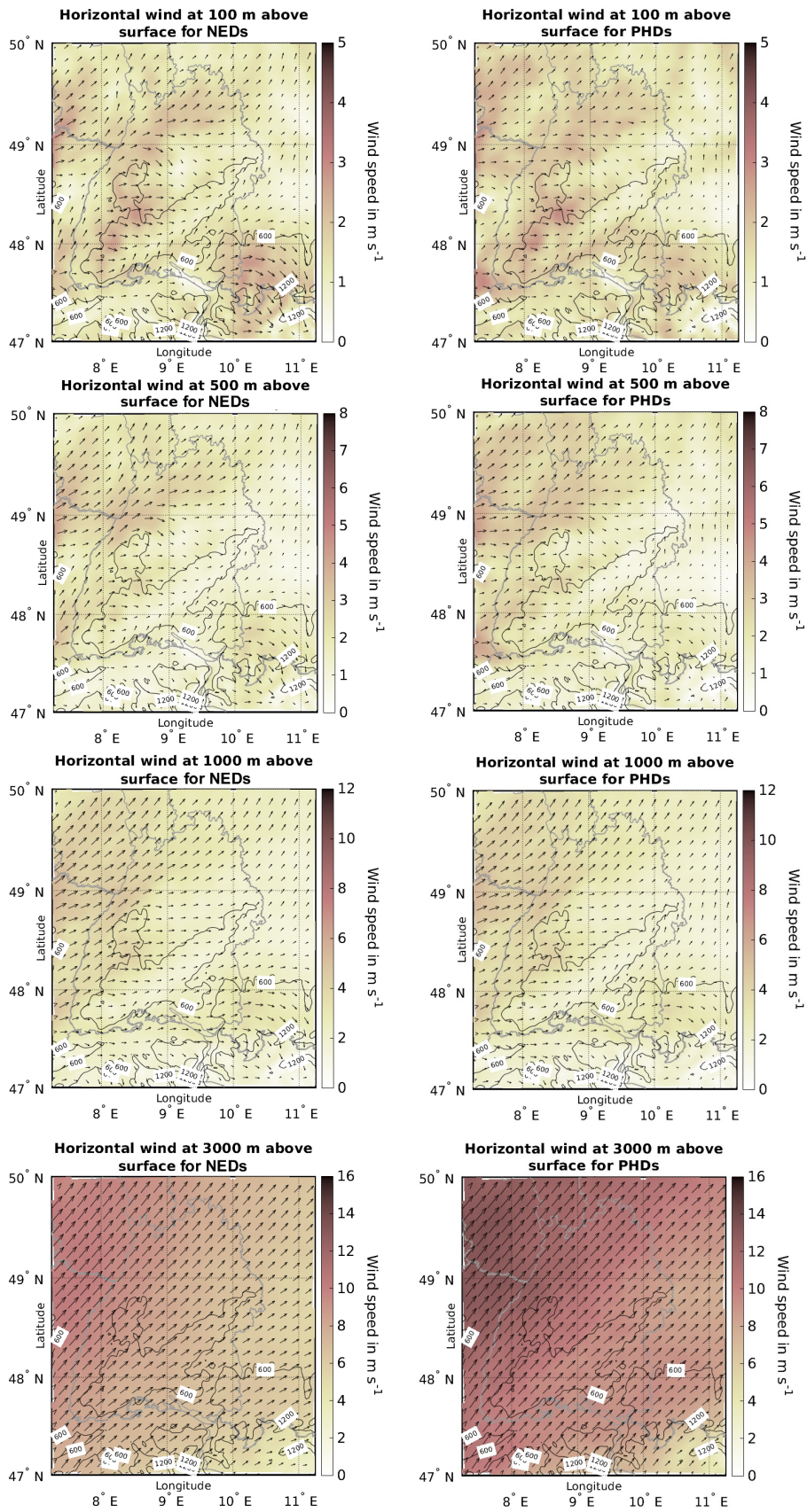


Figure 4.9: Mean horizontal wind fields (color shading and vectors) for all PHDs (right side) and NEDs (left side). Different vertical levels (in agl) are shown, note the different colorbar scaling for each level. Thin black lines with labelling represent topography.

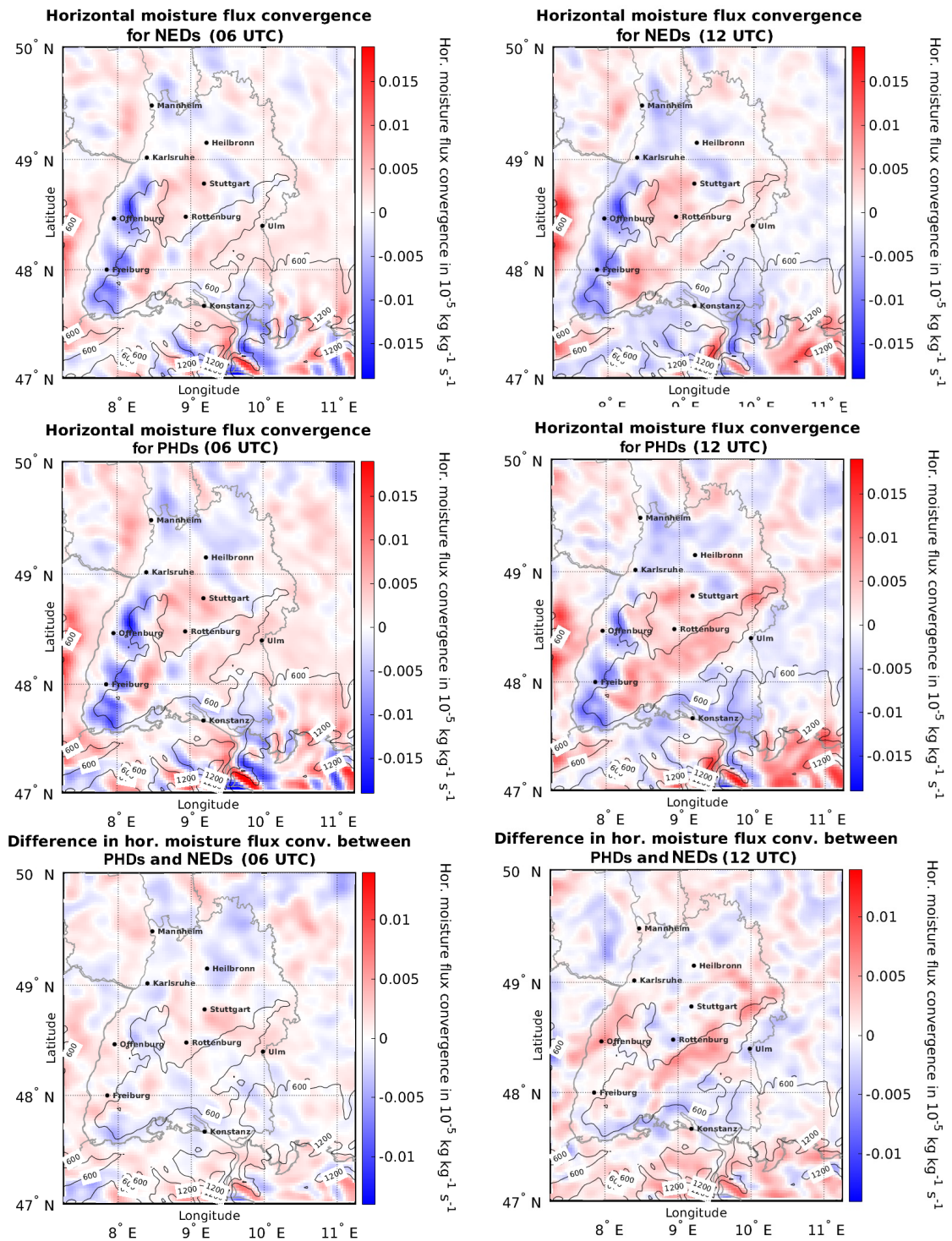


Figure 4.10: Mean horizontal moisture flux convergence at 6 (left side) and 12 UTC (right side) for NEDs (top), PHDs (center) and the difference between the two (bottom). Positive values in the difference indicate a higher value of PHDs.

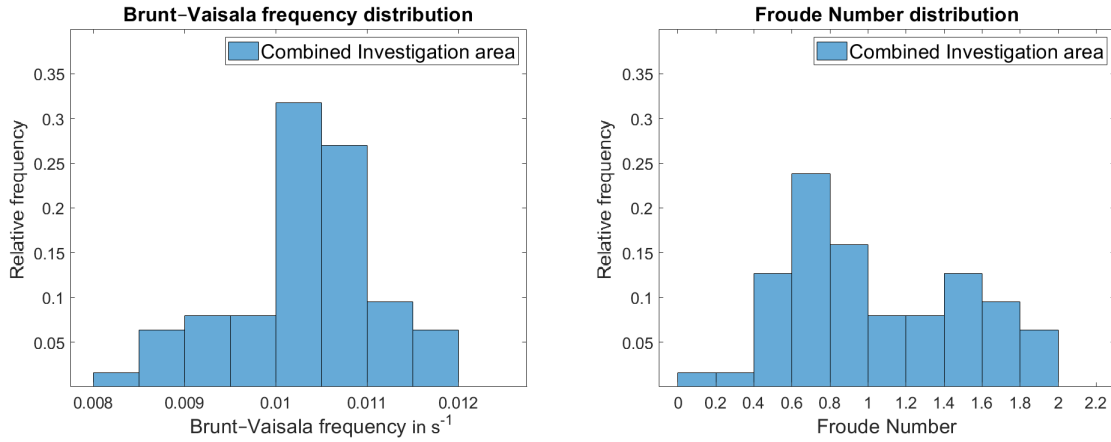


Figure 4.11: Distribution of Brunt-Vaisala Frequency (left side) and Froude number (right side) calculated from spatial means upstream of the Black Forest for all PHDs in the combined investigation area from 2011 to 2017.

## 4.4 Flow characteristics in different flow regimes and effects on potential hailstorm locality

For further investigation of the flow over / around the Black Forest the PHDs with tracks showing the of first detection within the combined investigation area were analyzed with respect to the flow regime. According to Section 3.6, the Brunt-Vaisala Frequency and the Froude number were calculated for each PHD at 12 UTC, Figure 4.11 shows the statistical distribution of the two quantities. The Brunt-Vaisala Frequency ranges from 0.008 to 0.012  $s^{-1}$  and shows a unimodal distribution with a maximum between 0.010 and 0.011  $s^{-1}$ . The Froude number ranges from 0 to 2 and shows a bimodal distribution. Two maxima appear around 0.7 and 1.5.

As can be seen in Figure 4.12 the distribution of Brunt-Vaisala frequency for the study areas NV and SJ ranges from 0.0085  $s^{-1}$  to 0.12  $s^{-1}$  for the NV event set and from 0.008  $s^{-1}$  to 0.12  $s^{-1}$  for the SJ event set. The SJ event set is mainly responsible for the contribution of the low Brunt-Vaisala frequencies. For the Froude number distribution, which ranges from almost 0 to 2, the opposite is the case. Here the NV event set is mainly responsible for the maximum in the low Froude number range. The average environmental conditions on PHDs over the Swabian Jura, on the other hand, indicate increased Froude numbers. However, since both event sets nevertheless span the entire range of the distribution, it is difficult to speak of a clear tendency. These results suggest that potential hailstorms over the Swabian Jura occur preferentially in higher Froude number regimes and thus in stable stratification and/or higher characteristic wind speeds. For potential hailstorms over the Neckar valley the opposite is the case. It should be emphasized here that the calculation of the Brunt Vaisala frequency and the Froude number is based on spatial averages of the corresponding quantities upstream of the Black Forest (cf. Section 3.6) and not on the characteristics in the study areas SJ and NV.

In order to investigate the flow dynamics in more detail, the wind field at different heights is analyzed. Figure 4.13 reveals clear differences in the horizontal wind field for PHDs

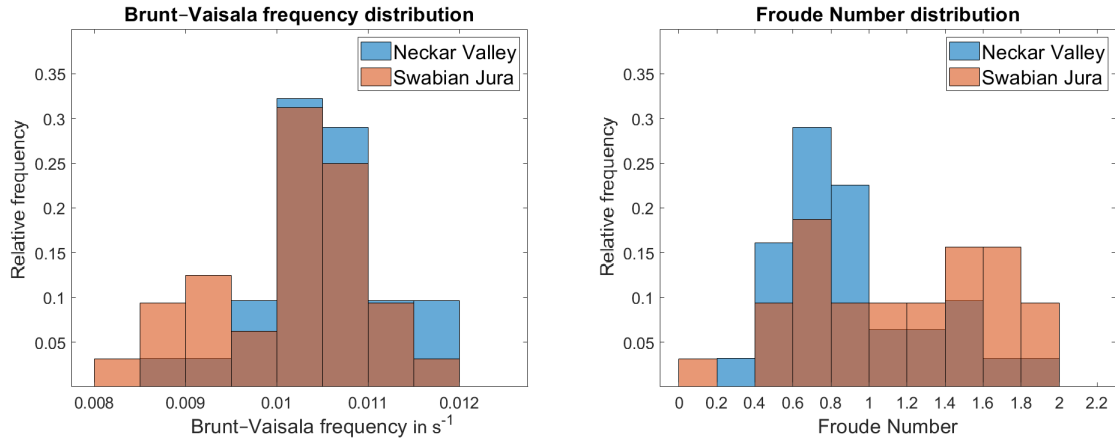


Figure 4.12: Histograms of Brunt-Vaisala frequency (left side) and Froude number (right side) between the two study areas NV and SJ from 2011 to 2017. Blue columns represent the area around the Neckar Valley (NV), brown columns the region around the Swabian Jura (SJ).

with low Froude number ( $Fr < 0.7$ ) and for PHDs with high Froude number ( $Fr > 1.4$ ). These thresholds represent the upper and lower quartile of the distribution of the Froude number shown in Figure 4.11. Therefore, both event sets for low and high Froude number consists of 18 events, respectively. A significant difference in the wind speed is visible between low and high Froude number PHDs. For the case of low Froude numbers, a significant flow around the Black Forest can be seen in the layer at 100 m agl. This occurs on the southern as well as on the northern flank of the mountains. For the case of high Froude numbers, a flow around is hardly recognisable. A clear difference can also be seen in the flow direction north of Baden-Württemberg. For the case of low Froude numbers, a local wind maximum occurs over the Allgäu, but the reason for this cannot be clarified here. A slightly visible wind maximum is apparent at the northern edge of the Black Forest. For the layers at 500 and 1000 m agl a similar picture emerges and there are clear differences in the inflow direction of the Black Forest. The greatest differences are found in 1000 m agl. While in the case of high Froude numbers an almost undisturbed flow with a homogeneous west-southwest direction is already evident here, the influence of the Black Forest on the wind field is still apparent for the case of low Froude numbers as can be seen by the wind vectors. The large-scale flow directions are showing significant differences here with northwesterly wind directions for low Froude numbers and southwesterly wind directions for high Froude numbers. Only at 3000 m agl a mostly undisturbed wind field with almost homegenic southwesterly direction can be observed even in the case of low Froude numbers. This may indicate a substantial difference in the height of the planetary boundary layer between the two data sets resulting in remarkably different flow dynamics at 1000 m agl.

For this reason, Figure 4.14 compares the boundary layer height from COSMO-DE for event sets of low and high Froude number regimes. For the cases of low Froude numbers, the height of the boundary layer extends to about 1500 m agl. Over the Black Forest, values of just under 1000 m agl are reached, indicating an absolute height of roughly

2000 m above mean sea level. In the cases of high Froude numbers, the boundary layer on the western flank of the Swabian Jura also reaches 1500 m agl, but in the spatial mean, significantly lower values are reached. Large differences are visible especially over the upper Rhine valley and north of the Black Forest. These areas coincide well with the areas where the differences in wind speed and wind direction at 1000 m altitude between the data sets are most significant.

In the last step, the horizontal moisture flux convergence fields and their differences between the two Froude number regimes will be investigated. As shown in Figure 4.15, the horizontal moisture flux convergence for both regimes reveals a large-scale area of convergence from the Black Forest to the Swabian Jura, as well as a clearly visible area of divergence on the upstream slopes of the Black Forest. In the difference plots, that represent the deviation from the low / high Froude number event set compared to the event set containing all Froude numbers, a slight positive anomaly for low Froude numbers appears in the lee of the northern Black Forest, as does a somewhat stronger maximum on the southern flank of the Black Forest. However, upstream of the Black Forest there is an extended area of negative anomaly in the horizontal moisture flux convergence. For high Froude numbers, a prominent maximum can be seen in the area of the Swabian Jura ridge, which is also clearly visible in the anomaly map. Areas of strong moisture flux convergence can also be seen in the Rhine valley and in the area of the northern Vosges.

In the upper part of Figure 4.15 black crosses are visible, which represent the POFHD of all potential hail tracks, whose environmental conditions are included in the time mean of the corresponding map. For low Froude numbers, nine of these crosses are located in the investigation area NV and another nine in the study area SJ. In the case of high Froude numbers, only five crosses fall in the western study area NV, whereas 13 entries are located in the eastern study area SJ. This is at least partially consistent with the findings from Figure 4.12 and suggests that in a high Froude number environment, potential hailstorms are more likely to occur over the Swabian Jura than over the Neckar valley, and therefore not in the immediate lee of the Black Forest but further downstream with a distance of more than approx. 50 km to the Black Forest. However, whether the Froude number can act as a predictor in this respect cannot be elaborated in detail in the context of this work. Furthermore, the interpretation of the POFHD is limited here by the fact that the additional separation by Froude number has reduced the sample size to 18 events for each of the investigation areas NV and SJ.

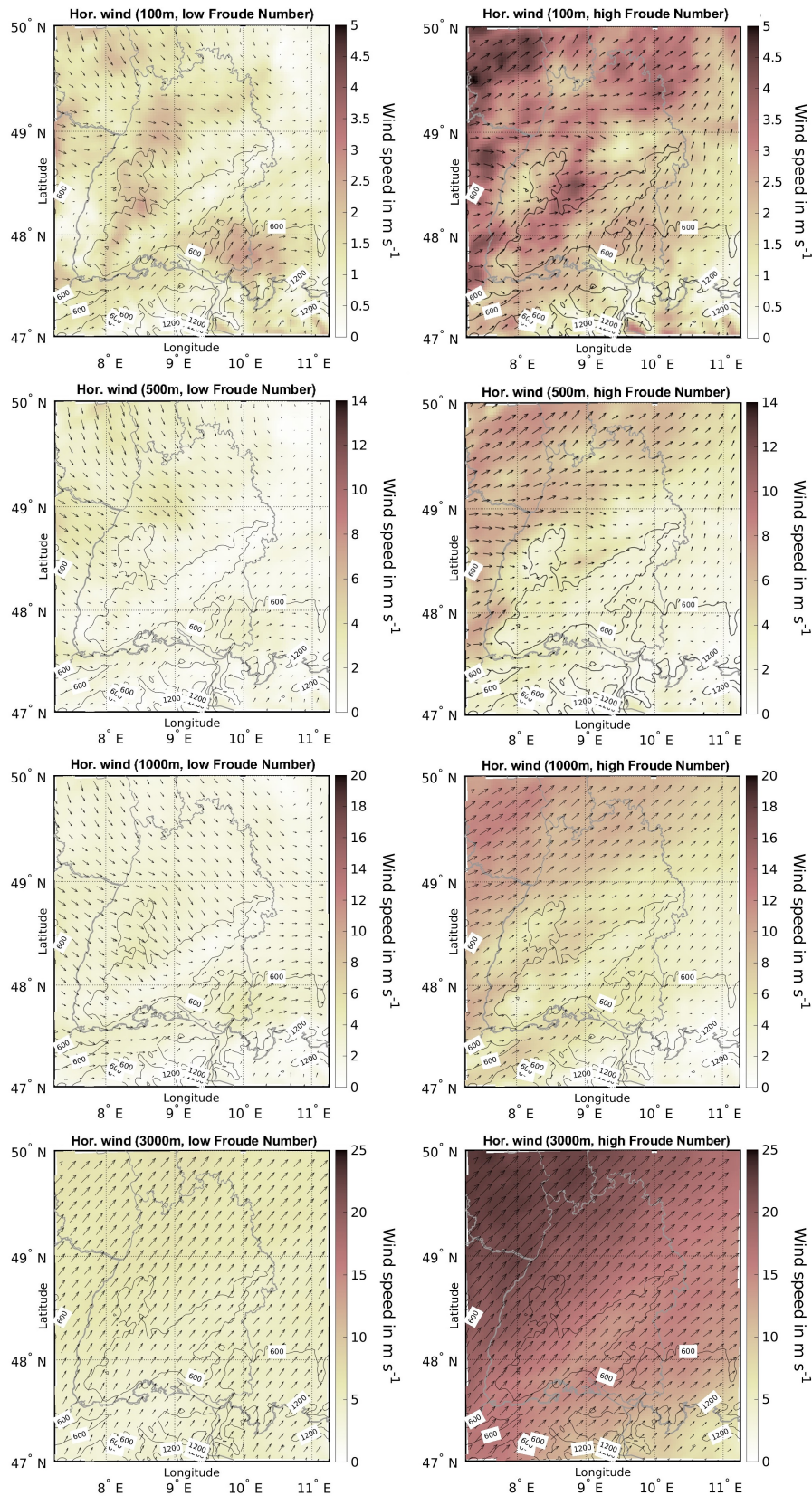


Figure 4.13: Mean horizontal wind fields at 12 UTC (color shading and vectors) for PHDs with thunderstorm formation within the combined investigation area from 2011 to 2017. Left side shows low Froude number situations with  $Fr < 0.7$ , right side shows high Froude number situations with  $Fr > 1.4$ . Sample size is 18 events for each Froude number regime. Different vertical levels (agl) are shown, note the different colorbar scaling for each level. Thin black lines with labelling represent topography, grey lines represent state borders.

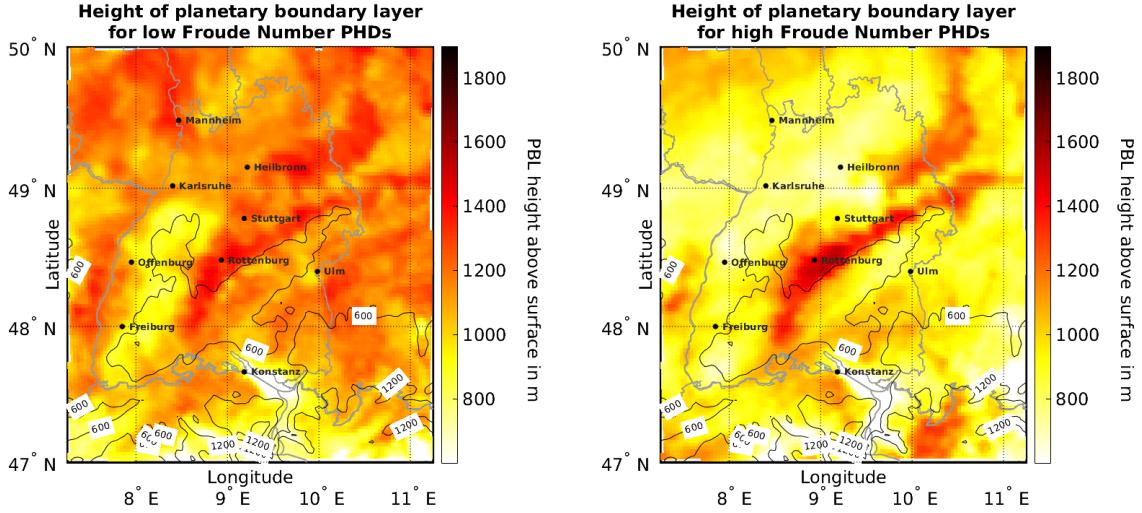


Figure 4.14: Mean planetary boundary layer height above surface (color shading) at 12 UTC. Left side shows time average over PHDs with low Froude number, right side for PHDs with high Froude number. Black solid lines indicate surface height above sea level.

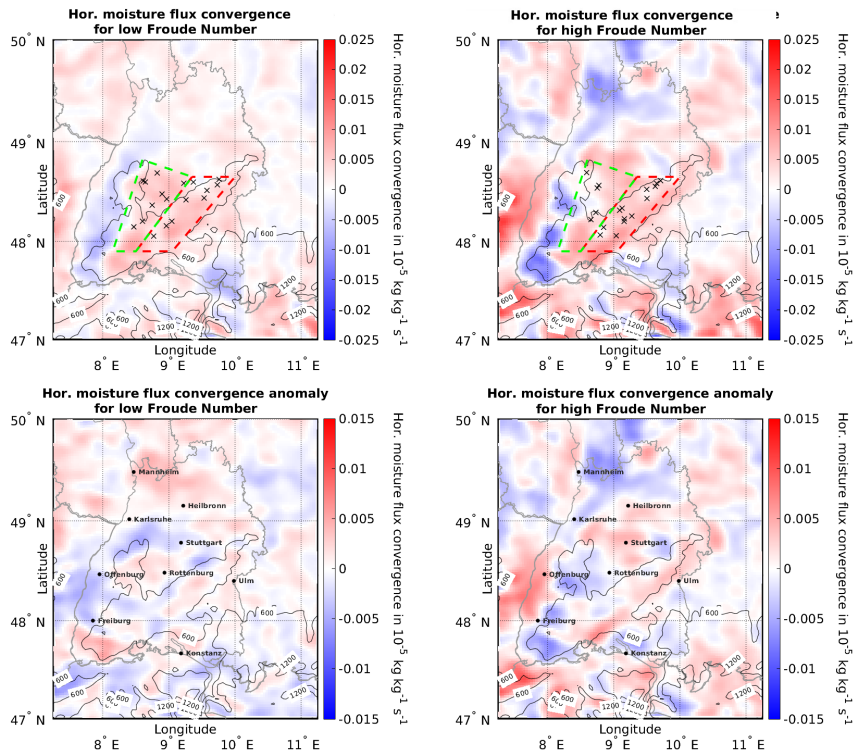


Figure 4.15: Mean horizontal moisture flux convergence (color shading) at 12 UTC for all time steps with hailstorm formation within the combined investigation area from 2011 to 2016. Left side shows low Froude number situations with  $Fr < 0.7$ , right side shows high Froude number situations with  $Fr > 1.4$ . In the upper part (absolute values of MCONV) black crosses indicate the locations of hailstorm formation that occurred during those time steps. Green and red box indicate the study areas. Lower part shows the anomaly of low or high Froude number situations compared to the average situation without any Froude number filtering. MCONV fields are smoothed after Section 3.5.

## 5 Final remarks and discussion

Thunderstorms and their associated phenomena such as severe gusts, heavy rainfall, hail, or tornadoes are responsible for damages of several hundred million euros per year in Germany. 80 % of this damage is due to hailstorms, 70 % of which occur in Baden Württemberg alone (SwissRe-Institute, 2021). Especially downstream of the low mountain ranges, a clear clustering of hail events was found by Kunz and Puskeiler (2010) and Schmidberger (2018). The aim of this work was to investigate the environmental conditions during the development phase of severe thunderstorms downstream of the Black Forest with the help of data sets obtained from the cell tracking algorithms KONRAD and TRACE3D, as well as the use of COSMO-DE analysis data, and to explore connections between the thermodynamic and flow-dynamic properties as well as their influence on the formation of thunderstorms. The focus was on an investigation area that extended from the western slopes of the Black Forest to the Swabian Jura and included the Neckar valley. The main study period spanned over the years from 2011 to 2016. Based on the data from the cell tracking algorithms, the study area of this work could be identified as a Germany-wide hail hotspot. Statistical differences between potential hailstorms from the investigation area and potential hailstorms from the Germany-wide event set were examined. The results indicate a longer lifetime for potential hailstorms within the investigation area compared to those from the Germany-wide event set. Additionally, for severe thunderstorms whose point of first detection was within the investigation area, the maximum number of detected thunderstorms by TRACE3D was slightly earlier in the course of the day, between 13 and 14 UTC, while in the Germany-wide event set it is between 15 and 16 UTC. Regarding the propagation direction, there is a strong tendency for thunderstorms over the Swabian Jura to have tracks directed from WSW to ENE, potentially affected by the orographic features.

By calculating spatial averages of the potential temperature for different height layers and vertically averaged wind speed from the COSMO-DE analysis data, the TRACE3D data set was divided into different flow regimes according to the Froude number. The classification was based on the threshold values  $Fr < 0.7$  and  $Fr > 1.4$ . For potential hail days (PHDs) with low Froude numbers, the model simulations showed a clear flow around the Black Forest on both the northern and southern edges. Signs of the flow around the Black Forest are visible up to 1000 m above the ground. This flow around results in flow divergence over the Rhine valley and a large region of flow convergence in the investigation area. These areas of convergence, moreover, exhibit comparably strong positive values in the horizontal moisture flux convergence. For PHDs with a high Froude number, weakly pronounced flow modification effects of the Black Forest were shown at significantly higher wind speeds in the layers near the ground. At 1000 m agl, this data set shows an almost

completely decoupled flow from the Earth's surface, indicating different vertical extents of the planetary boundary layer (PBL) between the data sets of the two flow regimes. For PHDs with low Froude number, the height of the PBL was found to be about 1400 m above ground on spatial average, for PHDs with high Froude number, values around 1000 m were found. Thunderstorm days on which potential hailstorms were detected over the Neckar valley showed a tendency towards low Froude numbers. Analogously, potential hailstorms whose point of first detection was over the Swabian Jura showed a tendency towards higher Froude numbers. However, due to the small sample size of the data sets (18 entries per sub-study area), these indications need further quantitative confirmation. In addition, for the case of a flow over of the Black Forest, the role of gravity waves in the development or intensification of deep-moist convection should be investigated.

In addition, also non-event days were considered in the analyses, i.e. a data set with days that showed suitable thermodynamic conditions but where no thunderstorm were detected by KONRAD or TRACE3D. This procedure was performed by using threshold values for spatial averages of the vertically averaged flow direction and the most unstable convective available potential energy (MU-CAPE). Only minor differences were found between the PHD data set and the non-event data set in the low-level wind field. However, in 3000 m agl the PHDs show higher wind speeds overall indicating a stronger vertical wind shear. The non-event days also show a flow around the Black Forest with areas of divergence over the Rhine valley and the western slopes of the mountains as well as a pronounced area of convergence downstream of the Black Forest, which extends to the Swabian Jura. In the area of the Swabian Jura ridge, however, the moisture flux convergence at 12 UTC was clearly more pronounced in the PHD data set than for the non-events.

For a more appropriate selection of non-event days, further sensitivity studies would be appropriate, including other parameters that are involved in the formation of potential hailstorms, such as vertical wind shear. However, this makes it more difficult to obtain a data set with sufficient sample size. In addition, elaborating differences in the flow dynamics is more complicated, when a certain dynamic is already predefined.

The PHDs used in this work includes all thunderstorm cells whose point of first detection (= first time step exceeding the hail detection threshold of 52 dBZ), as determined by TRACE3D, is within the study area. However, as the investigations have shown, there can be up to 80 km distance between the point of first detection determined by TRACE3D in the setup of Schmidberger (2018) and the first precipitation visible in the radar image. The actual point of origin of a thunderstorm can therefore be up to imately 100 km from the location used in this work. Nevertheless, the event set used here is justified, since the convection-favoring processes investigated can also contribute to strengthening an already existing thunderstorm into a hailstorm. This behavior was observed at least in individual cases. Nevertheless, the data set could be enlarged and improved by estimating the exact origin of the corresponding thunderstorms. In addition to considering mean fields of wind and horizontal moisture flux convergence, the discussion of an individual case

---

study, such as the "Reutlinger Hagelunwetter" (2013), might improve the understanding of the interaction between flow and moisture flux convergence areas and the initiation or intensification of deep-moist convection.

A comparison of the flow dynamics simulated by COSMO-DE in the study area with real observations could not be performed within the scope of this work. The existence of the convergence regions downstream of the Black Forest simulated by the model should be verified in further work with observational data. In this context, the measurement campaign Swabian MOSES 2021 is particularly suitable, in which the ambient conditions before and during local-scale convective thunderstorms associated with heavy rain and hail were investigated. Even if the COSMO-DE model provides a good basis for the simulation of wind fields in complex terrain due to its high spatial resolution, there may be external factors in reality not present in the model. In the context of warm air advection from southern regions, the input of Saharan dust should be mentioned in particular, which might have a large impact on the formation of deep moist convection by weakening the solar radiation. Saharan dust or other aerosol particles can also have a favourable influence on cloud and precipitation formation through their effect as cloud condensation nuclei (CCN) or ice nucleating particles (INP), whose impacts are not simulated within the model.



# Bibliography

- Adler, R. F. and D. D. Fenn, 1979: Thunderstorm vertical velocities estimated from satellite data. *Journal of Atmospheric Sciences*, **36**, 1747 – 1754.
- Banacos, P. C. and D. M. Schultz, 2005: The use of moisture flux convergence in forecasting convective initiation: Historical and operational perspectives. *Weather and Forecasting*, **20**, 351 – 366.
- Bartels, H. et al., 2005: Projekt RADVOR-OP: Radargestützte, zeitnahe Niederschlagsvorhersage für den operationellen Einsatz (Niederschlag-Nowcasting-System). Final Report, Deutscher Wetterdienst, Offenbach, Germany.
- Bergeron, T., 1928: Über die dreidimensional verknüpfende Wetteranalyse. *Geofysiske Publikationer*, **5**, 1 – 111.
- Bolton, D., 1980: The computation of equivalent potential temperature. *Monthly Weather Review*, **108**, 1046 – 1053.
- Bothwell, P., 1988: Forecasting convection with the AFOSData analysis programs (ADAP-version 2.0). *NOAA Technical Memorandum NWS SR-122*, NOAAiNWS Southel'll Regional Headquarters, Washington, D.C., USA.
- Brombach, J., 2012: Modifikation der Strömung über Mittelgebirgen und die Auswirkungen auf das Auftreten hochreichender Konvektion. Master's thesis, Institute of Meteorology and Climate Research (IMK), Karlsruhe Institute of Technology (KIT), Karlsruhe, Germany.
- Bunkers, M. et al., 2002: A preliminary investigation of supercell longevity. *The 21st Conf. on Severe Local Storms and 19th Conf. on Weather Analysis and Forecasting/15th Conf. on Numerical Weather Prediction*, San Antonio, USA.
- Byers, H. R. and R. R. Braham, 1948: Thunderstorm structure and circulation. *Journal of Meteorology*, **5**, 71–86.
- COSMO, 1998: Consortium for Small-scale Modeling. URL: <http://cosmo-model.org>, accessed on: 17.02.2022.
- Damian, T., 2011: Blitzdichte im Zusammenhang mit Hagelereignissen in Deutschland und Baden-Württemberg. Master's thesis, Institute of Meteorology and Climate Research (IMK), Karlsruhe Institute of Technology (KIT), Karlsruhe, Germany.
- DiGangi, E. A. et al., 2016: An overview of the 29 May 2012 Kingfisher supercell during DC3. *Journal of Geophysical Research: Atmospheres*, **121**, 14,316–14,343.

- Dixon, M. and G. Wiener, 1993: TITAN: Thunderstorm Identification, Tracking, Analysis, and Nowcasting: A Radar-based methodology. *Journal of Atmospheric and Oceanic Technology*, **10**, 785 – 797.
- Doms, B. M., G., 2018: A description of the nonhydrostatic regional cosmo-model part i: Dynamics and numerics. consortium for small-scale modelling. URL: [http://www.cosmo-model.org/content/model/documentation/core/cosmo\\_dynamics\\_5.05.pdf](http://www.cosmo-model.org/content/model/documentation/core/cosmo_dynamics_5.05.pdf), accessed on: 18 Feb 2022.
- Doswell, C., 1987: The distinction between large-scale and mesoscale contribution to severe convection: A case study example. *Weather and Forecasting*, **2**, 3 – 16.
- Doswell, C. A., 1982: The operational meteorology of convective weather. volume 1. operational mesoanalysis. *Operational Mesoanalysis*, **1**, Air Weather Service, Scott Air Force Base, Belleville, USA.
- Doswell, C. A., 1985: The operational meteorology of convective weather. *Storm scale analysis*, **2**, Air Weather Service, Scott Air Force Base, Belleville, USA.
- Dotzek, N., 2001: Tornadoes in Germany. *Atmospheric Research*, **56**, 233 –251.
- Dotzek, N., P. Groenemeijer, B. Feuerstein, and A. Holzer, 2009: Overview of ESSL’s severe convective storms research using the European Severe Weather Database ESWD. *Atmospheric Research*, **93**, 575–586.
- Doviak, R. J. et al., 2006: *Doppler radar and weather observations*. Dover Publications, Mineola, USA, 562 pages.
- DWD, 2018: Radarverbund des Deutschen Wetterdienstes, Deutscher Wetterdienst, Offenbach, Germany. URL: [https://www.dwd.de/DE/derdwd/messnetz/atmosphaerenbeobachtung/\\_functions/Teasergroup/radarverbund\\_teaser5.html](https://www.dwd.de/DE/derdwd/messnetz/atmosphaerenbeobachtung/_functions/Teasergroup/radarverbund_teaser5.html), accessed on: 29 Sep 2021.
- DWD, 2021a: Konvektive Entwicklung in RadarproduktenDeutscher Wetterdienst, Offenbach, Germany. URL: [https://www.dwd.de/DE/forschung/wettersvorhersage/met\\_fachverfahren/nowcasting/konrad\\_node.html](https://www.dwd.de/DE/forschung/wettersvorhersage/met_fachverfahren/nowcasting/konrad_node.html), accessed on: 28 Sep 2021.
- DWD, 2021b: Regionalmodell COSMO-DEDeutscher Wetterdienst, Offenbach, Germany. URL: [https://www.dwd.de/DE/forschung/wettersvorhersage/num\\_modellierung/01\\_num\\_vorhersagemodelle/regionalmodell\\_cosmo\\_de.html](https://www.dwd.de/DE/forschung/wettersvorhersage/num_modellierung/01_num_vorhersagemodelle/regionalmodell_cosmo_de.html), accessed on: 28 Sep 2021.
- DWD, 2022: Qualitätssicherung von WetterradardatenDeutscher Wetterdienst, Offenbach, Germany. URL: [https://www.dwd.de/DE/forschung/wettersvorhersage/met\\_fachverfahren/wetterradarverfahren/qualitaetssicherung\\_wetterradardaten\\_node.html](https://www.dwd.de/DE/forschung/wettersvorhersage/met_fachverfahren/wetterradarverfahren/qualitaetssicherung_wetterradardaten_node.html), accessed on: 19 Jan 2022.
- Etling, D., 1996: *Theoretische Meteorologie*. Vieweg+Teubner Verlag, Wiesbaden, Germany, 364 pages.

- Frontke, J., 2021: Von der Radarreflektivität zur Regenrate, Deutscher Wetterdienst, Offenbach, Germany. URL: [https://www.dwd.de/DE/wetter/thema\\_des\\_tages/2021/9/24.html](https://www.dwd.de/DE/wetter/thema_des_tages/2021/9/24.html), accessed on: 19 Jan 2022.
- Graf, M. A., M. Sprenger, and R. W. Moore, 2011: Central european tornado environments as viewed from a potential vorticity and lagrangian perspective. *Atmospheric Research*, **101**, 31–45.
- Hagen, M., J. van Baelen, and E. Richard, 2011: Influence of the wind profile on the initiation of convection in mountainous terrain. *Quarterly Journal of the Royal Meteorological Society*, **137**, 224–235.
- Handwerker, J., 2002: Cell tracking with TRACE3D - a new algorithm. *Atmospheric Research*, **61**, 15–34.
- Helmert, K. et al., 2014: DWDs new radar network and post-processing algorithm chain. *The eighth european conference on radar in meteorology and hydrology*, (Munich, Germany).
- Houze, R. A., 1994: Cloud dynamics. *Quarterly Journal of the Royal Meteorological Society*, **120**, 1427–1428.
- Johnson, T., J. et al., 1998: The storm cell identification and tracking algorithm: An enhanced wsr-88d algorithm. *Weather and Forecasting*, **13**, 263 – 276.
- Juckes, M. and R. K. Smith, 2000: Convective destabilization by upper-level troughs. *Quarterly Journal of the Royal Meteorological Society*, **126**, 111–123.
- Kaschuba, M., 2013: Hailstone side view. Picture published on 09 Aug 2013.
- Kessler, E., 1981: *Thunderstorms: Thunderstorm morphology and dynamics*, Washington, D.C., USA, 432 pages, Vol. 2. US Department of Commerce, National Oceanic and Atmospheric Administration.
- Koebele, D., 2014: Analyse von Konvergenzbereichen bei Hagelereignissen stromab von Mittelgebirgen anhand von COSMO-Modellsimulationen. Master’s thesis, Institute of Meteorology and Climate Research (IMK), Karlsruhe Institute of Technology (KIT), Karlsruhe, Germany.
- Köhler, H., 1921: Zur Kondensation des Wasserdampfes in der Atmosphäre. *Geofysisk. Publicationer*, **2**, 3–15.
- Kugel, P., 2012: Anwendung verschiedener Verfahren zur Detektion von Hagel aus dreidimensionalen C-Band Radardaten. Master’s thesis, Institute of Meteorology and Climate Research (IMK), Karlsruhe Institute of Technology (KIT), Karlsruhe, Germany.
- Kunz, M., 2003: Simulation von Starkniederschlägen mit langer Andauer über Mittelgebirgen. Ph.D. thesis, Institute of Meteorology and Climate Research (IMK), Karlsruhe Institute of Technology (KIT), Karlsruhe, Germany.

- Kunz, M., 2007: The skill of convective parameters and indices to predict isolated and severe thunderstorms. *Natural Hazards and Earth System Sciences*, **7**, 327–342.
- Kunz, M., U. Blahak, J. Handwerker, M. Schmidberger, H. J. Punge, S. Mohr, E. Fluck, and K. M. Bedka, 2018: The severe hailstorm in southwest Germany on 28 July 2013: Characteristics, impacts and meteorological conditions. *Quarterly Journal of the Royal Meteorological Society*, **144**, 231–250.
- Kunz, M. and M. Puskeiler, 2010: High-resolution assessment of the hail hazard over complex terrain from radar and insurance data. *Meteorologische Zeitschrift*, **19**, 427–439.
- Kuo, J.-T. and H. D. Orville, 1973: A radar climatology of summertime convective clouds in the black hills. *Journal of Applied Meteorology and Climatology*, **12**, 359 – 368.
- Lamb, D. and J. Verlinde, 2011: *Physics and chemistry of clouds*. Cambridge University Press, Cambridge, UK, 600 pages.
- Lang, P. P. M. H. R. J., P., 2003: Konvektionsentwicklung in Radarprodukten – ein operationelles Verfahren zur Analyse von Gewitterzellen und deren Zugbahnen, basierend auf Wetterradarprodukten, Berichte des Deutschen Wetterdienstes 222, Selbstverlag des Deutschen Wetterdienstes, Deutscher Wetterdienst, Offenbach, Germany.
- Lemon, L. R. and C. A. Doswell, 1979: Severe thunderstorm evolution and mesocyclone structure as related to tornadogenesis. *Monthly Weather Review*, **107**, 1184 – 1197.
- Lin, Y.-L. and T.-A. Wang, 1996: Flow regimes and transient dynamics of two-dimensional stratified flow over an isolated mountain ridge. *Journal of Atmospheric Sciences*, **53**, 139 – 158.
- Mahlke, H. M., 2017: Mechanismen der Auslösung hochreichender Konvektion im südwestdeutschen Mittelgebirgsraum. Ph.D. thesis, Institute of Meteorology and Climate Research (IMK), Karlsruhe Institute of Technology (KIT), Karlsruhe, Germany.
- Markowski, P. and Y. Richardson, 2010: *Mesoscale Meteorology in Midlatitudes*, Vol. 2. John Wiley & Sons Ltd., Publication, Chichester, United Kingdom, 407 pages.
- Marshall, J. S. and W. M. K. Palmer, 1948: The distribution of raindrops with size. *Journal of Atmospheric Sciences*, **5**, 165 – 166.
- Marwitz, J. D., 1972: The Structure and Motion of Severe Hailstorms. Part I: Supercell Storms. *Journal of Applied Meteorology*, **11**, 166–179.
- Mason, B. J. B. J., 1971: *The Physics of Clouds*. Oxford monographs on meteorology, Oxford University Press, Oxford, UK, 540 pages, Oxford.
- Muccilli, M., 2015: Using the Froude number to improve orographic snow forecasts in the Green Mountains of Vermont. *Eastern Region Technical Attachment*, National Weather Service, Maryland, USA, URL: <https://www.weather.gov/media/erh/ta2015--05.pdf>, accessed on: 25 Oct 2021.

- Möhler, O., 2019: Atmospheric Aerosols - Classical nucleation theory [lecture notes]. Institute of Meteorology and Climate Research (IMK), Karlsruhe Institute of Technology (KIT), Karlsruhe, Germany.
- Normand, C. W. B., 1938: On instability from water vapour. *Quarterly Journal of the Royal Meteorological Society*, **64**, 47–70.
- North Carolina Climate Office, 2021: Convection: Lifting Mechanisms, State Climate Office of North Carolina, North Carolina, USA. URL: <https://legacy.climate.ncsu.edu/edu/Lift>, accessed on: 24 Dec 2021.
- PennState Meteorology Department, 2021: Assessing Strong Updrafts, PennState College of Earth and Mineral Sciences, Pennsylvania, USA. URL: <https://learningweather.psu.edu/node/87>, accessed on: 20 Dec 2021.
- Peristeri, M., W. Ulrich, and R. K. Smith, 2000: Genesis conditions for thunderstorm growth and the development of a squall line in the northern alpine foreland. *Meteorology and Atmospheric Physics*, **72**, 251–260.
- Pflaum, J. C., 1980: Hail formation via microphysical recycling. *Journal of Atmospheric Sciences*, **37**, 160 – 173.
- Pruppacher, H. and J. Klett, 1997: *Microphysics of Clouds and Precipitation*. Kluwer Academic Publishers, Dordrecht, Niederlande, 954 pages.
- Puskeiler, M., 2009: Analyse der Hagelgefährdung durch Kombination von Radardaten und Schadendaten für Südwestdeutschland. Master’s thesis, Institute of Meteorology and Climate Research (IMK), Karlsruhe Institute of Technology (KIT), Karlsruhe, Germany.
- Puskeiler, M., 2013: Radarbasierte Analyse der Hagelgefährdung in Deutschland. Ph.D. thesis, Institute of Meteorology and Climate Research (IMK), Karlsruhe Institute of Technology (KIT), Karlsruhe, Germany.
- Rinehart, R. E. and E. T. Garvey, 1978: Three-dimensional storm motion detection by conventional weather radar. *Nature*, **273**, 287–289.
- Schmidberger, M., 2018: Hagelgefährdung und Hagelrisiko in Deutschland basierend auf einer Kombination von Radardaten und Versicherungsdaten. Ph.D. thesis, Institute of Meteorology and Climate Research (IMK), Karlsruhe Institute of Technology (KIT), Karlsruhe, Germany.
- Schraff, H. R., C., 2005: A description of the nonhydrostatic regionalmodel LM. Part III. URL: [https://www.dwd.de/SharedDocs/downloads/DE/modelldokumentationen/nwv/cosmo\\_de/lmk\\_dbbeschr\\_200901.pdf](https://www.dwd.de/SharedDocs/downloads/DE/modelldokumentationen/nwv/cosmo_de/lmk_dbbeschr_200901.pdf), accessed on: 18 Jul 2021.
- Scorer, R. S., 1995: Atmospheric convection. *International Journal of Climatology*, **15**, 821–822.

- Sekhon, R. S. and R. C. Srivastava, 1971: Doppler radar observations of drop-size distributions in a thunderstorm. *Journal of the Atmospheric Sciences*, **28**, 983–994.
- Seltmann, J. and J. Reidl, 1999: Improved clutter treatment within the german radar network: First results. *COST-75 Advanced Weather Radar Systems, International Seminar, EUR 18567*, C. Collier, Hrsg., Luxembourg, Luxembourg, 267–279.
- Smith, R. B., 1979: The influence of mountains on the atmosphere. *Advances in Geophysics*, **21**, 87–230.
- Smith, R. B., 1989: Hydrostatic airflow over mountains. *Advances in Geophysics*, **31**, 1–41.
- SwissRe-Institute, 2021: Sigma-Explorer, Worldwide Natural Catastrophes, Swiss Real Estate Institute, Zurich, Switzerland. URL: <https://www.sigma-explorer.com>, accessed on: 14 Aug 2021.
- Trapp, R. J., 2013: *Mesoscale-convective processes in the atmosphere*. Cambridge University Press, Cambridge, UK, 346 pages.
- Umscheid, M., 2005: Use of low-level lapse rates in forecasting convective initiation, National Weather Service, Maryland, USA. URL: <https://www.weather.gov/ddc/111r>, accessed on: 19 Feb 2022.
- Waldstreicher, J. S., 1989: A guide to utilizing moisture flux convergence as a predictor of convection. *National Weather Service Eastern Region Headquarters, National Weather Service, Maryland, USA*.
- Waldvogel, A., B. Federer, and P. Grimm, 1979: Criteria for the detection of hail cells. *Journal of Applied Meteorology and Climatology*, **18**, 1521 – 1525.
- Wegener, A., 1911: *Thermodynamik der Atmosphäre*. J.A. Barth, Germany, Leipzig, 376 pages.
- Wei, J., H. Su, and Z.-L. Yang, 2016: Impact of moisture flux convergence and soil moisture on precipitation: a case study for the southern united states with implications for the globe. *Climate Dynamics*, **46**, 467–481.
- Westermayer, A. et al., 2017: Identification of favorable environments for thunderstorms in reanalysis data. *Meteorologische Zeitschrift*, **26**, 59–70.
- Wilhelm, J., 2021: Einfluss atmosphärischer Umgebungsbedingungen auf den Lebenszyklus konvektiver Zellen in der Echtzeit-Vorhersage. Ph.D. thesis, Institute of Meteorology and Climate Research (IMK), Karlsruhe Institute of Technology (KIT), Karlsruhe, Germany.
- Wissmeier, U. and R. Goler, 2009: A comparison of tropical and midlatitude thunderstorm evolution in response to wind shear. *Journal of Atmospheric Sciences*, **66**, 2385–2401.

Young, K. C. et al., 1993: *Microphysical processes in clouds*. Oxford University Press, Oxford, UK, 448 pages.



# List of Figures

2.1	CAPE and CIN in radio soundings . . . . .	13
2.2	Life cycle of a single thunderstorm cell . . . . .	15
2.3	Gust front induced lifting processes in sheared environment . . . . .	16
2.4	Supercell cross-section and precipitation areas . . . . .	17
2.5	Classical nucleation theory . . . . .	18
2.6	Droplet and particle growth by collection . . . . .	20
2.7	Hailstone cross-section: Dry and wet growth . . . . .	21
2.8	Possible hail trajectories within a supercell . . . . .	22
2.9	DWD radar network . . . . .	24
2.10	Radar scanning strategy . . . . .	25
2.11	Errors and quality assurance in radar data . . . . .	28
2.12	Modification of a horizontal wind field by obstacles . . . . .	29
2.13	Model domain of COSMO-DE . . . . .	32
2.14	Rotated coordinate system in COSMO . . . . .	35
3.1	Identification of reflectivity cores in TRACE3D . . . . .	39
3.2	Handling of cell track crossings in TRACE3D . . . . .	40
3.3	Overview of data availability . . . . .	43
3.4	Statistical thunderstorm lifetime of KONRAD and TRACE3D data sets . . . . .	44
3.5	Cell propagation direction of KONRAD and TRACE3D data sets . . . . .	45
3.6	Potential hailstorm occurrence over Germany . . . . .	46
3.7	Model topography and investigation area . . . . .	46
3.8	Sensitivity study for filtering of non-event days . . . . .	48
3.9	Thermodynamic parameter of potential hail days and non-event days . . . . .	49
3.10	Thunderstorm effects within the analysis data . . . . .	50
3.11	Sensitivity study of filtering by hor. moisture flux convergence . . . . .	51
4.1	TRACE3D tracks within the investigation area . . . . .	55
4.2	Time of first detection of thunderstorm cells . . . . .	56
4.3	Propagation direction for cell tracks within the sub-areas . . . . .	57
4.4	Synoptic-scale situation for potential hail days . . . . .	58
4.5	Thunderstorm lifetime for cell tracks within the investigation area . . . . .	59
4.6	Automated hail threshold tracking vs. manual precipitation threshold tracking . . . . .	60
4.7	Time and spatial difference between automated and manual detection . . . . .	61
4.8	Spatial distribution of CAPE and LLR for potential hail days and non-event days . . . . .	63

4.9	Horizontal wind field for potential hail days and non-event days . . . . .	64
4.10	Hor. moisture flux convergence for potential hail days and non-event days .	65
4.11	Distribution of Brunt Vaisala frequency and Froude number for potential hail days . . . . .	66
4.12	Histograms of Brunt Vaisala frequency and Froude number between sub-areas	67
4.13	Horizontal wind field for low and high Froude number environments . . . .	69
4.14	Planetary boundary layer height for low and high Froude number environ- ments . . . . .	70
4.15	Hor. moisture flux convergence for low and high Froude number environments	70

# Danksagung

An dieser Stelle möchte ich mich bei allen, die mich während meiner Zeit als Studierender und in der Phase der Masterarbeit unterstützt haben, ganz herzlich bedanken.

Ein besonderer Dank geht dabei an Herrn Prof. Dr. Michael Kunz, der mir durch die Übernahme des Referats und die Aufnahme in die Arbeitsgruppe "Atmosphärische Risiken" das Anfertigen der Masterarbeit ermöglicht hat. Die Diskussionen mit ihm sowie die Kommentare zur schriftlichen Anfertigung waren aufschlussreich und halfen dabei, meine Auswertungen in die richtige Richtung zu lenken, ohne mich dabei in der Freiheit zur Umsetzung eigener Ideen einzuschränken. Bedanken möchte ich auch bei Herrn Prof. Dr. Peter Knippertz für die Übernahme des Korreferats.

Des Weiteren gilt ein großer Dank meinem Betreuer Dr. Jannik Wilhelm, der stets ein offenes Ohr für mich hatte und mich sowohl bei wissenschaftlichen Fragestellungen als auch bei den technischen Herausforderungen im Laufe der Abschlussarbeit unterstützte. Besonders hilfreich waren die umfangreichen Hinweise und Korrekturen beim Anfertigen der schriftlichen Arbeit. An dieser Stelle auch ein herzliches Dankeschön an Dr. Philipp Gasch für den regelmäßigen Austausch und die damit verbundenen Hinweise und Ideen.

Dankeschön auch an den Deutschen Wetterdienst für die Bereitstellung der Radar- und Modelldaten, sowie an Manuel Schmidberger und nochmals Jannik Wilhelm, für die Aufbereitung und Bereitstellung der Zellverfolgungsdatensätze.

Ebenfalls möchte ich mich bei der gesamten Arbeitsgruppe "Atmosphärische Risiken" bedanken, die mich herzlich aufgenommen hat und wo ich neben vielen wissenschaftlichen Diskussionen auch an einer einzigartig freundschaftlichen Atmosphäre teilhaben durfte.

Zum Schluss geht ein herzliches Dankeschön an meine Familie. Vielen Dank an meine Eltern, die mir das Studium ermöglicht haben und mich während meiner gesamten Zeit am KIT unterstützten. Ein ebenso großer Dank gebührt meiner Lebensgefährtin Nicole für die Hilfe beim Korrekturlesen, für das Verständnis meines teilweise erhöhten Stresslevels und für die dabei helfenden, ausgleichenden Momente.



# Declaration of authenticity

Ich versichere wahrheitsgemäß, die Arbeit selbstständig angefertigt, alle benutzten Hilfsmittel vollständig und genau angegeben und alles kenntlich gemacht zu haben, was aus Arbeiten anderer unverändert oder mit Abänderungen entnommen wurde.

Karlsruhe, 21. 02. 2022

Fabian Siegmann